

**UNIVERSIDADE ESTADUAL DE PONTA GROSSA
SETOR DE ENGENHARIAS
PROGRAMA DE PÓS-GRADUAÇÃO EM ENGENHARIA E CIÊNCIA DE
MATERIAIS**

AMANDA CATARINA BRANDES

**FEASIBILITY OF FS AS A DEPOSITION LAYER TECHNIQUE TO APPLY AS
FATIGUE CRACK PROPAGATION STOPPER
VIABILIDADE DO FS COMO TÉCNICA DE DEPOSIÇÃO EM CAMADA PARA
APLICAÇÃO COMO RETARDADOR DE PROPAGAÇÃO DE TRINCA POR
FADIGA**

**PONTA GROSSA
2023**

AMANDA CATARINA BRANDES

**FEASIBILITY OF FS AS A DEPOSITION LAYER TECHNIQUE TO APPLY AS
FATIGUE CRACK PROPAGATION STOPPER
VIABILIDADE DO FS COMO TÉCNICA DE DEPOSIÇÃO EM CAMADA PARA
APLICAÇÃO COMO RETARDADOR DE PROPAGAÇÃO DE TRINCA POR
FADIGA**

Dissertation presented as requirement for obtaining the title of Master of Engineering and Materials Science at the State University of Ponta Grossa.

Field: Materials Processing and Characterization.

Advisor: Prof. Dr. André L. M. de Carvalho

Co-Advisor: Prof. Dr. Juliana de Paula Martins

**PONTA GROSSA
2023**

B817 Brandes, Amanda Catarina
Feasibility of FS as a deposition layer technique to apply as fatigue crack propagation stopper / Amanda Catarina Brandes. Ponta Grossa, 2023.
111 f.

Dissertação (Mestrado em Engenharia e Ciência de Materiais - Área de Concentração: Desenvolvimento e Caracterização de Materiais), Universidade Estadual de Ponta Grossa.

Orientador: Prof. Dr. André Luis Moreira Carvalho.
Coorientadora: Profa. Dra. Juliana de Paula Martins.

1. Friction surfacing. 2. Aluminum alloy. 3. Fatigue crack propagation. 4. Damage tolerance. 5. Process parameters. I. Carvalho, André Luis Moreira. II. Martins, Juliana de Paula. III. Universidade Estadual de Ponta Grossa. Desenvolvimento e Caracterização de Materiais. IV.T.


CDD: 620.11

AMANDA CATARINA BRANDES


FEASIBILITY OF FS AS A DEPOSITION LAYER TECHNIQUE TO APPLY AS
FATIGUE CRACK PROPAGATION STOPPER

Dissertation presented as requirement for obtaining the title of Master of Engineering
and Materials Science at the State University of Ponta Grossa.
Field: Materials Processing and Characterization

Ponta Grossa, August 15th, 2023.

Documento assinado digitalmente
 ANDRE LUIS MOREIRA DE CARVALHO
Data: 14/03/2024 14:28:25-0300
Verifique em <https://validar.iti.gov.br>

Prof. Dr. André Luis Moreira de Carvalho
Department of Materials Engineering, State University of Ponta Grossa DEMA/UEPG

Documento assinado digitalmente
 HERMAN JACOBUS CORNELIS VOORWALD
Data: 17/03/2024 20:54:44-0300
Verifique em <https://validar.iti.gov.br>

Prof. Dr. Herman Jacobus Cornelis Voorwald
Department of Materials and Technology, State University of São Paulo FEG/UNESP

 Digitally signed by
AFONSO
REGULY:62849352004
Date: 2024.03.18 16:51:53
-03'00'

Prof. Dr. Afonso Reguly
Department of Metallurgy, Federal University of Rio Grande of Sul EE/UFRGS

ACKNOWLEDGMENT

I acknowledge the C2PA Consortium for Research & Development in Friction Stir Processing for providing the opportunity to develop this research in the field of Friction Surfacing.

I acknowledge the Department of Solid-State Materials Processing in Helmholtz-Zentrum Hereon for contributing to this project and for providing the necessary resources and infrastructure to conduct this research.

I acknowledge the State University of Ponta Grossa (UEPG) for providing this invaluable opportunity to pursue high-quality public education.

I acknowledge Embraer SA for providing the necessary material used in this work and for the knowledge shared in the aircraft industry. Also, I extend my gratitude to Marcos H. Miyazaki and Fernando F. Fernandez for their unwavering support and encouragement throughout this project.

I acknowledge and express my sincere gratitude to Dr. Prof. André L. M. Carvalho and to Dra. Prof. Juliana P. Martins, for believing in my passion for solid-state joining processes and for all the support and patience up to now. As well as my supervisor Dr.-Ing. Arne Roos and Prof. Dr.-Ing. habil. Benjamin Klusemann from WMP for all the knowledge shared and enthusiasm in the field of solid-state joining processes.

I also would like to express my deepest gratitude to all those who have supported and guided me throughout my time in completing this master thesis. My sincere thanks go to my family and friends for their unwavering love, encouragement, and understanding throughout this demanding journey. Their constant support and belief in my abilities have been a source of inspiration and motivation.

ABSTRACT

The search for innovative technologies with the purpose of increasing service life, thus reducing maintenance and frequency of inspections, is the main objective for many aircraft industries, such as EMBRAER S.A. Techniques concerning the damage tolerance improvement of fuselage structures are becoming an interesting solution when it comes to aluminum structures exposed to fatigue. There is a rising interest in the use of friction surfacing (FS) as a technique to retard fatigue crack propagation (FCP). FS is a deposition process, used to deposit layers of material through plastic deformation and high temperature. Once the process temperature achieved during FS is below the melting point, the deposition occurs entirely in a solid state. This characteristic is advantageous regarding the joining of “non-weldable” alloys, such as the high alloyed aluminum alloys from 2XXX and 7XXX series. The first part of this study is to identify the best parameter set, regarding satisfactory superficial morphology, effective bonding width, and bonding strength. Thus, light microscopy (LM), scanning electron microscopy (SEM) equipped with a field emission gun (FEG), Vickers microhardness, and three-point bending tests are used to evaluate the best set, in terms of microstructural features and mechanical behavior. Then, the second part consists of understanding the mechanical and FCP behavior of friction surfaced AA2024 on AA7475 substrate, by evaluating the yield strength (YS), ultimate tensile strength (UTS), and elongation with uniaxial tensile tests. For the FCP tests, three specimen configurations are used to compare the influence of the advancing side (AS) and retreating side (RS) in the fatigue crack growth rate (FCGR) and the influence of a post surface machining process. To identify features on the fractured surfaces after tensile and fatigue failure, LM and SEM-FEG fractography were performed. Furthermore, this work has resulted from the industrial research entitled “*Friction Surfacing for Damage Tolerance Improvement in Aircraft Structure*” from the joining effort among partners from Department of Solid-State Materials Processing from the Institute of Materials Mechanics (Helmholtz-Zentrum Hereon) in Germany, Embraer, State University of Ponta Grossa (UEPG).

Keywords: friction surfacing, process parameters, aluminum alloy, fatigue crack propagation, damage tolerance.

RESUMO

A busca por tecnologias inovadoras com o propósito de aumentar a vida útil, assim reduzindo a manutenção e frequência de inspeções são os principais objetivos de muitas indústrias aeronáuticas, tal como a EMBRAER S.A. Técnicas relativas à melhoria da tolerância ao dano estão se tornando uma solução interessante quando se trata de estruturas de alumínio expostas à fadiga. Há um crescente interesse no uso de deposição superficial por atrito (FS) como uma técnica para retardar a propagação de trinca por fadiga. FS é um processo de deposição, usado para depositar camadas de material por deformação plástica e alta temperatura. Uma vez que a temperatura de processo alcançada durante o FS está abaixo do ponto de fusão, a deposição ocorre inteiramente em estado sólido. Esta característica é vantajosa em relação à união de ligas "não soldáveis", tais como ligas das séries 2XXX e 7XXX. A primeira parte deste estudo consiste em identificar o melhor set de parâmetro, tratando-se de uma morfologia superficial satisfatória, comprimento de união efetivo e resistência da união. Para tanto, microscopia ótica (MO), microscopia eletrônica de varredura (MEV) equipado com fonte de emissão de campo (FEG), microdureza Vickers e teste de dobramento por três pontos são utilizados para avaliar o melhor parâmetro. Em seguida, a segunda parte consiste em entender os comportamentos mecânico e de propagação de trinca por fadiga (FCP) de depósitos de AA2024 sobre substrato de AA7475, avaliando a tensão de escoamento, a tensão de resistência máxima e o alongamento no teste de tração. Para os testes FCP, três configurações de amostras são utilizadas para comparar a influência do lado de avanço e lado de recuo na taxa de propagação de trinca por fadiga (FCGR), e a influência de um pós processamento de usinagem na superfície. Para identificar as características na superfície de fratura após ensaio de tração e falha por fadiga, fractografia por meio de MO e MEV-FEG serão utilizadas. Além disso, esse trabalho resultou da pesquisa industrial intitulada "*Friction Surfacing for Damage Tolerance Improvement in Aircraft Structure*" da união de esforços entre os parceiros do *Department of Solid-State Materials Processing* do *Institute of Materials Mechanics* (Helmholtz-Zentrum Hereon) da Alemanha, Embraer e a Universidade Estadual de Ponta Grossa.

Palavras-chave: Deposição superficial por atrito, parâmetros de processo, liga de alumínio, propagação de trinca por fadiga, tolerância ao dano.

FIGURE LIST

Figure 1 –	Major structural components and property requirements present on an aircraft.	18
Figure 2 –	Illustration of a semi-monocoque fuselage structure, with the presence of frames, longerons and stringers.	19
Figure 3 –	Combination of compression and tension forces during bending loads of an aircraft wing.	20
Figure 4 –	Illustration of an empennage structure from an aircraft, with horizontal stabilizer, vertical stabilizer, rudder, trim tabs, elevator.	20
Figure 5 –	Aproximate weight distribution of a large passenger aircraft.	21
Figure 6 –	Designation system for aluminum alloys according to Aluminum Association.	22
Figure 7 –	Coherency between particle and matrix interface. (a) Coherent. (b) Semicoherent. (c) Incoherent.	24
Figure 8 –	Illustration of (a) Particle shear and (b) Orowan mechanism as barriers to dislocation movement.	24
Figure 9 –	Application of 2XXX and 7XXX alloys in structures and components from an airplane.	26
Figure 10 –	Photograph of Boeing 737-3H4 with a close-up to the fuselage skin crack.	29
Figure 11 –	Fatigue stress level estimative on an aircraft wing, from a single flight cycle.	29
Figure 12 –	Fatigue parameters at constant amplitude in (a) tension-compression load and (b) tension-tension load.	30
Figure 13 –	Crack tip loading modes.	31
Figure 14 –	Common log-log FCP curve regarding crack growth rate da/dN and stress intensity factor range ΔK	32
Figure 15 –	Typical profile of RES induced by shot peening, with compressive stresses close to the surface, and tensile stresses in the remnant length of the material.	34
Figure 16 –	Example of bonded straps between stringers, applied in aircraft structures.	34
Figure 17 –	RES distribution along the scan line for Ti-6Al-4V deposits on similar substrate by FS.	35
Figure 18 –	Crack length versus load cycles in Ti-6Al-4V specimens from base material and deposited with different deposition speed.	36
Figure 19 –	Process steps from FS layer deposition. Starting position (A). Plasticizing stage (B). Deposition stage (C). Final stage (D).	37
Figure 20 –	Schematic representation of the FS process with designation of the main FS process parameters.	37
Figure 21 –	Monitoring of axial force, torque and stud axial displacement in Z-direction of friction surfaced AA6082 over AA2024.	38
Figure 22 –	Recorded axial force and deposit surface appearance of Ti-6Al-4V titanium alloy.	38
Figure 23 –	Deposit surface appearance generated from friction surfaced AA6082 over AA2024.	39

Figure 24 – Influence of axial force on deposit geometry of friction surfaced mild steel over mild steel.....	40
Figure 25 – Influence of deposition speed on deposit geometry of friction surfaced AA5083 over AA7050-T7451 alloy.	40
Figure 26 – Influence of rotation speed on deposit geometry of friction surfaced AA5052 alloy.	41
Figure 27 – Fuselage panel with FS deposits as an example of application from this technique.....	42
Figure 28 – AA7475-T761 substrate and AA2024-T351 stud material provided by EMBRAER SA.....	43
Figure 29 – Illustration of HLR RAS 1 machine used to produce layer FS deposition process at Hereon (Germany).....	44
Figure 30 – Specimen extraction plan for metallography, microhardness profile and three-point bending test.....	46
Figure 31 – Schematic positioning of thermocouples in the substrate for temperature measurements.	46
Figure 32 – Exemplary friction surfacing three-point bending test specimen after machining, showing side view (left) and transverse view (right) of the specimen.....	48
Figure 33 – Universal testing machine used for three-point bending test at Hereon (Germany).....	48
Figure 34 – (a) Dimension specification from tensile test specimens. (b) AA7475-T761 BM and (c) FS specimen with post machined layer.	49
Figure 35 – Extensometer by MTS.....	50
Figure 36 – Specimen dimension and details for FCP test.....	50
Figure 37 – Specimen configuration for FCP tests.....	51
Figure 38 – Servo hydraulic machine MTS by Landmark, specimen, clamping and clip-gage system.	52
Figure 39 – Servo hydraulic machine by SCHENCK and stereoscope system used for crack growth measurement.....	52
Figure 40 – Process plot of a layer deposition of AA2024 over AA7475 alloys. Parameters are $F_z = 12$ kN, $v_x = 8$ mm/s and $R_s = 900$ rpm.	53
Figure 41 – FS process temperature measures. (a) Vertical temperature distribution via IR-camera. (b) Horizontal temperature distribution via embedded thermocouples into the substrate sheet.....	54
Figure 42 – Axial force plot and visual appearance. Process parameters are (a) $R_s = 900$ rpm, $F_z = 12$ kN, $v_x = 10$ mm/s and (b) $R_s = 900$ rpm, $F_z = 8$ kN, $v_x = 12$ mm/s.....	55
Figure 43 – Deposit surface morphology and superposed axial force over the 27 specimens. (a) Constant $F_z = 8$ kN, $R_s = 900, 1100$ and 1300 rpm, $v_x = 8, 10, 12$ mm/s. (b) Constant $F_z = 10$ kN, $R_s = 900, 1100, 1300$ rpm, $v_x = 8, 10, 12$ mm/s. (c) Constant $F_z = 12$ kN, $R_s = 900, 1100, 1300$ rpm, $v_x = 8, 10, 12$ mm/s.	57
Figure 44 – Cross-section macrograph from specimen S09. Parameters are $F_z = 12$ kN, $v_x = 8$ mm/s and $R_s = 900$ rpm.....	58
Figure 45 – Control chart for a bonded width between 10 and 15 mm.....	59

Figure 46 – Lateral surface of different FS specimens after three-point bending tests.....	60
Figure 47 – Microstructure from BM. (a) three-rolling direction AA7475-T761 sheet, (b) elongated grains in extrusion direction and (c) equiaxed grains in cross-section area of AA2024-T351 stud.	61
Figure 48 – Micrographs from the microstructure of the deposit. Process parameters are FZ = 12 kN, vx = 8 mm/s and RS = 900 rpm. (a-b) Bonding interface; (c) refined deposit microstructure; (d) substrate microstructure; edges from (e) AS and (f) RS.	62
Figure 49 – SEM micrograph from the bonded interface (a). EDS analysis from bonded interface region between AA2024 deposit and AA7475 substrate (b).	63
Figure 50 – FS offset. (a) and (b) showing the stud position on the substrate, and (c) the cross-section macrograph with a 4.5 mm offset.	64
Figure 51 – Microhardness profile of FS specimens and BM, with constant (a) $R_s = 900$ rpm, (b) $R_s = 1100$ rpm and (c) $R_s = 1300$ rpm.	65
Figure 52 – Microhardness map from cross-section of specimen with Fz= 12 kN and v_x= 12 mm/s, showing an asymmetrical HAZ.....	67
Figure 53 – Tensile test results for AA7475-T761 BM (BM01, BM02 and BM03) and FS specimens (FS01, FS02 and FS03).....	68
Figure 54 – Fracture surface of AA7475-T761 BM specimen after tensile test (a). Fractured surface features (b), presence of shear dimples, tear ridges and smaller dimples (c) and magnification of the smaller dimples(d). ...	69
Figure 55 – Fractured surface of FS specimen after tensile test (a). Bonding interface (b), AA2024 deposit material (c) and AA7475 substrate material (d).	70
Figure 56 – Crack size versus number of cycles for AA7475-T761 BM and FS specimens with A-A and R-R deposit configuration.	71
Figure 57 – Results for da/dN over ΔK for BM and FS specimens with (a) A-A configuration and (b) R-R configuration.....	72
Figure 58 – FCP rate (da/dN) versus crack length (2a) for AA7475-T761 BM, A-A and R-R FS specimen configuration.....	74
Figure 59 – Crack size (2a) versus number of cycles for BM (AA7475-T761) and FS specimens with R-A deposit configuration and machined surface.	75
Figure 60 – Crack growth rate da/dN over crack length on RS notch side for specimen FCP06FS. Different slope in (a) unmachined region and (b) machined region.....	76
Figure 61 – Fracture surface morphology from AA7475-T761 BM. Pre-cracking zone (a) and low ΔK I (b).....	76
Figure 62 – Fracture surface morphology from AA7475-T761 BM. Low ΔK II (a) and moderate ΔK (b).	77
Figure 63 – Fracture surface morphology from FS specimen. Pre-cracking zone (a) and low ΔK I region (b).	78
Figure 64 – Fracture surface morphology from FS specimen. Moderate ΔK (a) and (b).....	79
Figure 65 – Fatigue striation marks for BM specimen at different ΔK ranges: (a) region A, (b) region B and (c) region C.....	80

Figure 66 – Fatigue striation marks for FS specimen at different ΔK ranges: (a) region A, (b) region B and (c) region C.....81

TABLE LIST

Table 1 – Temper designation used in aluminum alloys and description.	25
Table 2 – The main nucleation sites and its related number of aircraft accidents. ...	28
Table 3 – Chemical composition of AA2024-T351 stud and AA7475-T761 sheet.	43
Table 4 – Process window for the main process parameters (axial force, rotation speed and deposition speed).	45
Table 5 – Detailed steps for grinding and polishing.	47
Table 6 – Suitable process parameter selection regarding surface appearance and process stability.	58
Table 7 – Mean values of tensile properties for YS, UTS and elongation from BM and FS specimens.	68
Table 8 – Mean values of Paris constants and FCP rate from AA7475-T761 BM and FS specimens with A-A and R-R configuration.	73
Table 9 – Average striation spacing for BM and FS specimen in different regions.	82

ABBREVIATION LIST

AA	Aluminum Association
AS	Advancing Side
BM	Base Material
COD	Crack Opening Displacement
DIC	Digital Image Correlation
FCGR	Fatigue Crack Growth Rate
FCP	Fatigue Crack Propagation
FEG	Field Emission Gun
FS	Friction Surfacing
FSW	Friction Stir Welding
LM	Light Microscopy
LSP	Laser Shock Process
MT	Middle Tension
RS	Retreating Side
SEM	Scanning Electron Microscopy
UTS	Ultimate Tensile Stress
YS	Yield Stress

SYMBOL LIST

$\Delta\sigma$	Cyclic Stress Range
f	Frequency
σ_a	Cyclic Stress Amplitude
σ_m	Mean Stress
R	Stress Ratio

SUMMARY

1	INTRODUCTION	15
2	OBJECTIVES	17
2.1	GENERAL OBJECTIVES	17
2.2	SPECIFIC OBJECTIVES.....	17
3	LITERATURE REVIEW	18
3.1	AIRCRAFT STRUCTURES AND MATERIALS	18
3.2	ALUMINUM ALLOYS FOR AIRCRAFT INDUSTRY	21
3.2.1	General properties of 2XXX and 7XXX aluminum alloys	25
3.3	FATIGUE FAILURE IN AIRCRAFT STRUCTURES	27
3.3.1	Fatigue.....	27
3.3.2	Fatigue crack propagation tests.....	31
3.4	DAMAGE TOLERANCE IMPROVEMENT.....	33
3.5	FRICTION SURFACING LAYER DEPOSITION	36
3.5.1	FS parameters and process monitoring.....	37
3.5.2	Influence of FS process parameters	39
3.5.3	Potential application of FS	41
4	MATERIALS AND METHODOLOGY	43
4.1	MATERIALS	43
4.2	METHODOLOGY	44
4.2.1	Friction Surfacing Equipment.....	44
4.2.2	Process Parameters	45
4.2.3	Specimen Extraction Plan.....	45
4.2.4	Temperature Measurement	46
4.2.5	Metallographic Analysis	47
4.2.6	Bending Test	48
4.2.7	Microhardness Test	48
4.2.8	Tensile Test	49
4.2.9	Fatigue Crack Propagation Test.....	50
5	RESULTS AND DISCUSSION	53
5.1	PROCESS ANALYSIS.....	53
5.2	PROCESS PARAMETER ANALYSIS	55
5.2.1	Deposit surface morphology	55

5.2.2	Deposit geometry.....	58
5.2.3	Effective interface adhesion.....	59
5.3	SUITABLE PROCESS PARAMETER.....	61
5.4	MICROSTRUCTURE ANALYSIS	61
5.5	MECHANICAL TESTING.....	64
5.5.1	Microhardness test	64
5.5.2	Tensile test	67
5.6	FATIGUE CRACK PROPAGATION	71
5.6.1	Fracture surface analysis.....	76
6	CONCLUSIONS	83
7	SUGESTIONS FOR FUTURE WORK	85
	REFERENCES	88
	APPENDIX A – PROCESS DATA GRAPHS OF FS SPECIMENS.	97
	APPENDIX B – MACROGRAPHS FROM CROSS-SECTIONED SPECIMENS. ...	107

1 INTRODUCTION

The application of aluminum alloys still play an important role in the aircraft industry due to its well-known excellent mechanical properties. Despite the crescent use and research in composite materials in recent years, high strength aluminum alloys remain important for aerospace structures due to its advantageous properties, such as toughness, easy fabricability and low weight. (1)

The increased use of aluminum alloys as structural materials is the main driving force for the development of innovative technologies to improve performance, damage tolerance and fatigue resistance of this material, without deteriorating mechanical, chemical or metallurgical properties.(2) The biggest challenge for the aerospace field is the development of new strategies to extend the airplane life service and reduce operating and maintenance costs.

Fatigue is well-known as the main failure mode in aircraft parts. It is defined as the degradation of mechanical properties under cyclic loading. It starts with crack initiation in high stress concentration sites, usually from poor drilled holes, screws, sharp notches, or any other surface damage. After that, crack propagation starts, which may advance until overall failure of the structure. These failures may lead to undesired catastrophic accidents, that's why the search for innovative techniques is becoming essential to improve damage tolerance, extend the fatigue life of aircraft structures and prevent structure failures.

The use of crack stopper straps in critical areas of an aircraft structure has the purpose to arrest the fast fracturing of a crack. However, this technique generates thermal residual stresses from adhesive curing phenomena, which might lead to undesired mechanical performance. Another method to increase service life of an engineered component exposed to fatigue is the introduction of residual stresses in the surface layer to induce compressive residual stresses, enough to retard crack initiation or arrest crack growth. These techniques are such as shot peening, laser shock peening and laser heating from the surface engineering.

One promising technique to increase damage tolerance in aluminum alloy structures is by friction surfacing (FS) layer deposition. This process consists of material deposition in layers from a rotating consumable stud pressed over a substrate surface. The combination of frictional heat and plastic deformation enables the stud material adherence on the substrate, and the deposition of the plasticized material

occurs with a translational movement. This deposition process occurs in solid-state, which is suitable for the joining of “non-weldable” alloys such as those with high amounts of copper, e.g., from 2XXX and 7XXX series. As other friction-based welding and local heating techniques, FS was found as an alternate technique to introduce residual stresses in coated components, which has the potential to increase the service life. In FS deposition processes, the localized heating and subsequent cooling leads to thermal stress gradient in the body. This thermal misfit creates a tensile stress in the deposit area, which is called as active zone. The balance is found in a compressive stress area around the deposit, called as compensative zone (3). This compressive stress acts as a crack growth retarder, which is the desired condition for this study.

Therefore, the current investigation aims to assess the feasibility of the FS processing as a deposited strip technique for application in fuselage structures. The objective is to use this technique as a FCP stopper, thereby enhancing the damage tolerance behavior of the structure. This technique has the potential to replace the existing ones currently employed in the aircraft industry. To achieve these goals, the current research was conducted in two parts. First, the investigation of the best parameter set for the deposition of AA2024 on AA7475, following choosing criteria, such as surface morphology, deposit geometry and adhesion resistance. The second part regards the mechanical properties, by examining the microhardness, YS, UTS, elongation and FCP.

Furthermore, this master’s research is inserted into the industrial research entitled “*Sustainable Production of Fuselage Sections with Improved Damage Tolerance Behavior and Increased Productivity*” from the joining the effort among partners the Department of Solid-State Materials Processing from the Institute of Materials Mechanics at Hereon (Helmholtz-Zentrum Hereon) in Germany, Embraer, State University of Ponta Grossa (UEPG) from the C2PA. The way to develop industrial research in advanced technology, i.e., Friction Stir Welding (FSW) and Friction Surfacing (FS) to the fuselage structure application.

C2PA Industrial Research Consortia for Friction Stir Processing R&D, which was created in 2015. It is the first consortium that develops industrial research approaching FSW and FS and the pioneer to carry out industrial research concerning FS in Brazil, with the project “Development of Friction Surfacing Technology for Aeronautic Application” having the Embraer as a partner and has been developed at UEPG.

2 OBJECTIVES

2.1 GENERAL OBJECTIVES

The general objective of this study is to find the best process parameter set in the deposition of AA2024-T351 on AA7475-T761 sheets. Then, investigate the FCP behavior from the FS technique with the chosen parameter.

2.2 SPECIFIC OBJECTIVES

The specific objective of this study is to:

- Analyze the surface morphology of AA2024 layers deposited over AA7475 sheets;
- Produce deposited layers with an effective bonding width between 10 and 15 mm wide;
- Investigate the adhesion quality of selected process parameters through three-point bending test;
- Analyze the macro and microstructural features achieved after FS through LM and SEM-EDS;
- Analyze the influence of FS on mechanical properties, such as microhardness and tensile properties;
- Execute FCP tests in AA7475-T761 base material (BM) and three FS layer configuration.
- Obtain the FCP rate in specimens with and without deposited layers, after FCP test;
- Analyze the fractured surface from the specimens with deposited layers after tensile and FCP tests.

3 LITERATURE REVIEW

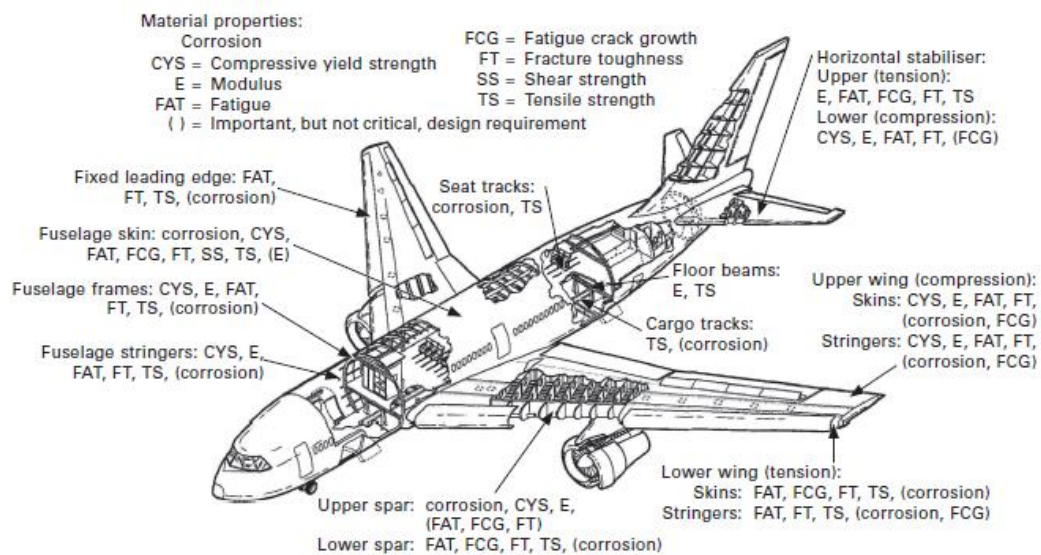
The following section gives an overview of aircraft structures, materials used in aerospace industry and aluminum alloys used in the current study. Furthermore, an introduction to fatigue failure of aircraft structures and techniques to improve damage tolerance, such as solid-state based FS layer deposition, is given.

3.1 AIRCRAFT STRUCTURES AND MATERIALS

The understanding of aircraft structures and predominant loads during life service are essential for the structural designers and engineers to achieve a maximum safety margin and minimum maintenance for a serviceable airliner.

The main structural parts of an aircraft are fuselage, wings, empennage, and engine.(4) During flight, the predominant loads are tension, shear and compression due to loading of the wings and cabin pressure that causes bending of the fuselage. (5-7) The property requirements for all major structure of an aircraft is summarized in Figure 1.

Figure 1 – Major structural components and property requirements present on an aircraft.



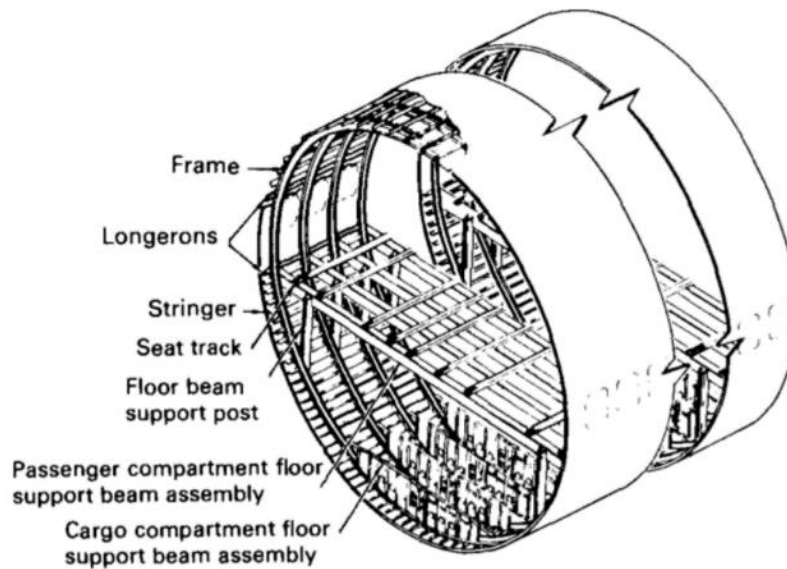
Source: STARKE, E. A.; STALEY, J. T. Application of modern aluminum alloys to aircraft. Progress In Aerospace Sciences, v. 32, n. 2-3, p. 131-172, 1996. (4)

The modern fuselage shell-like structure, known as a semi-monocoque, consists of a thin skin supported by stiffening components: longitudinal elements (stringers and longerons) and transverse elements (frames and bulkheads). These

components are used in aircraft to prevent buckling and support body loads during flight or landing. (4,6)

The fuselage must carry tension loads promoted by shear strength and cabin pressure. Stringers are applied to carry tension and compression loads, giving strength to the fuselage shell. Frames are used to maintain the fuselage shape and reduce instability. Bulkheads are applied in specific points to distribute the load from wings, tail and landing gear into fuselage skins. (4,6) These components are illustrated in more details in Figure 2.

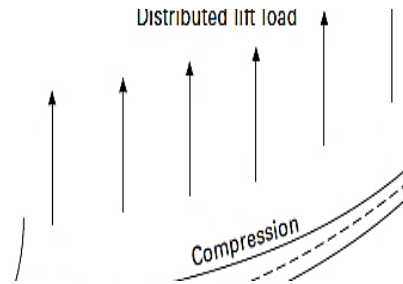
Figure 2 – Illustration of a semi-monocoque fuselage structure, with the presence of frames, longerons and stringers.



Source: NIU, M. Chun-Yung. Airframe structural design: practical design information and data on aircraft structures. California: Conmilit Press Ltd, 1988. 612 p. (6)

The wings are responsible for maintaining the flight and to transmit the applied air load to the fuselage. Moreover, it carries loads from internal fuel pressure, landing gear, engines and trailing edge. Wings are composed of stringers, spars and ribs that gives support to thin skins. During service, the wings bend constantly to maintain flight, and this generates the combination of compression and tension forces, as illustrated in Figure 3. The upper part of the wing suffers compression during flight, and the lower part suffers tension. During taxiing, it's the reverse. (4,6)

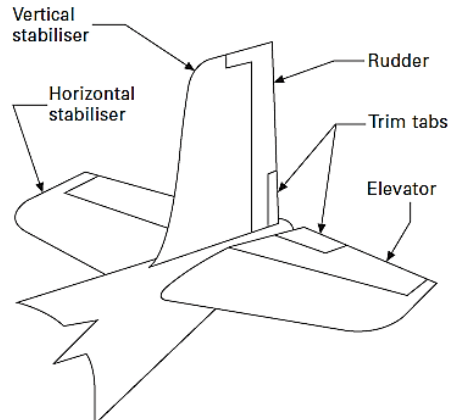
Figure 3 – Combination of compression and tension forces during bending loads of an aircraft wing.



Source: MOURITZ, A. P. (ed.). 1 – introduction to aerospace materials. In: MOURITZ, A. P. (ed.). Introduction to aerospace materials. Cambridge: Woodhead Publishing Limited, 2012. P. 39-56. (5)

The empennage provides stability and controls the direction of the aircraft, guaranteeing a straight flight. It is constructed with a tail assembly, consisting of horizontal and vertical stabilizers, elevators, rudders and trim tabs, as shown in Figure 4. The main loads in this part are compression and tension, and act more on stabilizers. (4,6)

Figure 4 – Illustration of an empennage structure from an aircraft, with horizontal stabilizer, vertical stabilizer, rudder, trim tabs, elevator.



Source: MOURITZ, A. P. (ed.). 1 – introduction to aerospace materials. In: MOURITZ, A. P. (ed.). Introduction to aerospace materials. Cambridge: Woodhead Publishing Limited, 2012. P. 39-56. (5)

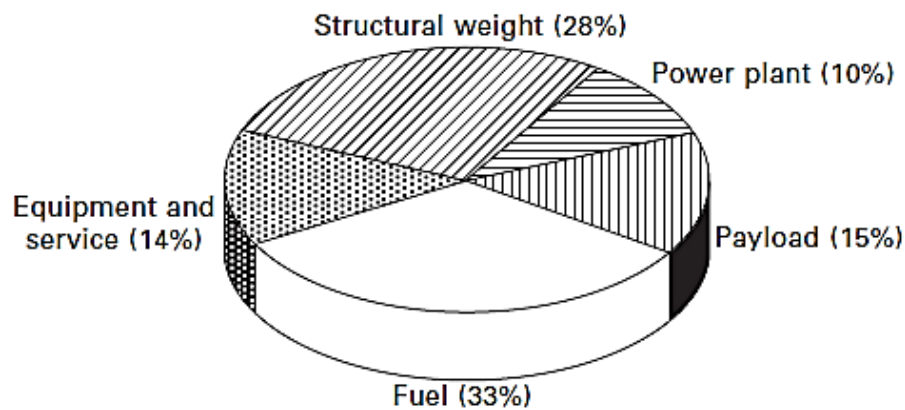
The appropriate material selection for aircraft structures is ruled mainly by component design, function, loads and service conditions. (3) Although, aerospace materials also require the combination of high stiffness, strength, damage tolerance, wear and corrosion resistance. (8,9)

During a designed life operation in commercial or military airliners, the structures should not crack, corrode, or suffer big damages under high loads, adverse environmental conditions and mechanical impacts. (5) These requirements are

extensively studied through tweaking material composition, modifying heat treatment conditions, structure design and processes that improves damage tolerance of a component. (9)

In general, the airframe takes between 20 to 40% of the weight from an aircraft, while the remanent weight is distributed in power plant, fuel, payload, equipment and service (Figure 5). (5) The rising demand for fuel economy by saving weight and materials with enhanced strength-to-weight ratio are becoming an essential factor for the study and application of light-weight structures. (4,5,7)

Figure 5 – Aproximate weight distribution of a large passenger aircraft.



Source: MOURITZ, A. P. (ed.). 1 – introduction to aerospace materials. In: MOURITZ, A. P. (ed.). Introduction to aerospace materials. Cambridge: Woodhead Publishing Limited, 2012. p. 39-56. (5)

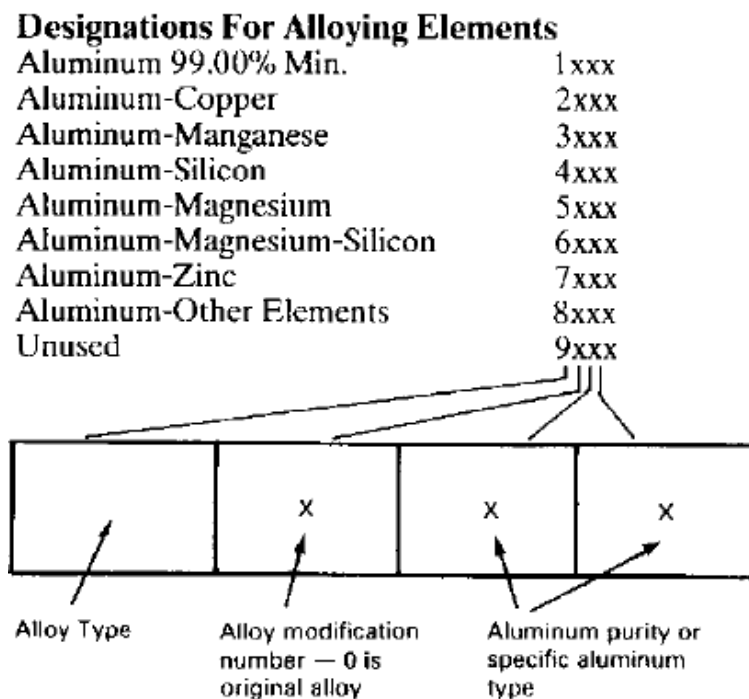
The most common aerospace materials present in modern airliners are aluminum, magnesium, titanium, steel alloys and fiber-reinforced polymer composite. Though, even with the advance in polymer composite research and application, aluminum alloys are still present in 60 to 80% of the airframe weight due to its great weight-efficiency. (7,10)

3.2 ALUMINUM ALLOYS FOR AIRCRAFT INDUSTRY

Since the 1930s, aluminum alloys assume an important role in aerospace application, specifically with the discovery of precipitation hardening by Alfred Wilm in these alloys. (4) The main reasons that makes aluminum alloys very attractive for the aircraft industry is the moderate cost, fabricability, light weight, ductility, fracture toughness, fatigue resistance and possibility to tweak properties by mechanical or thermal treatments. (7,9)

Aluminum alloys are applied in the form of cast, wrought non-heat-treatable and wrought heat-treatable alloys. For convenience, a designation system was built by the Aluminum Association to classify these two alloy categories. (11) For wrought alloys, a four-digit number system (XXXX) is used to identify up to eight alloy series. The first digit indicates the alloy type. The second digit regards any alloy modification (0 is referred as original). The last two digits specifies the alloy purity or simply alloy identification inside a certain series. (6,11) For cast alloys, the alloy designation is given by a three-digit number and a decimal. The only difference from wrought alloy designation is the final digit: alloy composition for casting (.0) or ingot (.1 or .2). (11) Figure 6 shows a summarized example of the designation system for wrought aluminum alloys.

Figure 6 – Designation system for aluminum alloys according to Aluminum Association.



Source: NIU, M. Chun-Yung. Airframe structural design: practical design information and data on aircraft structures. California: Conmil Press Ltd, 1988. 612 p. (6)

Cast alloys are produced with casting techniques (sand or permanent mold), do not suffer any mechanical or heat treatment and its application in aircraft is rare. (5,7,11) Wrought alloys, especially heat-treatable alloys, are present in approximately all aluminum used in aircraft structures, in the form of rolled sheets, foil, extruded bar and rod, forgings, drawn, extruded tubing, and others. (7,11) The properties of wrought alloys can be improved either by plastic deformation (work-hardening) and heat

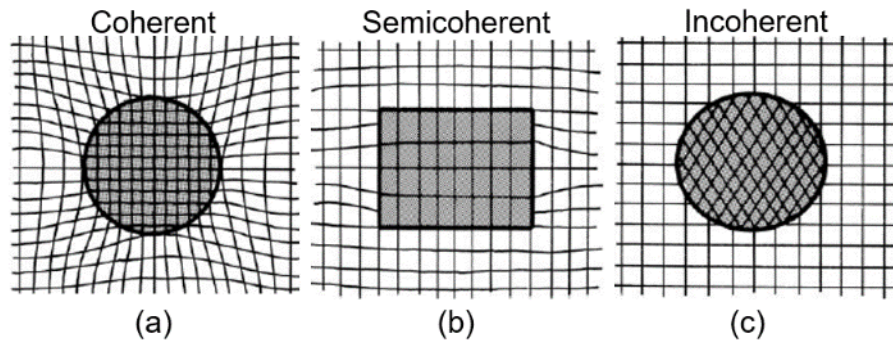
treatment. The common heat treatment used in these alloys is called precipitation- or age-hardening. (7)

Age-hardening is a strengthening mechanism quite common to increase aluminum alloys properties, including yield strength, ultimate strength, fracture toughness, fatigue endurance and hardness. (7) The aging treatment promotes the precipitation of various metastable and stable precipitates out of a supersaturated solid solution (SSSS). The strengthening mechanism occurs by restricting dislocation movement with these precipitates of second phase or intermetallic compounds. (12,13) The sequence performed in aging treatment of most aluminum alloys is:

- **Solution treatment:** this first step involves the heating of aluminum to a temperature high enough (above solvus line) to dissolve large precipitates in the metal after casting, without melting. The adequate temperature in this stage is in a range of 450 to 600 °C for aluminum alloys, although it depends on the alloy composition. This process is also dependent on time, so the metal is exposed in a certain temperature for an appropriate period (“soak time”). (7)
- **Quenching:** the objective in this step is to preserve the SSSS formed in the previous stage, freeze the alloying elements in the aluminum matrix and restrain the diffusive precipitation of coarse particles. Quenching involves rapid cooling near room temperature and its usually performed in cold water. (7,13)
- **Thermal aging:** this step involves various chemical and microstructural transformations that enhances the final strength of aluminum alloys. During aging, the SSSS transforms into clusters or Guinier-Preston (GP) zones, which is a solute-rich region and not yet precipitate particles. The first arrangement of alloying elements into the lattice structure of the aluminum matrix is defined as GP1 zones. The further arrangement of these zones into an ordered pattern, coherent with the lattice matrix, is known as GP2 zones. Even though the interface energy of these zones is low, it provides a small elastic strain in the surrounding matrix, which raises yield strength and hardness. Giving sequence to the aging treatment, these coherent regions grow into semicoherent zones or metastable precipitates with plate- or needle-shape until reaches a complete loss of coherency between precipitate interface/aluminum matrix. (7,12-14)

The level of strengthening depends on the interaction between dislocations and precipitates or transition phases. (12,14) This interaction involves dimension, coherency (Figure 7), strength, spacing and number of particles in the system. (12)

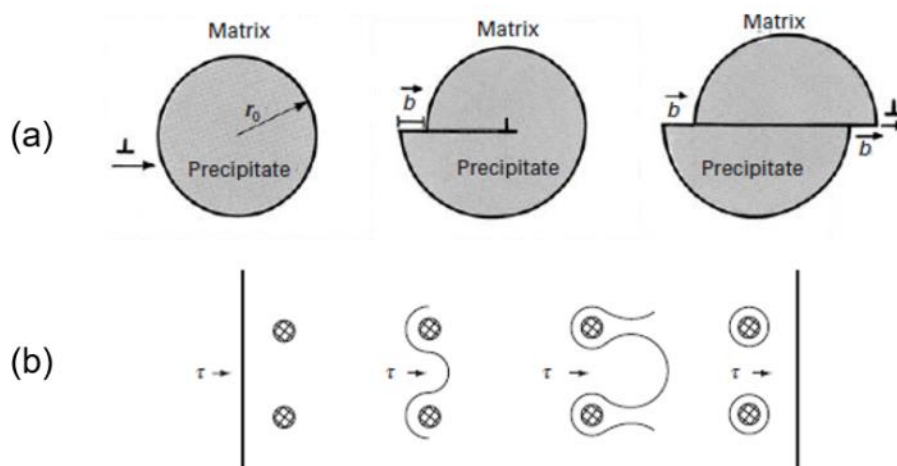
Figure 7 – Coherency between particle and matrix interface. (a) Coherent. (b) Semicoherent. (c) Incoherent.



Source: Adapted from: MEYERS, M.; CHAWLA, K. Mechanical behavior of materials. 2. ed. Cambridge: Cambridge University Press, 2009. 856 p. (12)

In aluminum alloys, GP zones are the first barriers to dislocation motion. However, dislocations can move through these coherent particles in a cutting movement (shear). Incoherent particles resist more to dislocation movement, and it moves by Orowan mechanism, as shown in Figure 8. (12,14) The highest strength and fatigue resistance is achieved when coherent particles transform into incoherent particles, but it lowers ductility. To soften the material and increase ductility, over-aging process can be used to coarse particles from the previous aging.

Figure 8 – Illustration of (a) Particle shear and (b) Orowan mechanism as barriers to dislocation movement.



Source: Adapted from MEYERS, M.; CHAWLA, K. Mechanical behavior of materials. 2. ed. Cambridge: Cambridge University Press, 2009. 856 p. (12)

A temper designation system, consisted of letters and numbers, is also used to specify aluminum alloys according to its temper condition. This system, also developed by the Aluminum Association, defines the type of forging and thermal treatment. Table 1 describes each temper designation.

Table 1 – Temper designation used in aluminum alloys and description.

Temper	Description
F (as fabricated)	Applies to products of forming processes in which no special control over thermal or work hardening conditions is employed.
O (annealed)	Applies to wrought products that have been heated to effect recrystallization, produce the lowest strength condition, and cast products that are annealed to improve ductility and dimensional stability.
H (strain-hardened)	Applies to wrought products that are strengthened by strain hardening through cold working. The strain hardening may be followed by supplementary thermal treatment. H is always followed by two or more digits.
W (solution heat-treated)	Applies to an unstable temper applicable only to alloys that spontaneously age at room temperature after solution heat-treatment.
T (thermally treated)	Applies to products that are heat-treated, sometimes with supplementary strain-hardening, to produce a stable temper other than F or O. The T is always followed by one or more digits.

Source: Adapted from TOTTEN, G. E.; MACKENZIE, D. S. **Handbook of Aluminum**: physical metallurgy and processes. New York: Marcel Dekker, 2003. 1296 p. (11)

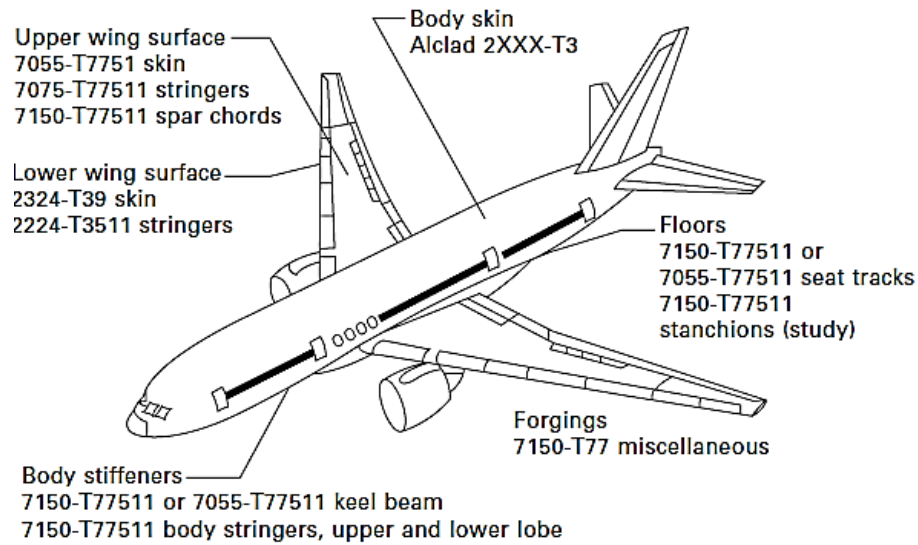
This work focuses on the study of thermally treated (T) aluminum alloys. The AA2024-T351 alloy is solution heat-treated, cold worked and naturally aged. The AA7475-T761 alloy is solution heat-treated and stabilized (over-aged). The properties from both alloys will be discussed in the next section.

3.2.1 General properties of 2XXX and 7XXX aluminum alloys

The 2XXX and 7XXX are classified as heat treatable alloys and contains alloying elements to increase mechanical properties by precipitation hardening. (13,15) The strengthening mechanism from age hardening of these alloys produces coherent clusters of solute atoms. This allows the stabilization of dislocations, which is trapped by these coherent clusters, and promotes the increase in strength and hardness. (16)

Both alloys are widely applied in specific structures, as shown in Figure 9, due to its high strength and light weight.

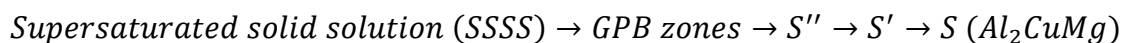
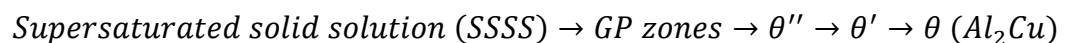
Figure 9 – Application of 2XXX and 7XXX alloys in structures and components from an airplane.



Source: MOURITZ, A. P. (ed.). 8 – aluminum alloys for aircraft structures. In: MOURITZ, A. P. (ed.). Introduction to aerospace materials. Cambridge: Woodhead Publishing Limited, 2012. p. 173-201. (7)

2XXX series are usually used in body skin, lower wing surface and stringers. 7XXX are applied in body stiffeners, keel beam, body stringers, upper and lower lobe, upper wing surface, airplane floors, seat tracks and stanchions. (7)

The 2XXX alloys has Cu as major alloying element, in addition with Mg. The thermal process induced in 2XXX alloys generates small and widely distributed precipitates in the microstructure. The size, distribution, morphology and type of these precipitates contribute to the increase in strength of the material. The precipitation sequences in 2XXX alloys are generally known as follow:



Second phase particles are also present and can be found as constituent phases and dispersoids. The presence of constituent phases is undesired in the microstructure, due to its detrimental contribution to fatigue resistance and fracture toughness. (15) These constituents contain low solid solubility impurities, such as Si and Fe elements. The most common constituents present in AA2024 are

$\text{Al}_{12}(\text{Fe},\text{Mn})_3\text{Si}$, $\text{Al}_6(\text{Fe},\text{Cu})$, $\text{Al}_7\text{Cu}_2\text{Fe}$, Mg_2Si , Al_2Cu , Al_2CuMg , Al_3Fe , Al_2CuLi and Al_6CuLi_3 . (11,17)

The 7XXX alloys has Zn as main alloying element, in addition with Mg and Cu. The strengthening precipitates present in 7XXX alloys is what makes this material one of the highest strengths among aluminum alloys. The precipitation sequence in this alloy is as follow:

Supersaturated solid solution (SSSS) → Clusters → GP I/GP II zones → η' → η

The AA7475 alloy is an improved version of AA7075 alloy, designed to increase damage tolerance through composition and manufacture control. The amounts of Fe and Si are reduced in this alloy, in order to decrease the formation of second-phase constituents. (16) The peak hardening in Al-Zn-Mg-Cu alloys is believed to occur due to the presence of metastable η' phase.(18)¹⁸ The stable η phase is usually found in grain boundaries. (11,16)

3.3 FATIGUE FAILURE IN AIRCRAFT STRUCTURES

The most common failure or damage in aircraft structures is well-known caused by fatigue. This type of failure often occurs at lower stress levels compared to the strength in a monotonic loading, which is a negative condition.

The nature of the service loads during flight and landing, discussed in previous sections, shows how important is the structure design and the suitable alloy selection for an airliner construction. There is a constant conflict between economy versus safety, and the ideal airliner should be constructed with low-weight structure, low operation costs, minimal maintenance, inspections and repairs. (19) The achievement of these concepts are still a challenge and under constant development in the aircraft industry.

3.3.1 Fatigue

Fatigue is basically defined as the mechanical property deterioration of material, under cyclic or fluctuating stresses, until its failure. (12,20) The damage caused by fatigue usually occurs in stresses well under the yield strength of the

material. This is due to the material exposure under repeated elastic stresses, that lead to loss in material strength. (12)

The main causes of fatigue damage from aircraft accidents are stress concentrations and high local stresses. (21) A damage by fatigue usually starts with a crack in a metallic component. This failure is often related to three main physical mechanisms of fatigue crack growth: crack nucleation, stable crack propagation and sudden failure. (22)

Fatigue cracks usually nucleate at pre-existing discontinuities, both on the surface or in the interior of the material. (21) These pre-existing discontinuities may be related to poor drilling and machining, etch pits, porosity, sharp corners, etc. Table 2 shows the variety of nucleation sites that resulted in aircraft accidents, extracted from a review made in 1984.

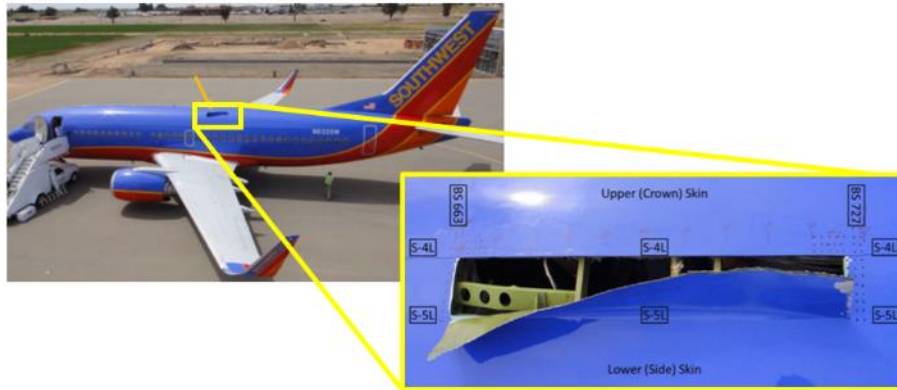
Table 2 – The main nucleation sites and its related number of aircraft accidents.

Nucleation sites	Number of accidents
Bolt, stud or screw	108
Fastener hole or another hole	72
Fillet, radius or sharp notch	57
Nucleation sites	Number of accidents
Thread (other than bolt or stud)	32
Manufacturing defect or tool mark	27
Scratch, nick or dent	26
Surface or subsurface flaw	6
Maintenance-induced crack	4

Source: Adapted from CAMPBELL, G. S.; LAHEY, R. A survey of serious aircraft accidents involving fatigue fracture. *International Journal of Fatigue*, v. 6, n. 1, p. 25-30, jan. 1984. (23)

According to table 2, the nucleation sites with the highest occurrence of accidents are bolt, stud, screw and holes. One example of an aircraft accident in 2011 with a Boeing 737-3H4 operating as Southwest Airlines experienced a fracture at the fuselage skin, about 60 inches long and 9 inches wide, which was sufficient to lose cabin pressurization. The fracture from the upper edge was through the lower rivet row from the lap joint, as show in Figure 10. (24)

Figure 10 – Photograph of Boeing 737-3H4 with a close-up to the fuselage skin crack.

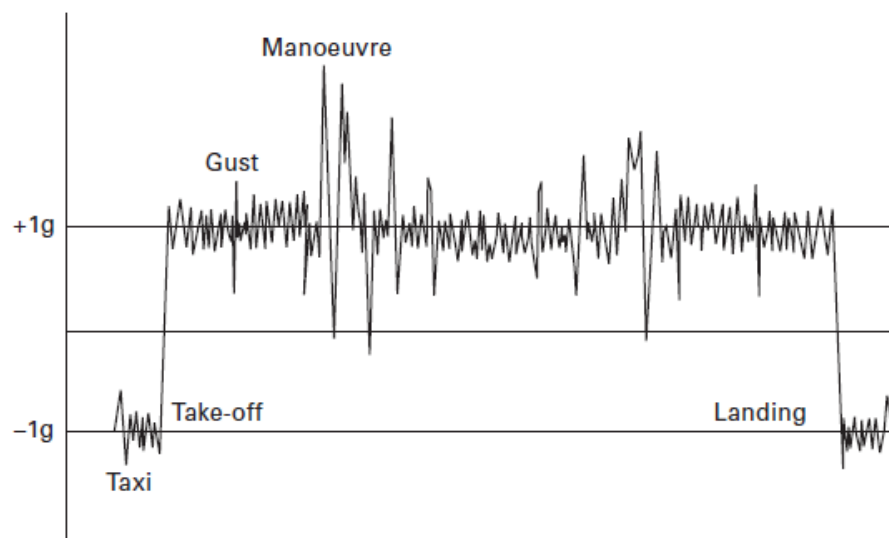


Source: Adapted from National Transportation Safety Board–NTSB (2013) B733depressurisation while en-route, Accident Number:DCA11MA039.(24)²⁴

After fatigue crack is nucleated, it grows within a series of opening and closing movement at the tip of the crack. In relation to the applied load, the crack grows in the normal direction and advances in steps because of loading cyclic.

An example of stress fluctuations on an aircraft wing, from a single flight, is shown in Figure 11. The taxi of the aircraft before take-off and after landing presents low-level stresses to about minus one g . After take-off, the stress levels increase until positive g and fluctuates due to gusts and manoeuvre. (20)

Figure 11 – Fatigue stress level estimative on an aircraft wing, from a single flight cycle.



Source: MOURITZ, A. P. (ed.). 20 – fatigue of aerospace materials. In: MOURITZ, A. P. (ed.). Introduction to aerospace materials. Cambridge: Woodhead Publishing Limited, 2012. P. 469-497. (20)

The random fluctuations in stress as shown in Figure 11 represent a complex condition. To determine the fatigue properties of an aircraft material, one way is to

simplify the cyclic loading and reduce the random stress fluctuation over a component. For typical fatigue-testing methods, some parameters are set to evaluate fatigue properties, which are: (12,20)

- Cyclic stress range, $\Delta\sigma$:

$$\Delta\sigma = \sigma_{max} - \sigma_{min}$$

- Cyclic stress amplitude, σ_a :

$$\sigma_a = (\sigma_{max} - \sigma_{min})/2$$

- Mean stress, σ_m :

$$\sigma_m = (\sigma_{max} + \sigma_{min})/2$$

- Stress ratio, R :

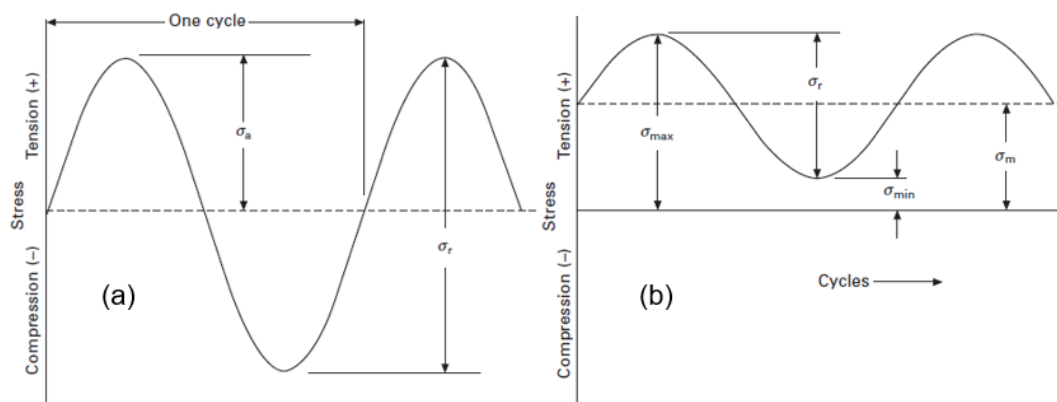
$$R = \sigma_{min} / \sigma_{max}$$

- Stress frequency, f :

$$f = (n^\circ \text{ of cycles})/s$$

The maximum and minimum stress levels are represented, respectively, by σ_{max} and σ_{min} . Figure 12 shows the fatigue parameters for two constant amplitude stress. In the first case (a), the material is being subjected to tension and compression loads (e.g. positive and negative stresses, respectively). And in the other case (b), the material is loaded only in tension (positive stress).

Figure 12 – Fatigue parameters at constant amplitude in (a) tension-compression load and (b) tension-tension load.



Source: Adapted from MOURITZ, A. P. (ed.). 20 – fatigue of aerospace materials. In: MOURITZ, A. P. (ed.). Introduction to aerospace materials. Cambridge: Woodhead Publishing Limited, 2012. P. 469-497. (20)

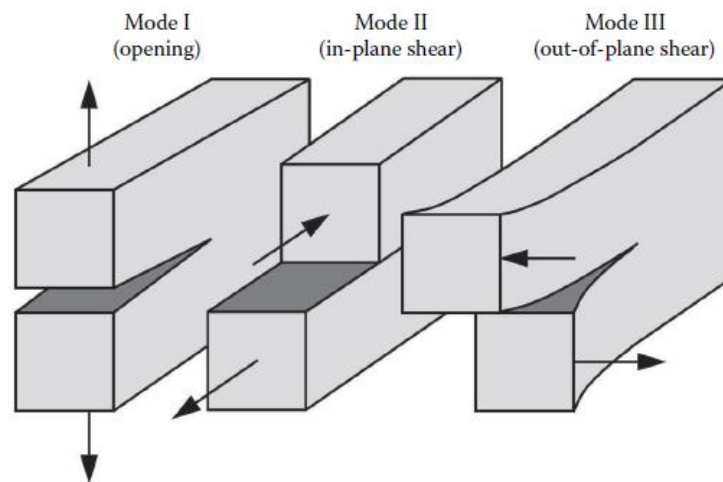
3.3.2 Fatigue crack propagation tests

The fatigue performance of aircraft parts is investigated through several fatigue tests, under standardized methods. The coupons should be designed according to representative and realistic applications. One useful method to determine the fatigue properties of materials is the FCP test on coupons with preexisting crack.

The fundamental concepts from fracture mechanics are approached to FCP, which involves empirical and semiempirical equations. In general, engineering components contain geometrical discontinuities, and their size and shape determine the component strength.

A crack tip can experience three types of loading modes, as shown in Figure 13. Assuming a planar crack, Mode I is defined as the application of a normal load to the crack plane. Mode II is the in-plane shear loading in the direction of the crack advance. Mode III is the out-of-plane shear loading, perpendicular to the crack advance. (20,25)

Figure 13 – Crack tip loading modes.



Source: ANDERSON, T. L. Fracture mechanics: fundamentals and applications. Florida: Taylor and Francis Group, 2017, 661 p. (25)

Considering the plastic deformation around the crack-tip region, one useful and established tool is the linear-elastic-fracture-mechanics (LEFM) approach for crack propagation. As first introduced by George R. Irwin (1958) (26), the stress-intensity factor (K), given by:

$$K = \sigma\sqrt{\pi a}Y$$

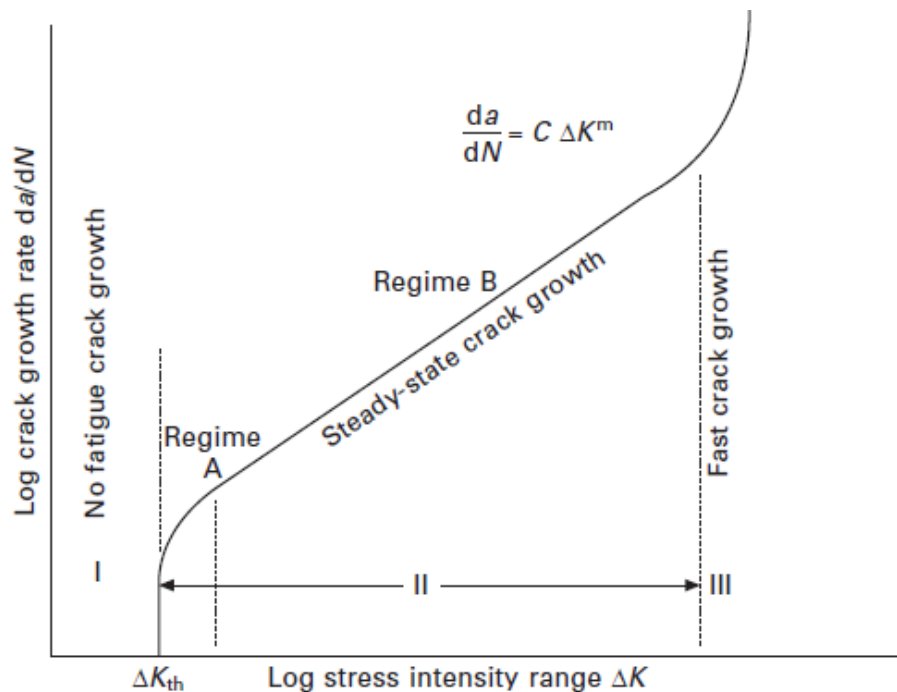
Which is a universal parameter that depends on the crack length (a), stress (σ) and a geometric function (Y), for Mode I cracks, and covers the stress distribution around the crack tip. Paul C. Paris (1963) (27) used the Irwin's concept and introduced an empiric equation that consider a crack growth by a certain rate da/dN in load cycles (N) and a local stress-intensity factor range (ΔK) in a steady-state crack growth rate:

$$\frac{da}{dN} = C\Delta K^m$$

Where C and m are material constants.

FCP curves give information over crack initiation, stable growth and consequent failure. Figure 14 demonstrates a common log-log FCP curve for metals, in terms of stress intensity factor range (ΔK), and crack growth rate (da/dN), divided into three regions: the threshold region (I), the steady-state crack growth or Paris region (II) and the final region of fast crack growth (III).

Figure 14 – Common log-log FCP curve regarding crack growth rate da/dN and stress intensity factor range ΔK .



Source: MOURITZ, A. P. (ed.). 20 – fatigue of aerospace materials. In: MOURITZ, A. P. (ed.). Introduction to aerospace materials. Cambridge: Woodhead Publishing Limited, 2012. p. 469-497. (22)

The threshold region (I) is a condition where the fatigue-crack growth do not occur due to a low range of ΔK . The crack only starts to grow when ΔK rises above a

threshold intensity-factor range (ΔK_{th}). Region II, or Paris region, covers a narrow crack growth (Regime A) and a stable crack growth rate (Regime B) in a slope of m . The final region (III) involves a severe fatigue condition, with fast crack growth until fracture. This occurs when ΔK achieves the fracture toughness (K_c) of the material. (20,28,29)

3.4 DAMAGE TOLERANCE IMPROVEMENT

Damage tolerance is defined as the ability of a structure or component to tolerate fatigue, corrosion, or other damages before it reaches a critical level. (30) In the aerospace research field, the residual stress-based methods are usually investigated due to their effect on component service life, and is becoming a potential cost-effective solution. (31) Residual stress is defined as self-equilibrating stresses present in an elastic body with no external temperature or force application. (32) It can be induced, unintentionally, by several manufacturing processes, such as non-uniform plastic deformation (rolling, casting, machining), steep thermal gradients (quenching, welding, laser heating) and phase transformation (martensitic transformation in steel). (33)

Residual stresses can be classified according to three types of length scales. Type I refers to a macro-stress, containing uniform stresses over a large number of grains and material fracture. Basically, it evolves the scale of the structure. Micro-stresses, such as Type II contains uniform stresses over the scale of various grains or phase. The uniform stresses over a smaller length, usually from dislocations and vacancies, are from Type III, which is also a micro-stress. (32,34,35) In the scope of this study, only Type I will be considered.

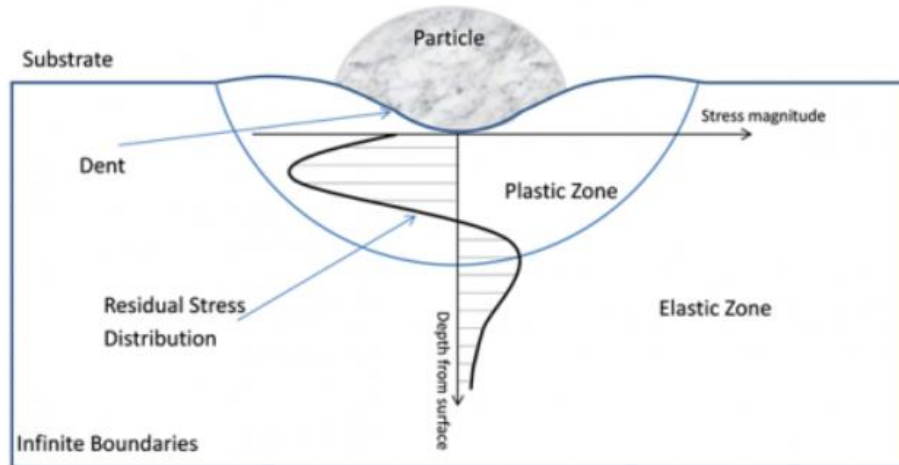
The nature of the residual stress applied in a component exists as a tensile (+) or compressive (-) stresses, and both always occur mutually. (36) The presence of tensile residual stress near surface is well-known to be more prejudicial for fatigue performance, due to its contribution over the increase in crack propagation rate. However, compressive residual stress retards the crack propagation growth and are very desirable regarding the prolongation on the fatigue life of structures. (37,38)

The purpose introduction of compressive residual stresses in probable fatigue crack growth path is also an alternative technique to improve fatigue performance without increasing structural weight. (39) Examples of these techniques that affects the

compression stresses around the fatigue crack tip are as such: shot peening, laser-shock peening and laser heating. (40-42)

A typical residual stress profile is shown in Figure 15 promoted by shot peening, with compressive stress near surface, and tensile stress at further depth. (43)

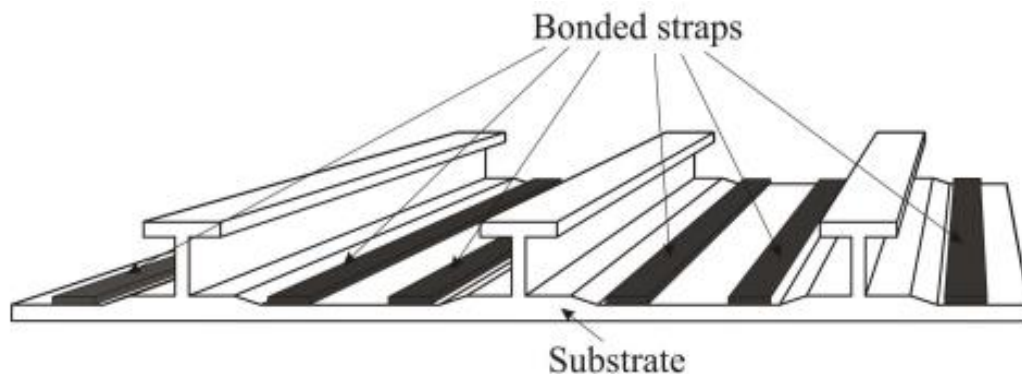
Figure 15 – Typical profile of RES induced by shot peening, with compressive stresses close to the surface, and tensile stresses in the remnant length of the material.



Source: Adapted from UNIVERSITY OF WATERLOO. Residual Stress. Available in: <https://uwaterloo.ca/fatigue-stress-analysis-lab/research/residual-stress>. Access in: 29th april 2022. (44)

Some other existing techniques may involve design approach, such as crack-stopper strips mechanically joined or bonded (Figure 16) applied on specific fuselage areas to tailor mechanical performance and restrain crack propagation. (45,46)

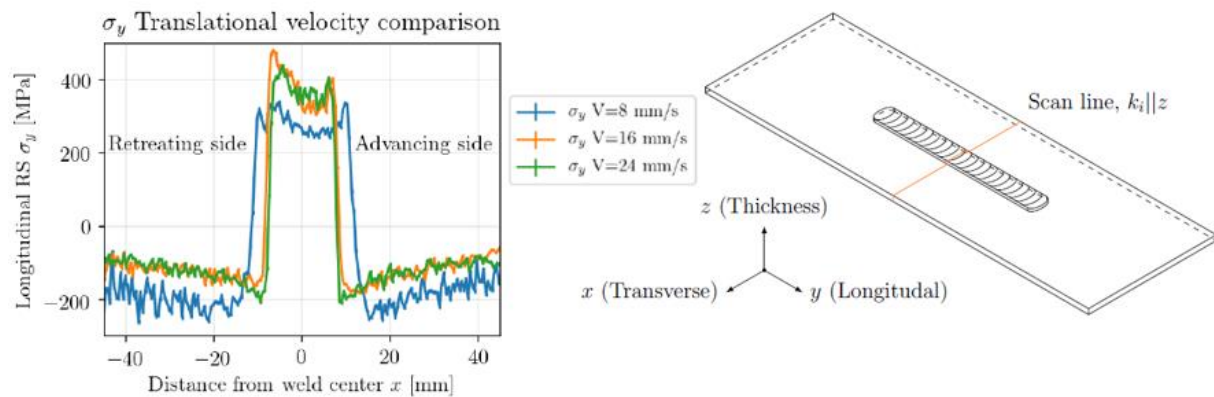
Figure 16 – Example of bonded straps between stringers, applied in aircraft structures.



source: BOSCOLO, M.; ZHANG, X. Bonded crack retarders for aircraft integral metallic structures: a sensitivity analysis of design parameters. Structures, Structural Dynamics and Materials Conference. American Institute of Aeronautics and Astronautics, 2012. (47)

The investigation of residual stress and fatigue performance from FS technique was first mentioned in a study with coated Ti-6Al-4V sheets. (3) FS is also a process that involves local plastic deformation and heating, which may introduce compressive residual stress. From FS process, there is a mismatch in thermal expansion between the material deposited and the substrate, and different cooling rates on the substrate material, due to the additional material being deposited. (3) These characteristics results in inhomogeneous cooling, generating residual stresses. (3) Figure 17 illustrates the shape of RES along the scan line from longitudinal σ_y of Ti-6Al-4V deposits on similar substrate. The tensile stresses are depicted in the deposit region, denoted as active zone, and compressive stresses in the rest of the material, denoted as a compensative zone. The process asymmetry also affects the residual stress distribution between RS and AS, where higher compressive stresses are observed in RS.

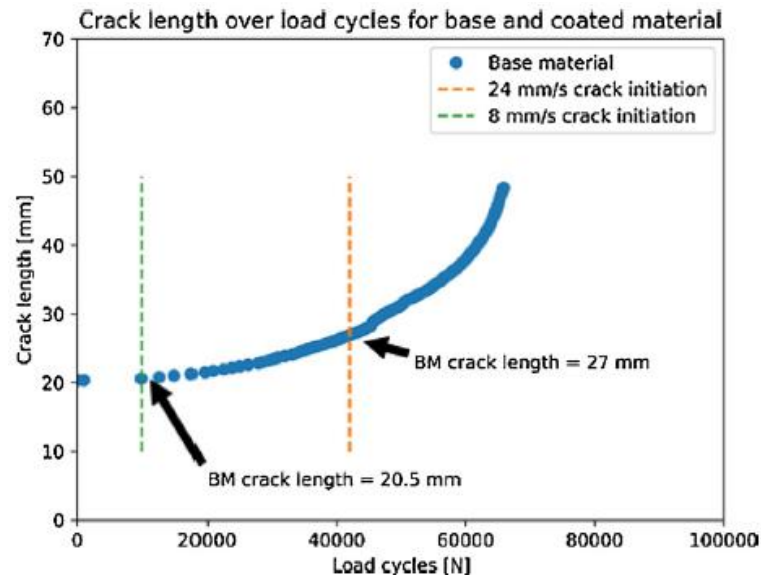
Figure 17 – RES distribution along the scan line for Ti-6Al-4V deposits on similar substrate by FS.



Source: Adapted from DOVZHENKO, G. Characterization of residual stresses in friction surfacing of Ti and Al alloys. 2020. Thesis (Doctoral degree) – Faculty of Mathematics, Informatics and Natural Sciences Department of Physics, Universität Hamburg, Hamburg, 2020. Available in: <https://ediss.sub.uni-hamburg.de/handle/ediss/8902>. Access in: 15th April 2020. (47)

Figure 18 shows the increase in lifetime before crack initiation in coated Ti-6Al-4V specimens by FS, compared to BM. The crack initiation in coated specimens by FS are delayed.

Figure 18 – Crack length versus load cycles in Ti-6Al-4V specimens from base material and deposited with different deposition speed.



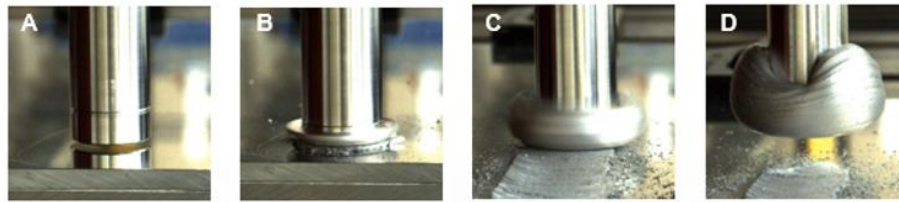
Source: DOVZHENKO, G. Residual stresses and fatigue crack growth in friction surfacing coated Ti-6Al-4V sheets. *Journal of Materials Processing Technology*, vol. 262, p. 104-110, 2018. (3)

3.5 FRICTION SURFACING LAYER DEPOSITION

FS is a solid-state deposition process based on plastic deformation and frictional heat. This process has a patent since 1941, and ever since, several studies were published with plenty material combinations. (48-62) This process involves an interesting possibility to join dissimilar materials, or even non-weldable metals, such as 2XXX and 7XXX aluminum alloys.

The FS process, as illustrated in Figure 19, consists of process steps and process stages. In the first process step, the stud is positioned above the substrate surface at the pre-set starting position (A) where a defined rotational speed is applied. Initial contact of the rotating stud tip with a pre-programmed axial force, leads to the plasticizing stage (B), where initially frictional heat between the stud tip and the substrate surface leads to plasticizing of the stud tip. When a predefined stud shortening is reached, a relative translational movement between substrate and rotating stud is superimposed, leading to the deposition stage (C), where plasticized stud material is deposited onto the substrate surface along the pre-programmed FS path. In a last step, the spend stud is retracted from the substrate, finishing the process (D). A revolving flash around the stud tip is observed during FS layer deposition, which is a part of the soft material that is squeezed out of the contact plane and pressed upwards.

Figure 19 – Process steps from FS layer deposition. Starting position (A). Plasticizing stage (B). Deposition stage (C). Final stage (D).



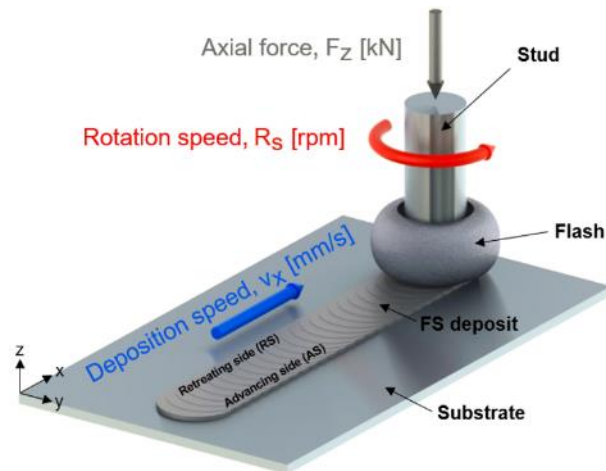
Source: The author.

3.5.1 FS parameters and process monitoring

There are two main types of process control during FS: force and position controlled. The adjustable process parameters are dependent on the type of process control implemented.

The adjustable FS process parameters in force control mode, which is the control mode used in this study, are: axial force (F_z), rotation speed (R_s) and deposition speed (v_x), as represented in Figure 20.

Figure 20 – Schematic representation of the FS process with designation of the main FS process parameters.

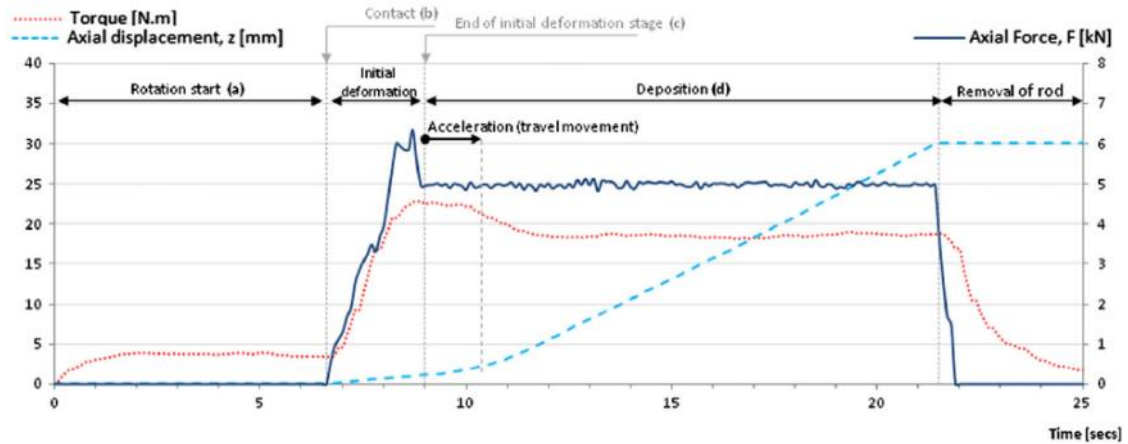


Source: The author.

Figure 21 covers the monitoring of process parameters and torque evolution in the deposition of AA6082 over AA2024 by FS. As previously described, in the first step, a rotation speed in the stud is developed by the machine. Then, the stud moves towards the substrate surface and contact occurs, which can be observed by the increase in axial force and torque. In the initial contact, the stud tip is plasticized and when the stable plasticization is achieved, a travel movement is imposed, and the

deposition stage starts. The removal of the stud occurs when the desired deposit length is achieved, and it can be seen by the drop of both axial force and torque.

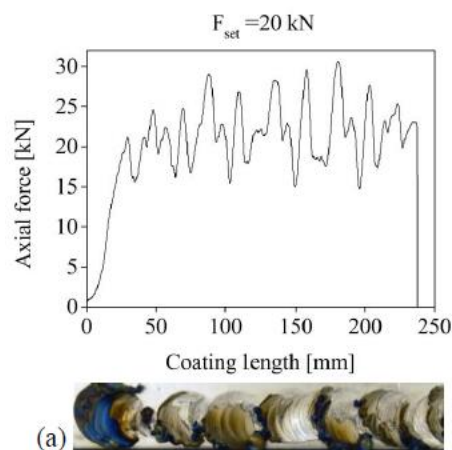
Figure 21 – Monitoring of axial force, torque and stud axial displacement in Z-direction of friction surfaced AA6082 over AA2024.



Source: GANDRA, J.; MIRANDA, R. M.; VILAÇA, P. Performance analysis of friction surfacing. *Journal of Materials Processing Technology*, vol. 242, p. 1676-1686, 2012. (62)

The plotted parameters allow to observe its evolution and stability of the process. In force control mode, the axial force evolution during deposition is a key factor to process stability and deposit appearance homogeneity. Figure 22 depicts a deposit surface appearance of Ti-6Al-4V and the recorded axial force *versus* coating length.

Figure 22 – Recorded axial force and deposit surface appearance of Ti-6Al-4V titanium alloy.

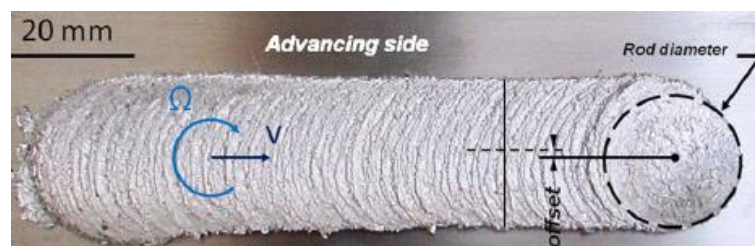


Source: FITSEVA, V. Friction surfacing of titanium grade 1 and Ti-6Al-4V. 2016. 116 f. Thesis (Doctorate degree) - Technischen Universität Hamburg-Harburg (TUHH), 2016. (63)

The desired constant axial force value of 20 kN was barely kept, and oscillations between 15 kN and 35 kN is observed. These force peaks resulted in discontinuous material transfer, generating a heterogeneous surface appearance.

The deposit produced by the same parameters shown in Figure 21 is presented in Figure 23. Once the machine kept the axial force values near constant during deposition stage, continuous material transfer occurs and homogeneous deposit appearance is generated.

Figure 23 – Deposit surface appearance generated from friction surfaced AA6082 over AA2024.



Source: Adapted from GANDRA, J.; MIRANDA, R. M.; VILAÇA, P. Performance analysis of friction surfacing. *Journal of Materials Processing Technology*, vol. 242, p. 1676-1686, 2012. (62)

In general, the deposit surface quality is related to the capability of constant axial force application during deposition. This capability is also dependent of a right set of process parameters, which are discussed in the next section.

3.5.2 Influence of FS process parameters

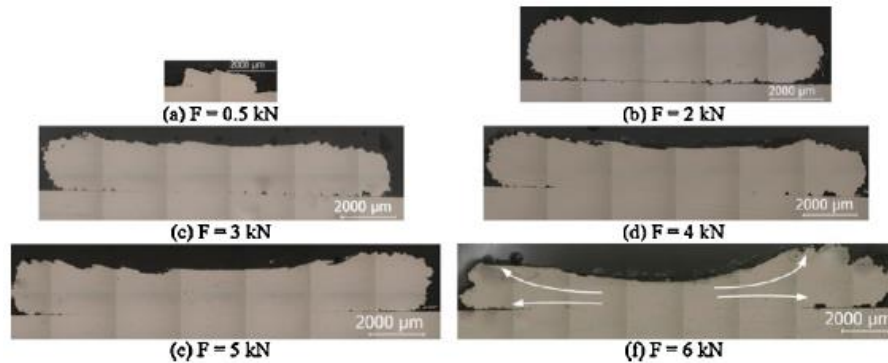
The influence of process parameters in deposit geometry is also dependent of chemical and physical properties of the material, which turns it into a complex correlation. According to several studies, some trends were found and a summary will be described as follow. (49,64,65)

The deposit geometry is characterized as the following: deposit thickness (t), total width (W_T) and bonded width (W_B). The bonded width covers the bonded interface effectively adhered between the deposit and the substrate, and the total width covers the bonded width in addition with the width from the unbonded edges.

The axial force is generally associated with improvement in bonding from the interface between deposit and substrate. This parameter also affects the width and thickness from deposits, as shown in Figure 24, in the deposition of mild steel over mild steel. Axial force up to 3 kN resulted in poor bonded interface, with presence of

voids. With the increase in force up to 6 kN, the sound bonding interface is achieved, although the excess of axial force led to a depression in the center of the deposit.

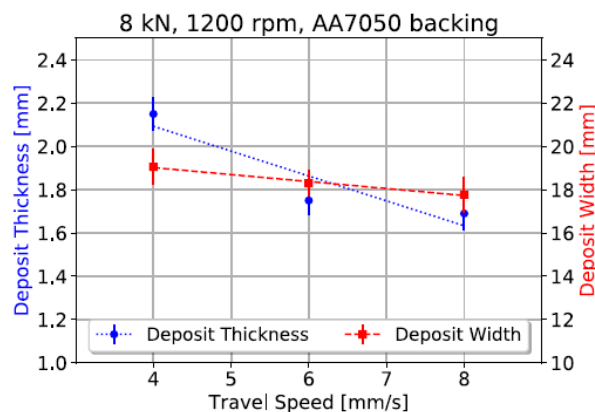
Figure 24 – Influence of axial force on deposit geometry of friction surfaced mild steel over mild steel.



Source: GANDRA, J.; MIRANDA, R. M.; VILAÇA, P. Performance analysis of friction surfacing. *Journal of Materials Processing Technology*, vol. 242, p. 1676-1686, 2012. (62)

The deposition speed can be related to the rate of material transferred from the deposit to the substrate. As such, this parameter generally affects deposit thickness and width. This is observed in the deposition of AA5083-H112 over AA7050-T7451, as shown in Figure 25. The increase in deposition speed (travel speed) from 4 mm/s to 8 mm/s resulted in thinner and narrower deposits.

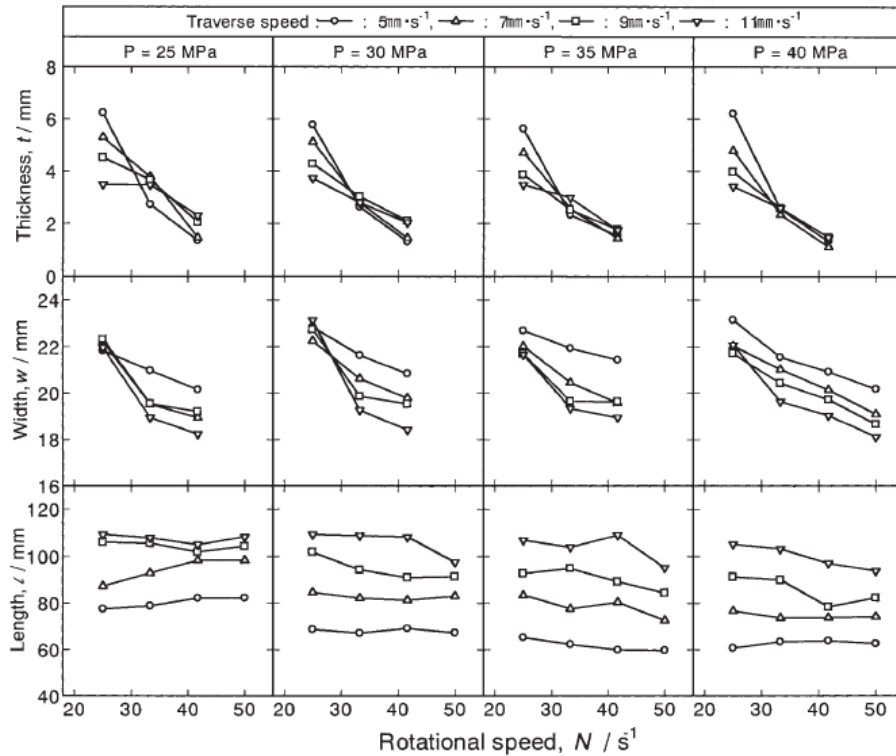
Figure 25 – Influence of deposition speed on deposit geometry of friction surfaced AA5083 over AA7050-T7451 alloy.



Source: KALIEN, Z.; RATH, L.; ROOS, A.; KLUSEMANN, B. Experimentally established correlation of FS process temperature and deposit geometry. *Surface and Coatings Technology*, vol. 397, n. 126040, 2020. (64)

The influence of rotation speed on friction surfaced AA5052 is shown in Figure 26. The thickness and width decrease with the increase in rotation speed.

Figure 26 – Influence of rotation speed on deposit geometry of friction surfaced AA5052 alloy.



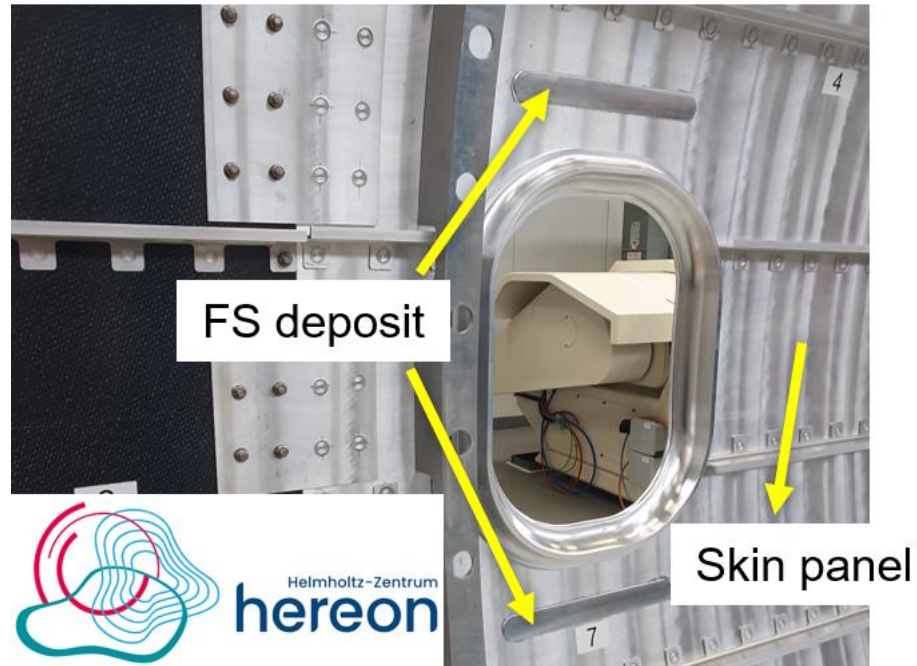
Source: SAKIHAMA, H.; TOKISUE, H.; KATOH, K. Mechanical properties of friction surfaced 5052 aluminum alloy. *Materials Transactions*, vol. 44, p. 2688-2694. 2003. (48)

3.5.3 Potential application of FS

As shown in previous sections, an aircraft is exposed to different types of loads (shear, compression and tension) during service. The aircraft industry seeks for technologies and materials to enhance the service life in components and structures, diminishing the maintenance and replacement of damaged parts.

It was found that FS can result in compressive stresses in the surrounding region from the active zone (deposit). This residual stress state achieved from FS has a potential use as crack growth retardation. The layers deposited by FS can be applied to specific regions, preferably near high stress concentration regions. One example of FS layer applied with this goal is shown in Figure 27, with FS deposits near an aircraft window and between stringers. This aluminum panel is exposed at Solid-state Materials Processing department, at Helmholtz-Zentrum Hereon institute (Germany).

Figure 27 – Fuselage panel with FS deposits as an example of application from this technique.



Source: Solid-state Materials Processing, Institute of Materials Mechanics, Helmholtz-Zentrum Hereon (Germany).

4 MATERIALS AND METHODOLOGY

This section gives an overview of the materials, equipment and experimental procedures used to develop the deposition of AA2024 layers on AA7475 sheets with the FS technology. Furthermore, the specimen preparation, characterization and mechanical testing are described in detail.

4.1 MATERIALS

The materials present in this study are two heat treatable aluminum alloys, provided by EMBRAER: AA2024-T351 in round studs with 19.05 mm diameter and 200 mm length, in extrusion condition, and AA7475-T761 sheets with 300 mm x 200 mm x 3.2 mm as substrate in hot-rolled condition (Figure 28). The chemical composition of both alloys was obtained by optical emission spectrometry (OES), which is presented in Table 3.

Figure 28 – AA7475-T761 substrate and AA2024-T351 stud material provided by EMBRAER SA.



Source: The author.

Table 3 – Chemical composition of AA2024-T351 stud and AA7475-T761 sheet.

wt. %	Al	Cu	Zn	Si	Fe	Mn	Mg	Cr	Ti
AA2024-T351 (stud)	93.1	4.4	0.02	0.06	0.24	0.64	1.5	0.02	0.02
AA7475-T761 (sheet)	90.48	1.5	5.4	0.03	0.08	<0.01	2.3	0.19	0.02

Source: The author.

4.2 METHODOLOGY

4.2.1 Friction Surfacing Equipment

FS was performed using a custom designed equipment (HLR RAS 1 by H. Loitz Robotik), located in the Solid-state Materials Processing (WMP) department (Helmholtz-Zentrum Hereon, Germany). This equipment is capable to deliver high process loads and stiffness, with axial forces up to 60 kN, 6000 rpm of rotational speed and a torque of 200 N.m. The machine is equipped with sensors for the simultaneous monitoring of forces in three axial directions and a torque sensor in the spindle. The maximum stud length permitted is 500 mm and is fixed into the machine by a stud/rod clamping. A profile table is used for the working space, which allows the fixation of clamping devices, and it is made with aluminum alloy to provide a good heat transfer. Both substrate and stud are clean with acetone and compressed air to remove any oxide layer or contamination, according to standard practices conducted in WMP. An overview of the machine is shown in Figure 29.

Figure 29 – Illustration of HLR RAS 1 machine used to produce layer FS deposition process at Hereon (Germany).



Source: FITSEVA, V. Friction surfacing of titanium grade 1 and Ti-6Al-4V. 2016. 116 f. Tese (Doutorado) - Technischen Universität Hamburg-Harburg (TUHH), 2016.(63)⁶⁴

The substrate is clamped onto the working table with clamping devices. AA7050 aluminum plate with 10 mm thickness is used as backing plate, fixed between the AA7475-T761 substrate and machine table, to increase heat extraction during process, as suggested in preliminary studies from WMP. The stud clamping material used in this work is from X 37 steel.

4.2.2 Process Parameters

An initial process window for the main process parameters (i.e., axial force, rotation speed and deposition speed) was determined based on trials and knowledge from WMP and UEPG. The criteria used to determine the boundaries of the process window was primarily process stability and visual appearance. This analysis was used to produce specimens for further characterization and testing purposes.

A design of experiments (DoE) methodology (one-factor-at-time) was applied to select optimal level settings intending to understand the relationship between the variables and the influence in specific properties. The three main process parameters were varied at three levels each, resulting in 27 specimens. The process parameters chosen for this work is shown in Table 4.

Table 4 – Process window for the main process parameters (axial force, rotation speed and deposition speed).

Axial force [kN]	8	10	12
Rotation speed [rpm]	900	1100	1300
Deposition speed [mm/s]	8	10	12

Source: The author.

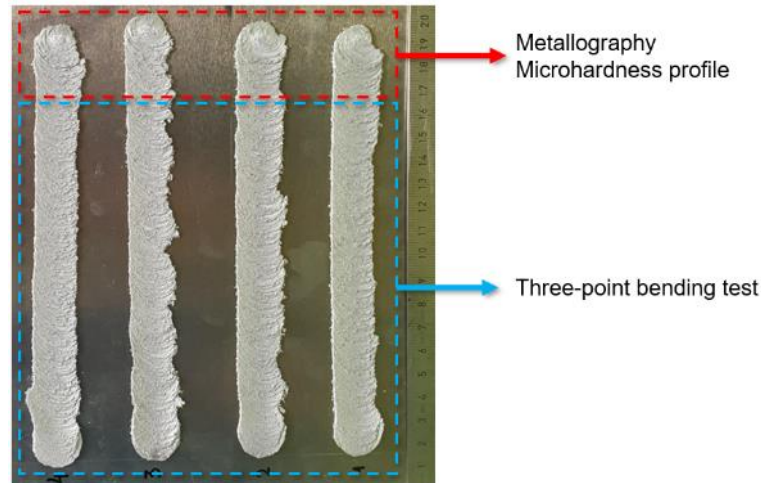
To produce specimens for FCP test, one process parameter set is chosen according with the selection criteria as follow:

- Satisfactory surface appearance and process stability.
- Effective bonding width between 10 mm and 15 mm.
- Satisfactory adhesion between deposit and substrate (evaluated by bending test).

4.2.3 Specimen Extraction Plan

FS deposits with total length of 170 mm were produced for metallography, microhardness and bending tests. The surface morphology of the entire deposit length was visually analyzed and recorded with digital camera. The cross sections were extracted near deposit end, in a water-cooling cut-off machine (Axitom-5 by Struers) provided by WMP, for metallography and microhardness profile. The remaining length of ~140 mm from each deposit was extracted and prepared for three-point bending test. The extraction plan is portrayed in Figure 30.

Figure 30 – Specimen extraction plan for metallography, microhardness profile and three-point bending test.



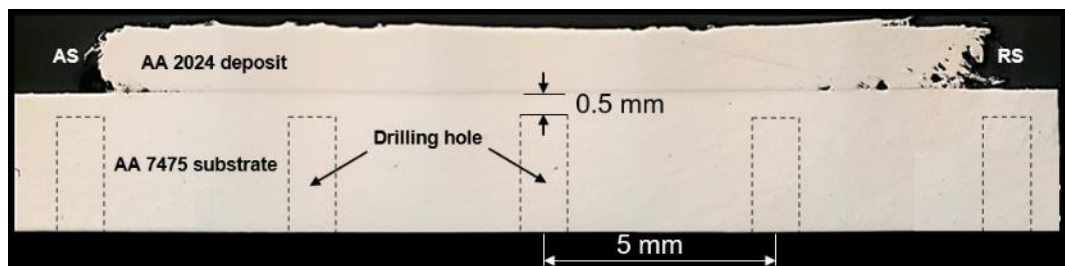
Source: The author.

4.2.4 Temperature Measurement

To investigate the maximum process temperature achieved on the deposition of two heat-treatable aluminum alloys (AA2024 and AA7475), temperature is measured by IR-camera (ImageIR 8300 by InfraTec) and thermocouples, both provided by WMP.

For IR imaging, stud and substrate were painted in black to prevent interferences caused by reflective surfaces. The images are processed with the IRBIS 3 Professional by InfraTec software using a temperature range of 60 to 300 °C and frame rate of 80 Hz. Six thermocouples K-type with 0.65 mm diameter are placed 0.5 mm below substrate surface and spaced between 5 mm each to guarantee that the layer width is covered, as illustrated in Figure 31.

Figure 31 – Schematic positioning of thermocouples in the substrate for temperature measurements.



Source: the author.

4.2.5 Metallographic Analysis

The cross-section characterization and the microstructure feature of the deposits are initially performed by standardized metallographic procedures (*ASTM E3 - Standard Guide for Preparation of Metallographic Specimens*).

To analyze the cross section, specimens are cold embedded in *Demotec 20* polymer resin. Then, the grinding and polishing steps are executed on an automatic machine (TegraPol-31 by Struers) provided by WMP, with custom automatized program as detailed in Table 5.

Table 5 – Detailed steps for grinding and polishing.

Abrasive paper (FEPA/ANSI)	Particle granulometry	Lubrication	Force	Rotation (holder/disc)	Time
#320/#240	46 μm	Water	15 N		20 s
#800/#400	22 μm	Water	15 N	200 rpm/150	30 s
#1200/#600	15 μm	Water	15 N	rpm	40 s
#2000/#800	10 μm	Water	15 N		40 s
Cloth (FEPA/ANSI)	Particle granulometry (μ)	Lubrication	Force	Rotation (holder/disc)	Time
MD Largo	9 μm	-			60 s
MD Dac	3 μm	-	15 N	200 rpm/150	120 s
MD Nap	1 μm	DP blue		rpm	240 s
MD Chem OPS	0.25 μm	Water			20 s

Source: The author.

Optical analysis and imaging of specimen's cross-section are performed with Keyence VHX-6000 digital microscope, provided by WMP. The deposit geometries, such as thickness (t), total width (W_T) and bonded width (W_B) are measured by the microscope software. At least five measures of deposit thickness from the W_B region, equi-spaced in 2 mm, are taken to obtain an average.

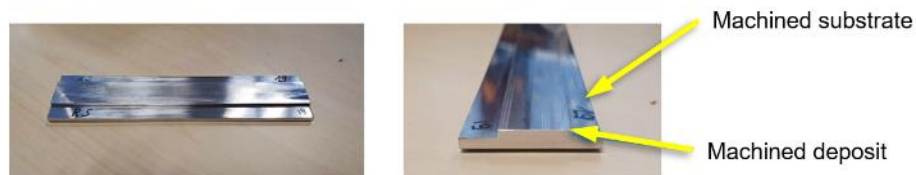
An electrochemical etching with Barker's reagent (aqueous solution of HBF_4) at voltage of 24 V for 100 s was used to reveal the microstructure of FS specimens. After etching, the microstructure was analyzed with LectroPol-5 by Struers provided by WMP, using polarized light.

Scanning electron microscope (SEM) (Quanta™ 650 FEG) equipped with energy dispersive spectroscopy (EDS) provided by WMP was used to investigate microstructure features and interface between deposit/substrate. SEM (FEG-MEV, TESCAN, Mira 3) provided by UEPG was also be used to investigate fracture surfaces from tensile and FCP test specimens.

4.2.6 Bending Test

Three-point bending tests were used to examine the deposit adherence in the substrate. As illustrated in Figure 32, specimens with 140 mm length were cut off and machined to remove surface roughness and to eliminate crack nucleation sites at the unbonded edges from RS and AS.

Figure 32 – Exemplary friction surfacing three-point bending test specimen after machining, showing side view (left) and transverse view (right) of the specimen.



Source: The author.

According to *ASTM E190 - Standard Test Method for Guided Bend Test for Ductility of Welds*, the bending tests were performed at 2 mm/min with 80 mm distance between rollers, using a 30 mm diameter punch in a universal testing machine (Zwick-Roell) provided by WMP, as shown in Figure 33.

Figure 33 – Universal testing machine used for three-point bending test at Hereon (Germany).



Source: The author.

4.2.7 Microhardness Test

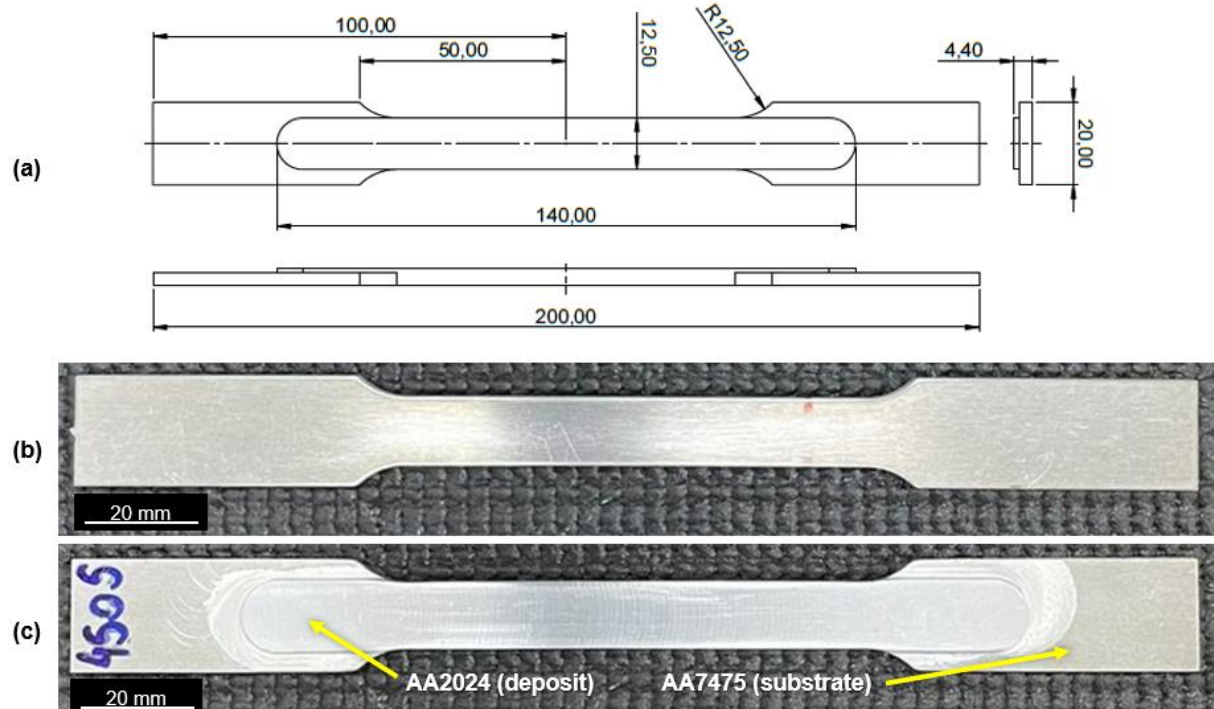
Microhardness Vickers (HV0.2) measurements were taken using Struers DuraScan provided by WMP, with penetration time of 12 s and load of 0.2 N. Lines of

indentations were made perpendicularly with the interface between deposit/substrate to investigate the microhardness profile. The microhardness map was performed with distance of 0.25 mm between indentations, to evaluate the extension of the heat affected zone (HAZ).

4.2.8 Tensile Test

To verify the process influence on tensile mechanical properties, e.g. yield strength (YS), elongation and ultimate tensile strength (UTS), tensile tests were performed using a MTS 370.25 Load Frame by Landmark servo-hydraulic machine with continuous axial displacement, provided by UEPG. The test was conducted at room temperature and performed at 1.5 mm/min, with the deposit length perpendicular to the load. The flat specimens for tensile tests were machined according to *ASTM E8/E8M-16 – Standard Test Methods for Tension Testing of Metallic Materials* standard, as shown in Figure 34, with dimensions in millimeters.

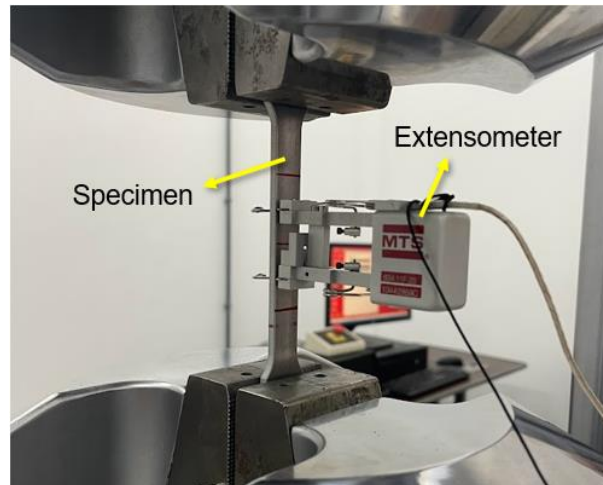
Figure 34 – (a) Dimension specification from tensile test specimens. (b) AA7475-T761 BM and (c) FS specimen with post machined layer.



Source: The author.

An axial extensometer (MTS by Landmark) provided by UEPG was used to measure the displacement in the center of the specimen, as shown in Figure 35.

Figure 35 – Extensometer by MTS.

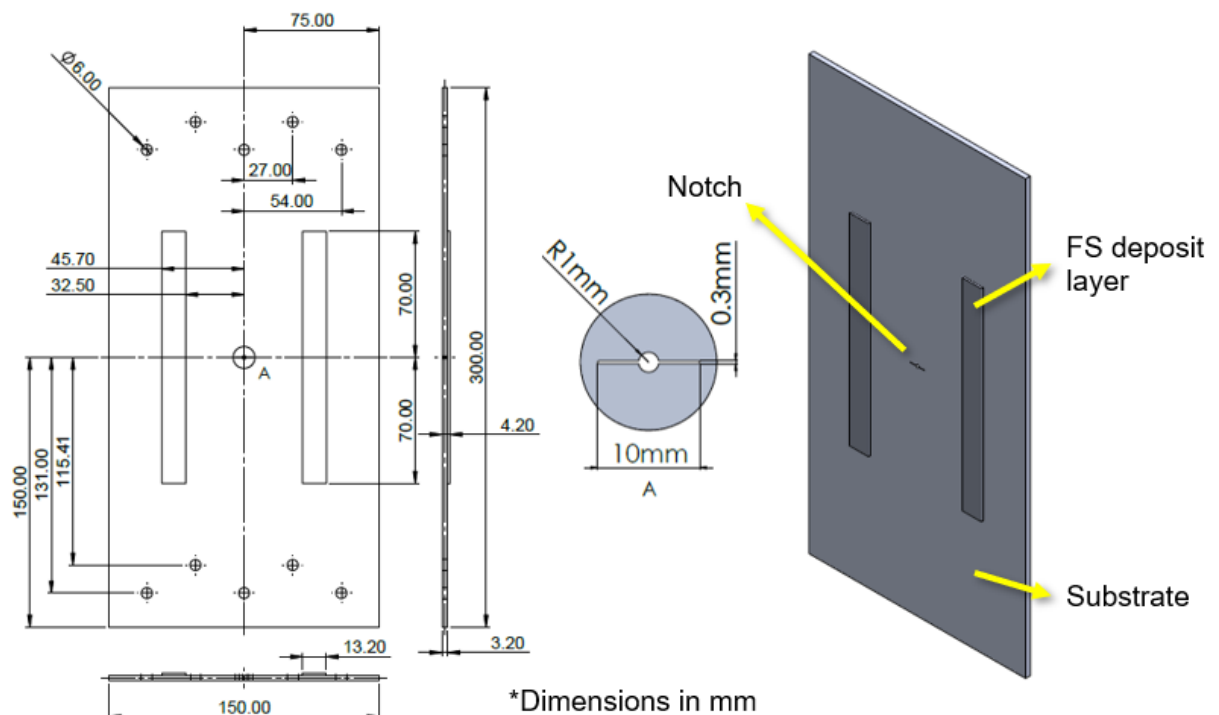


Source: the author.

4.2.9 Fatigue Crack Propagation Test

To investigate the FS process influence on crack propagation rate, FCP tests were performed on middle tension (MT) specimen geometry, with two deposits, as shown in Figure 36. The specimen's dimensions are 150 mm width, length of 300 mm and thickness of 3.2 mm. The notch was prepared by electrical-discharge machining, with 10 mm length and 0.3 mm high.

Figure 36 – Specimen dimension and details for FCP test.

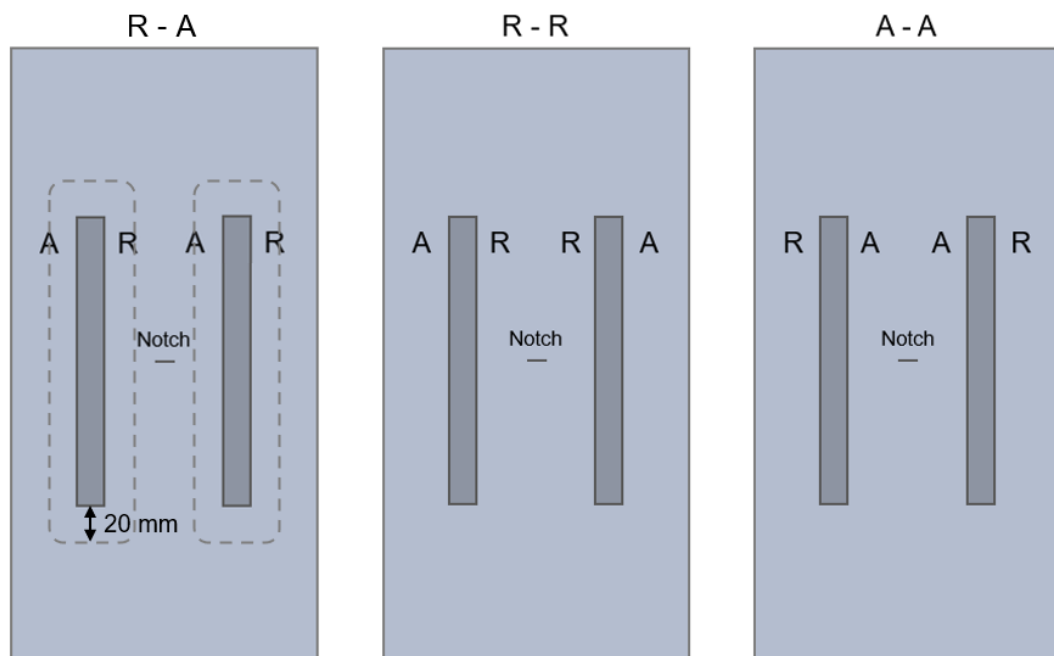


Source: the author.

The FS layers are deposited parallel to the rolling direction and perpendicular to the crack propagation. From a total number of 6 deposited specimens by FS, 2 specimens are produced with both layers with RS within the notch side, named as R-R and 2 more specimens have AS in the notch side, named as A-A. Both configurations have only the deposit's edges post-machined, in accordance with Figure 35.

A post-machining step of around 0.1 mm deep and 20 mm wide is done in the sheet surface and the deposit's edges, in order to evaluate the impact and influence on FCP rate of a post-machining step. Thus, 2 more specimens are produced with alternate edge side in the notch side, named as R-A, as depicted in Figure 37.

Figure 37 – Specimen configuration for FCP tests.



Source: The author.

All specimens are produced and tested in accordance with *ASTM E647 – Standard Test Method for Measurement of Fatigue Crack Growth Rates*. The test is conducted in a servo hydraulic machine (MTS by Landmark, provided by UEPG) for A-A and R-R specimen configuration, in tension-tension mode, at maximum load (P_{max}) of 28 kN, frequency (f) of 10 Hz and stress ratio of $R = \sigma_{min}/\sigma_{max} = 0.1$. Same test parameters are used for specimens with R-A configuration, although tested with another servo hydraulic machine (SCHENK, provided by Helmholtz-Zentrum Hereon). The crack size is measured either by direct method (for R-A specimen configuration) and compliance method (for A-A and R-R specimen configuration). Clip-gage (MTS by Landmark, provided by UEPG) is used to measure the elastic compliance of the

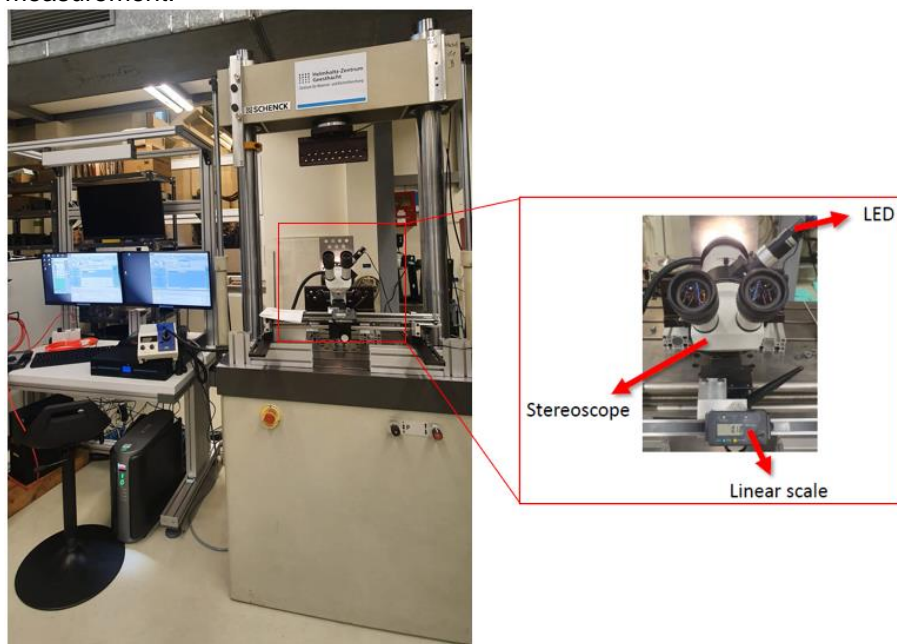
specimen and fixed within the notch, as shown in Figure 38, for the compliance method. Stereoscope (Wild M3Z by Leica, provided by Helmholtz-Zentrum Hereon) accoupled with a linear scale and LED light is used to measure the crack growth in every 2,500 FCP cycles, for the direct method (Figure 39).

Figure 38 – Servo hydraulic machine MTS by Landmark, specimen, clamping and clip-gage system.



Source: the author.

Figure 39 – Servo hydraulic machine by SCHENCK and stereoscope system used for crack growth measurement.



Source: the author.

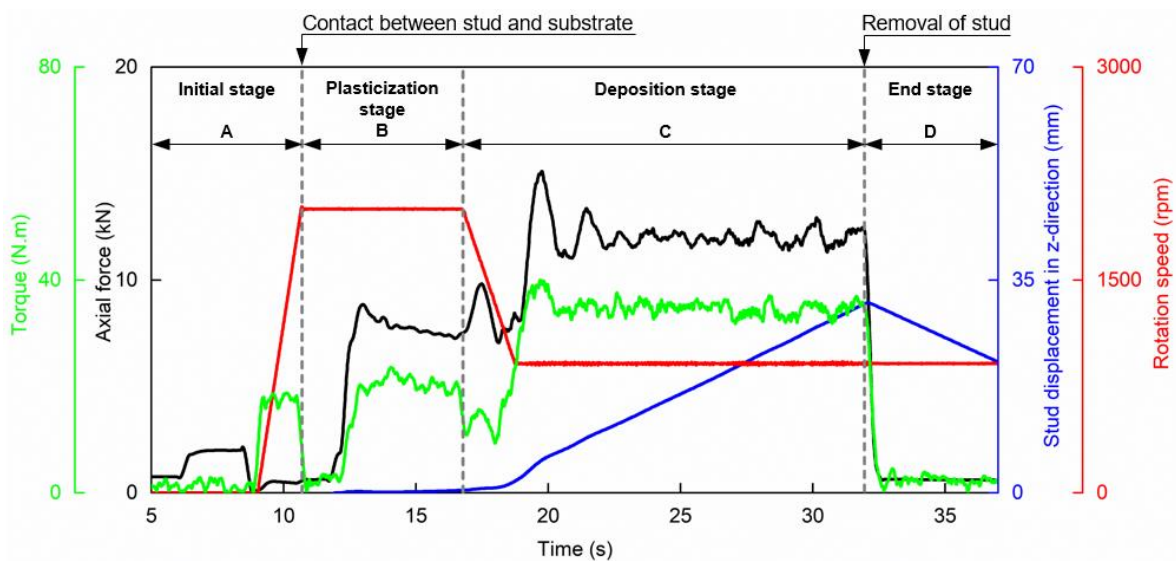
5 RESULTS AND DISCUSSION

This section gives the detailed results obtained from the early investigation stages over the suitable process parameter selection, including process analysis, microstructure analysis and mechanical testing. Further study of the fatigue crack growth in friction surfaced specimens are also discussed, with emphasis to fatigue life, crack growth rate in function of ΔK and fracture surface analysis.

5.1 PROCESS ANALYSIS

Figure 40 shows an example of a FS deposition process, with the monitoring of axial force (black), rotational speed (red), stud displacement in z-direction (blue) and torque (green).

Figure 40 – Process plot of a layer deposition of AA2024 over AA7475 alloys. Parameters are $F_z = 12$ kN, $v_x = 8$ mm/s and $R_s = 900$ rpm.



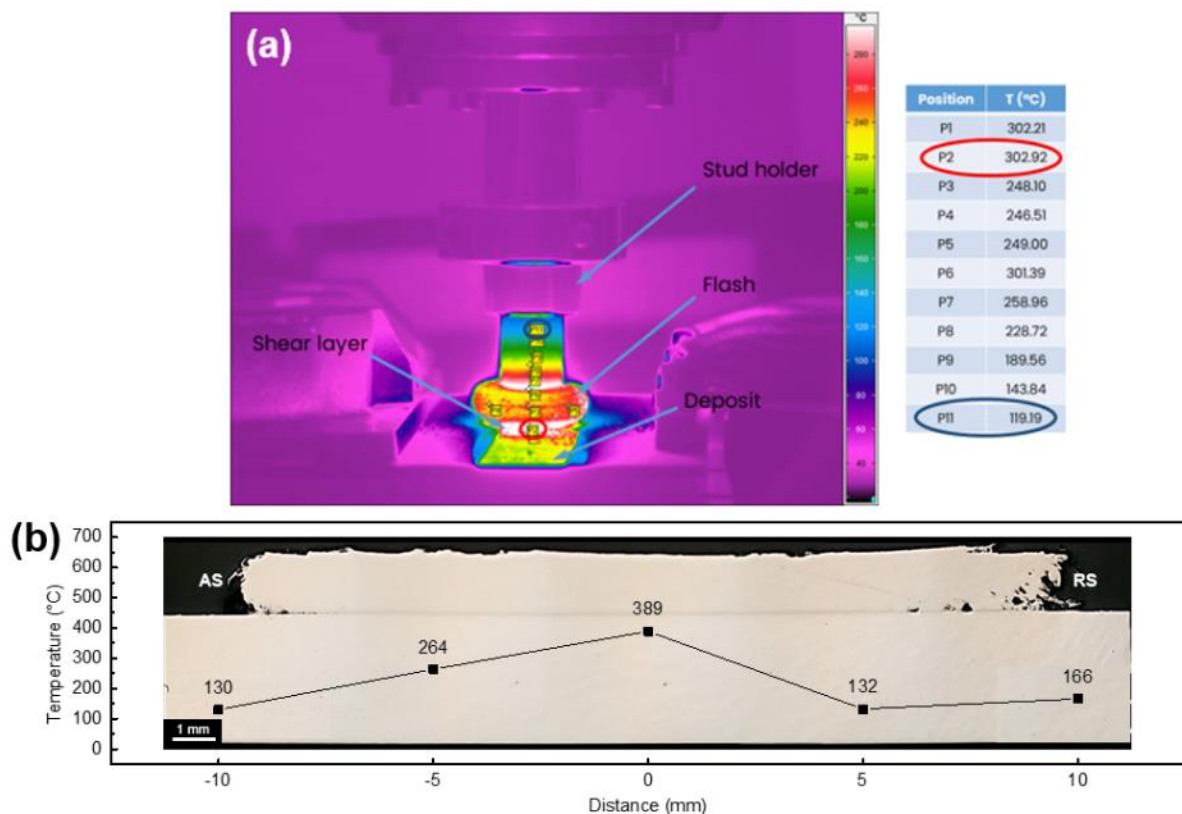
Source: the author.

In the initial stage (A), the stud is placed above the substrate and R_s is applied, as can be seen with the increase of R_s to 2000 rpm and torque curves. The rotating stud is pressed with a defined $F_z = 8$ kN over the substrate, and the plasticization stage (B) takes place. Different parameter set is used to induce higher heating rates and reduce instabilities caused by stud buckling or inefficient plastic deformation in the stud tip. In this stage, heat is generated by friction and the thermally softened material from the stud tip undergoes plastic deformation (mainly shear). In the next stage (C), a translational movement is applied and is defined as the deposition stage. A gradual increase of axial force from 8 to 12 kN can be observed from 17 to 20 s, as well as the

increase in stud displacement in z-direction and the Rs decrease to 900 rpm. A force peak of around 15 kN is observed when occurs the transition between the plasticization stage and deposition stage. This instability in the beginning of the deposition stage is due to the machine response to stud deflection. Torque and F_z show behave similar due to the machine force-control mode. FS process graphs for all parameters investigated are provided in appendix A.

The FS process temperature achieved is above recrystallization and below melting point temperature of the material. (66,67) To check the temperature achieved in the deposition of AA2024 onto AA7475, measurements were performed with IR-camera (Figure 41a) and thermocouples (Figure 41b).

Figure 41 – FS process temperature measures. (a) Vertical temperature distribution via IR-camera. (b) Horizontal temperature distribution via embedded thermocouples into the substrate sheet.



Source: the author.

The maximum temperature measured from IR-camera is located at the outer shear layer between the stud tip and the deposit surface, with 302.92 °C. The minimum temperature recorded of 119.19 °C was obtained directly at the junction of stud holder and stud. On the other hand, the maximum temperature measured with thermocouples was 388.7 °C, close to the center of the deposition path.

Pirhayati et al. (2020) found, using experimental and numerical simulation methods, a gradient of temperature and plastic deformation rate along the deposit-substrate thickness when depositing AA2024 on AA2024 using similar process parameters as investigated here. The authors showed that the maximum temperature at the center of the top of the deposit was ~ 342 °C, while the temperature at the substrate-deposit interface reached only ~ 235 °C. (68)

Possible errors during IR measurements occurs due to distance to measuring area and reflection from surrounding surfaces, justifying the difference between the two measuring methods. Also, the decrease from 166.1 °C to 131.9 °C between thermocouples n. 2 and 3 is related to a poor embedding of one of the thermocouples into the substrate sheet.

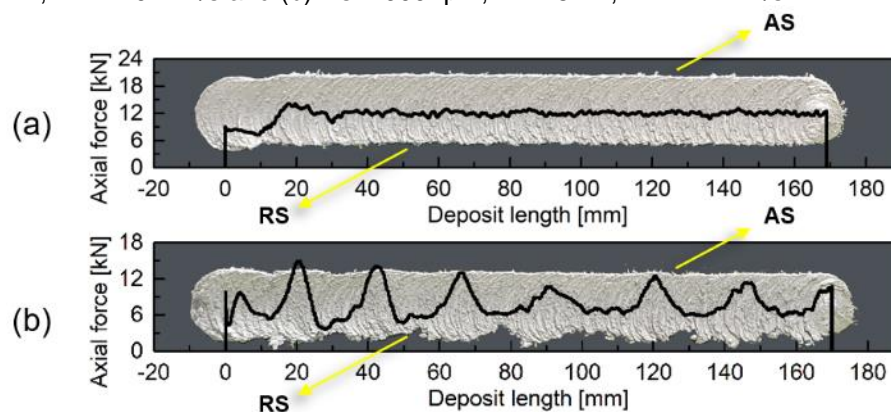
5.2 PROCESS PARAMETER ANALYSIS

5.2.1 Deposit surface morphology

A main process parameter window for axial force, rotational speed and deposition speed has been developed through knowledge-based orientation trials and with DoE (one-factor-at-a-time) method. The initial FS parameter selection criteria for further process development have been the process stability and visual appearance of the deposits.

For a better understanding, Figure 42 shows a comparison between two specimens regarding process stability, and both were analyzed by superposition of axial force over the deposit surface appearance.

Figure 42 – Axial force plot and visual appearance. Process parameters are (a) RS = 900 rpm, Fz = 12 kN, vx = 10 mm/s and (b) Rs = 900 rpm, Fz = 8 kN, vx = 12 mm/s.

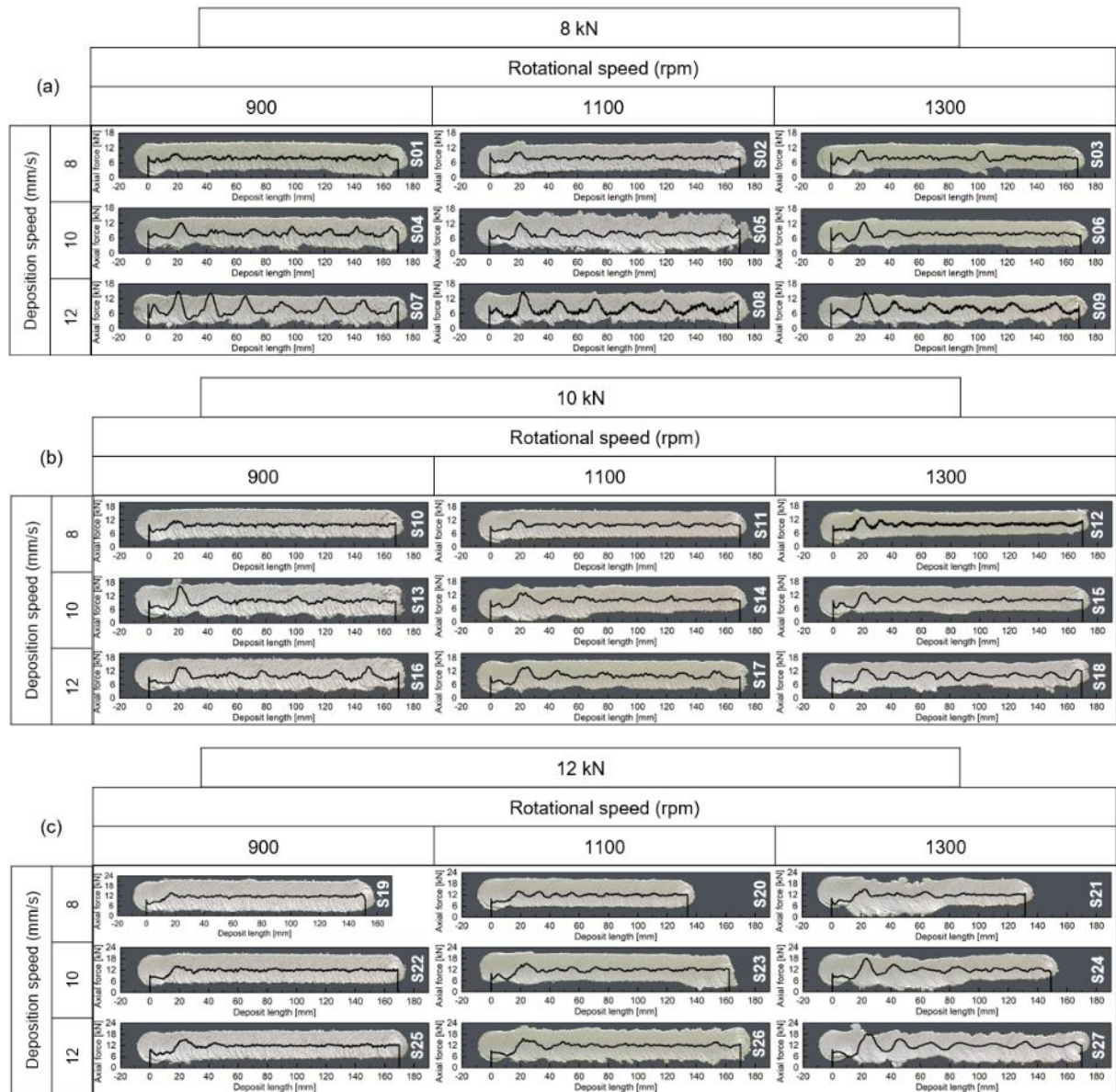


Source: the author.

When the recorded axial force is close to constant, it consequently contributes to a homogeneous deposit surface appearance, as seen in Figure 42a. A continuous deposit width provides a better experimental planning, such as correcting the offset between stud center and deposit center and consequently the best results from mechanical behavior. The oscillations observed in the axial force given by high and low force peaks shown in Figure 42b, produces heterogeneous deposit surface morphology, i.e., with deposit width variation along deposit length. This heterogeneity is attributed to low material plasticization from the stud, mainly caused by insufficient heat input. (69,69)

The deposit surface morphology among all deposited AA2024 on the AA7475 substrate, with respective superposed axial force on them from the process parameter window (27 specimens), is shown in Figure 43.

Figure 43 – Deposit surface morphology and superposed axial force over the 27 specimens. (a) Constant $F_z = 8$ kN, $R_s = 900, 1100$ and 1300 rpm, $v_x = 8, 10, 12$ mm/s. (b) Constant $F_z = 10$ kN, $R_s = 900, 1100, 1300$ rpm, $v_x = 8, 10, 12$ mm/s. (c) Constant $F_z = 12$ kN, $R_s = 900, 1100, 1300$ rpm, $v_x = 8, 10, 12$ mm/s.



Source: the author.

The first process parameter window (Figure 43a), with constant $F_z = 8$ kN is possible to notice that majority of parameter sets presented heterogeneous surface appearance, with axial force oscillations, except for parameter sets between 900 and 1100 rpm at 8 m/s. The same behavior took place for moderate F_z of 10 kN (Figure 43b). However, with axial force of 12 kN being constant, the best parameter sets that produced homogeneous deposit surface was at the 900 rpm along with the variation of deposition speed among 8, 10 and 12 m/s, as be seen in Figure 43c.

Furthermore, the increase of F_z to 12 kN-combined with the lowest v_x of 8 mm/s generated deposits below 170 mm length. This is due to the increase in stud consumption rate. This trend is also observed for constant $v_x = 10$ mm/s and variation of R_s from 900 to 1300 rpm. One interesting observation can be discussed on specimens with constant $R_s = 1300$ and variation in v_x : the increase in v_x from 8 to 12 mm/s resulted in gradual deposit length increase from ~130 mm to successful 170 mm. As cited earlier, the axial force influences the stud consumption rate. In this case, the increase in v_x tends to solve the deposit length problem, although the surface appearance is still unsatisfactory.

According to the first selection criteria described in section 4.2.2, the suitable process parameters, regarding surface appearance and process stability, are as follow in Table 6. The next selection criteria will be discussed in the following section.

Table 6 – Suitable process parameter selection regarding surface appearance and process stability.

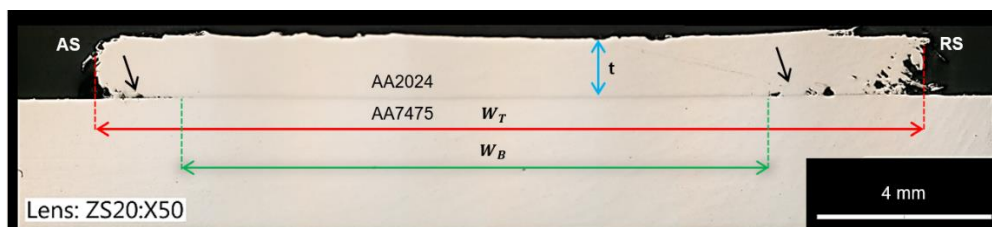
Specimen n.	S01	S02	S03	S06	S10	S11	S19	S20	S22
F_z [kN]	8	8	8	8	10	10	12	12	12
R_s [rpm]	900	1100	1300	1300	900	1100	900	1100	900
v_x [mm/s]	8	8	8	10	8	8	8	8	10

Source: the author.

5.2.2 Deposit geometry

The next step from this work concerns to obtain the measurement of the deposit geometry, i.e., effective width (W_B) from cross-section macrographs. Macrographs from all parameter sets investigated are provided in Appendix B.

Figure 44 – Cross-section macrograph from specimen S09. Parameters are $F_z = 12$ kN, $v_x = 8$ mm/s and $R_s = 900$ rpm.



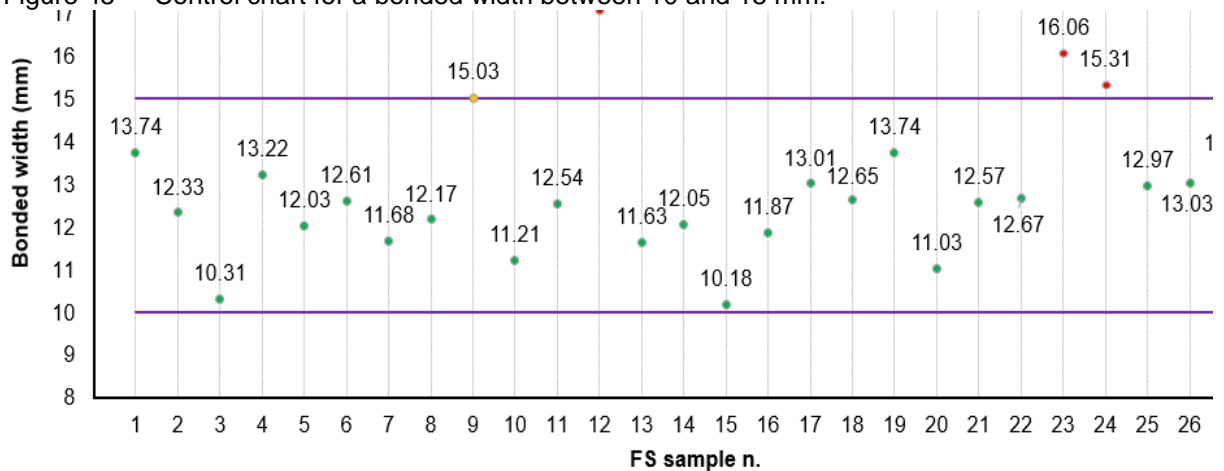
Source: the author.

Figure 44 illustrates an example from a specific specimen. It is clear to notice that deposit edges characteristics differ from the advancing side (AS) to the retreating side (RS) and it's a well-known intrinsic feature of the FS process. It was observed in

all parameter sets investigated in the scope of this work, the left edge has a smoother appearance, and the right edge has a rougher appearance. Also, all specimens present a sound bonding and visual defect-free interface between the deposit and the substrate were revealed. However, lack of bonding occurs at the deposit edges, due to inefficient axial force application and material adherence from the rotating stud in this region.

According to section 4.2.2, an effective W_B between 10 and 15 mm must be achieved. It can be noticed from the control chart (Figure 45) that the majority achieved a satisfactory bonded width, excepting specimens S09, S12, S23 and S24, which presented $W_B > 15$ mm and were already excluded in the previous section.

Figure 45 – Control chart for a bonded width between 10 and 15 mm.



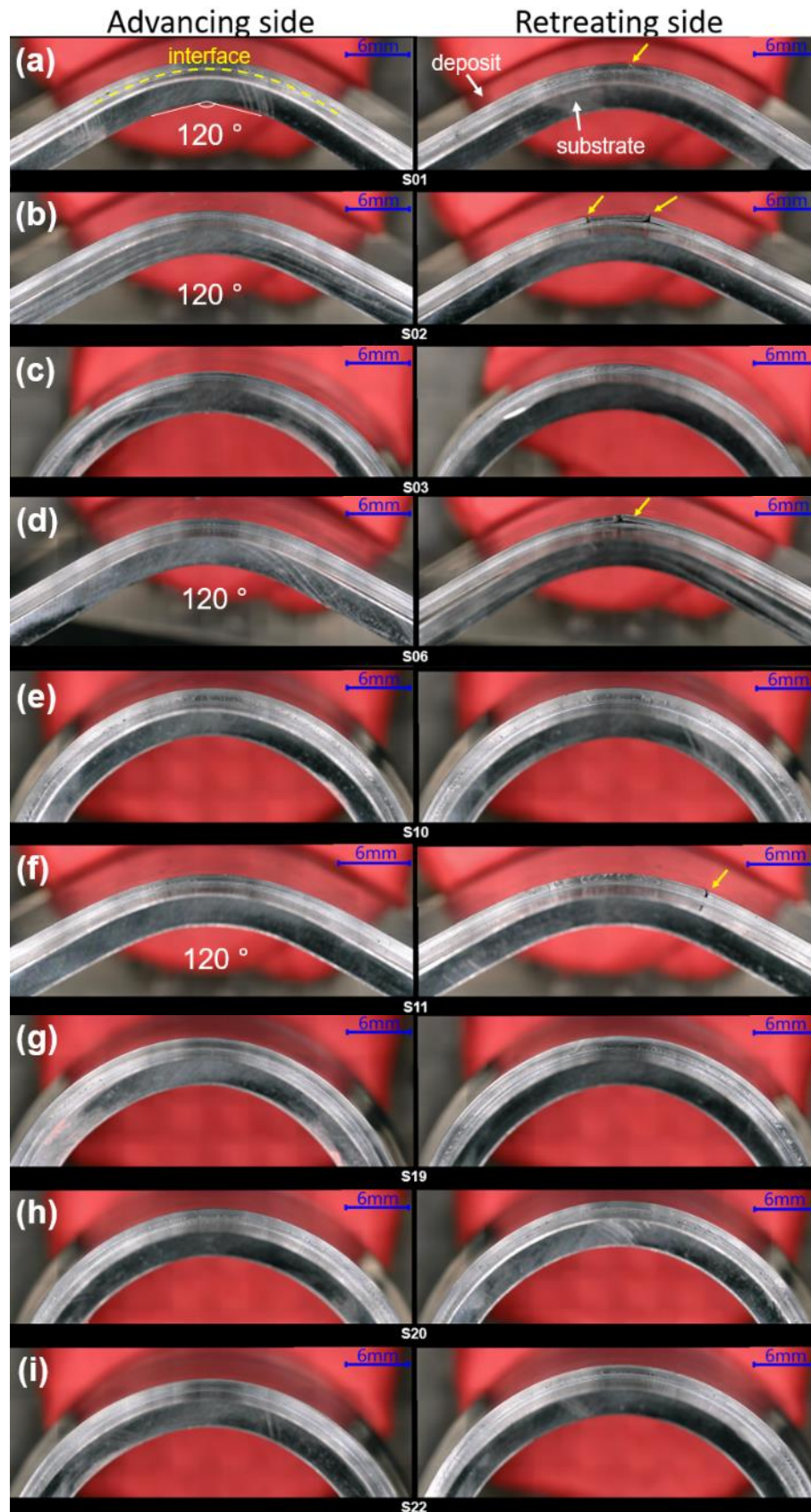
Source: the author.

5.2.3 Effective interface adhesion

To qualitatively evaluate the interface bond strength, three-point bending tests were performed on specimens from Table 6. Figure 46 highlight the lateral surface features from bent specimens.

Some specimens presented defects, indicated by yellow arrows (e.g., delamination, layer detachment, peeling) at 120° bend angle, such as (a), (b), (d) and (f). This is attributed mainly to a lower bonded edge resistance achieved from the respective process parameters, the reason why defects were observed in smaller bending angles. Only small crack initiation in RS is visible in the bonding interface from specimens bent until 180°, as can be seen from (c), (e), (g), (h) and (i). However, a quantitative comparison between each condition is not feasible due to different specimen geometries.

Figure 46 – Lateral surface of different FS specimens after three-point bending tests.



Source: the author.

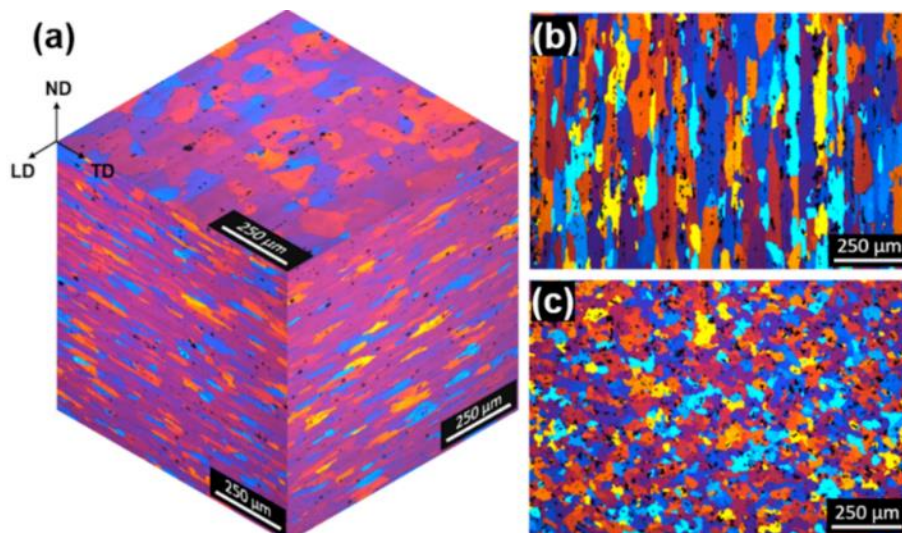
5.3 SUITABLE PROCESS PARAMETER

Regarding the selection criteria described in section 4.2.2, the parameter set chosen for further investigation of this work was specimen S19 ($F_z = 12$ kN, $R_s = 900$ rpm and $v_x = 8$ mm/s). Even though most specimens suit the selecting criteria, the reason S19 was chosen is due to the wider effective bonding width achieved, compared to other parameters selected for three-point bending test.

5.4 MICROSTRUCTURE ANALYSIS

To identify microstructure changes or volumetric defects, Figure 47 and 48 shows the microstructure from AA2024-T351 (stud) and AA7475-T761 (sheet) before and after FS layer deposition.

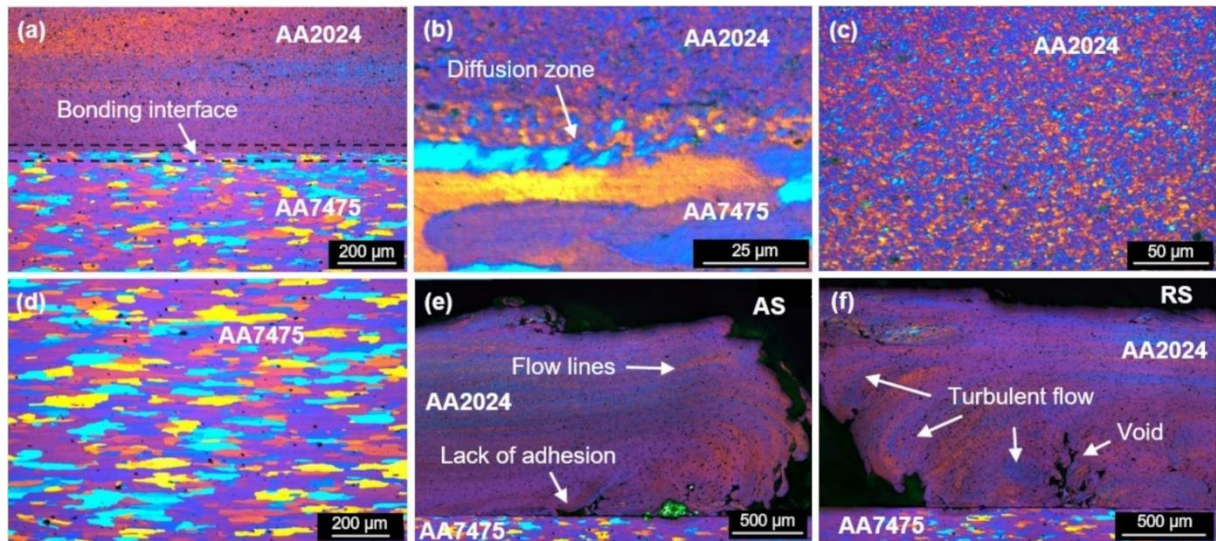
Figure 47 – Microstructure from BM. (a) three-rolling direction AA7475-T761 sheet, (b) elongated grains in extrusion direction and (c) equiaxed grains in cross-section area of AA2024-T351 stud.



Source: the author.

Figure 46a shows the AA7475-T761 grain morphologies from three-rolling direction characteristics: transverse direction (TD), normal direction (ND), and rolling direction (LD). The AA2024-T351 studs exhibit elongated grains in the extrusion direction and equiaxed grains in the cross-section area, as shown in Figure 46b-c.

Figure 48 – Micrographs from the microstructure of the deposit. Process parameters are FZ = 12 kN, $v_x = 8$ mm/s and RS = 900 rpm. (a-b) Bonding interface; (c) refined deposit microstructure; (d) substrate microstructure; edges from (e) AS and (f) RS.



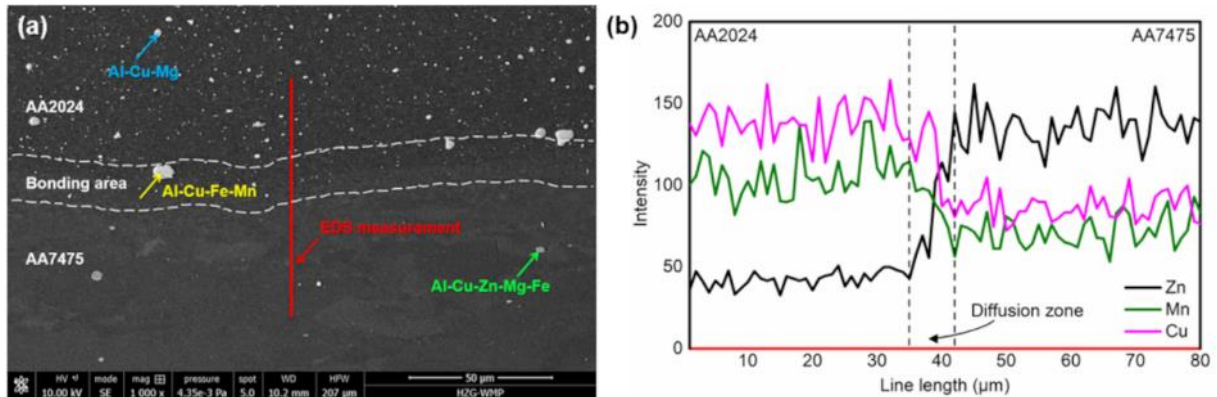
Source: the author.

Figure 48 shows the microstructural features from dissimilar deposition by the FS process. Similar features were observed in all parameters investigated in the scope of this work. Figure 48a shows a defect-free bonding interface achieved with no macroscopic volumetric defects. A diffusion zone is observed in Figure 48b, from fine-grained deposit material across the interface towards the elongated grains from the substrate material. In FS of most of aluminum alloys, strong metallurgical bond is accomplished in the joining of deposit and substrate material. (70) Fine and homogeneous microstructure achieved from dynamic recrystallization is often observed within the deposit material, as reported in several works (69-72), mainly due to plastic flow at high strain rates. Figure 48c shows the fine-grained microstructure from the deposited material (AA2024). The thermomechanical process suffered in the deposited material leads to an equiaxial and refined microstructure. The substrate microstructure, shown in Figure 48d, exhibit a similar microstructure from the as-received material. During FS process, the substrate does not suffer any plastic deformation like the deposited material. Although, it is affected by the thermal cycle from the process, influencing the precipitation state, for example. Both edges of the AS and RS regions from the deposit material (Figure 48e-f, respectively) reveal some features, such as flow lines, turbulent flow and voids. These features are consequences of the material flow during the deposition process, i.e., the material flow of the rotating plane at the surface of the deposit is influenced by the rotation of the stud in a way that the stud tip is sheared off in a softened state. (73) Since this region

is absent of lateral restraints, the material flow at the edges produces some features, as well as vortex-like appearances together with microdefects. (66,74)

A detailed investigation into the diffusion zone shown in Figure 48b is done through SEM and chemical analysis by EDS (Figure 49).

Figure 49 – SEM micrograph from the bonded interface (a). EDS analysis from bonded interface region between AA2024 deposit and AA7475 substrate (b).



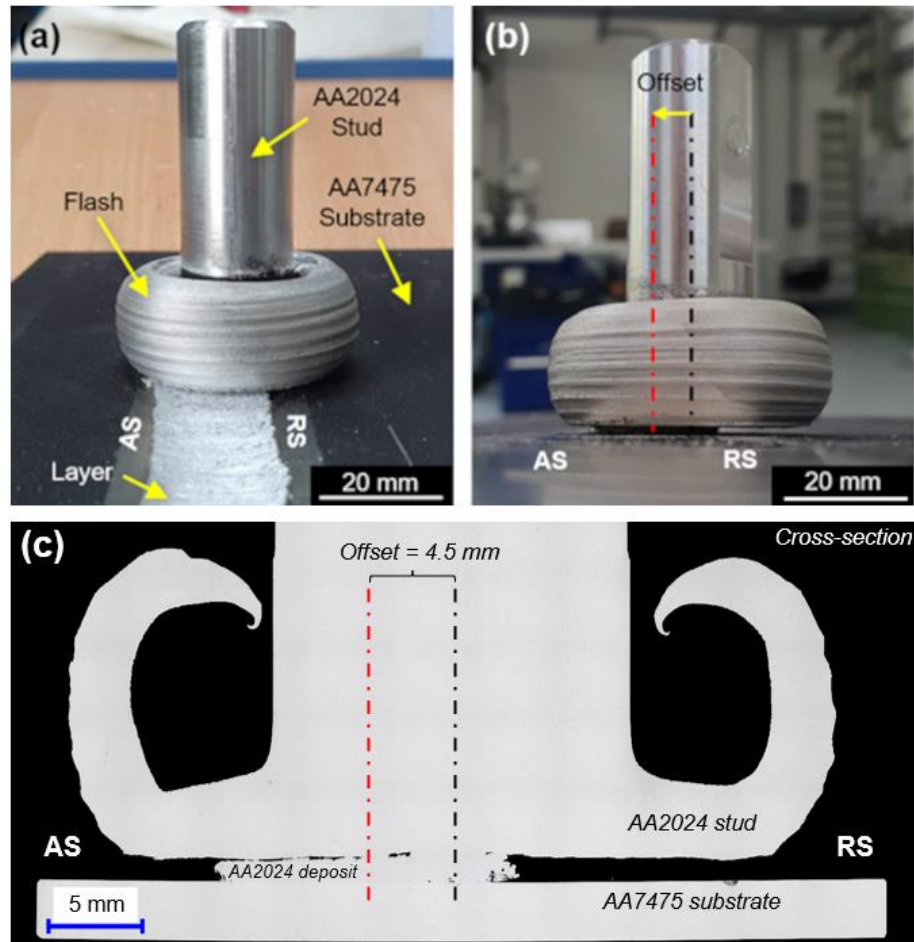
Source: the author.

Intermetallic particles (IM) with compositions of Al_2CuMg (S' and S phases) and $\text{Al}(\text{Cu}, \text{Fe}, \text{Mn})$ are present in the deposit microstructure (Figure 49a). During FS, IM particles do not completely dissolve, larger particles are mainly found near the interface and small particles are finely dispersed within the deposit material.

From EDS analysis, diffusion is detected along a thickness of $7.5 \mu\text{m}$ with Cu, Mn and Zn alloying elements varying across the bonded interface (Figure 49b). This similar behavior was observed in the deposition of AA6082 over AA2024. (74)

During deposition by FS, part of the softened material from the stud is squeezed out of the contact plane, mainly by the axial force applied, forming a flash around the stud (Figure 50a). (58) Another characteristic observed during the deposition of AA2024 on AA7475 was a 4.5 mm offset between the center of the stud and the center of the deposit, as the example shown in Figure 50b-c. This offset towards AS occurs due to the combination effect of process parameters (66,72), e.g., the axial pressure and thermal field submitted on the layer deposition. According to Pirhayati and Aval (2019) this deviation can be associated to higher process temperatures on the AS than on the RS, due to the stud rotation and deposition speed acting in the same direction during FS. (75)

Figure 50 – FS offset. (a) and (b) showing the stud position on the substrate, and (c) the cross-section macrograph with a 4.5 mm offset.



Source: the author.

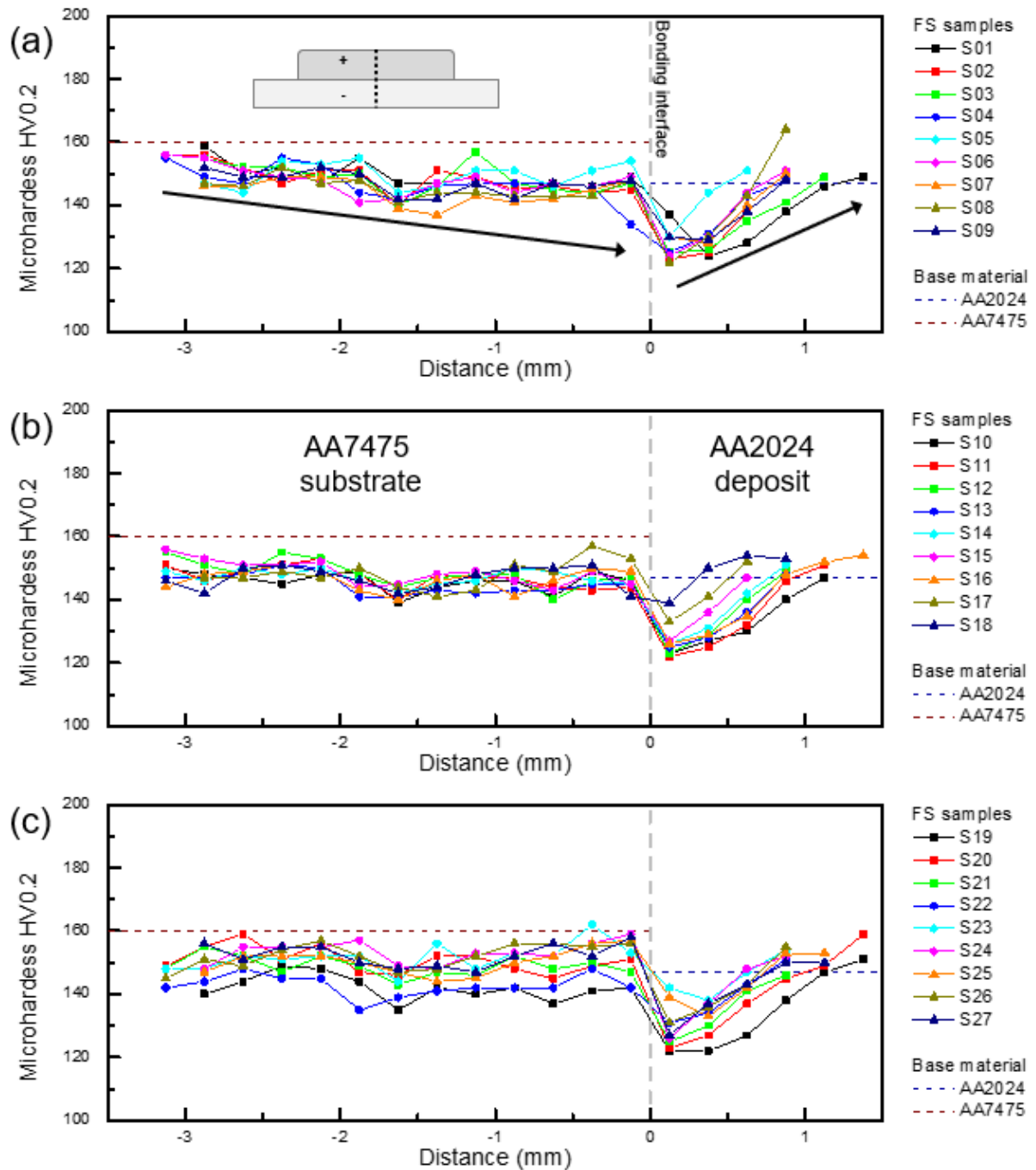
5.5 MECHANICAL TESTING

This section gives a selection of results obtained from microhardness testing and tensile testing of FS specimens, in order to examine the HAZ extension, process influence on mechanical properties and fracture surface investigation.

5.5.1 Microhardness test

Figure 51 shows the microhardness profile obtained for all FS parameters investigated in this study.

Figure 51 – Microhardness profile of FS specimens and BM, with constant (a) $R_s = 900$ rpm, (b) $R_s = 1100$ rpm and (c) $R_s = 1300$ rpm.



Source: the author.

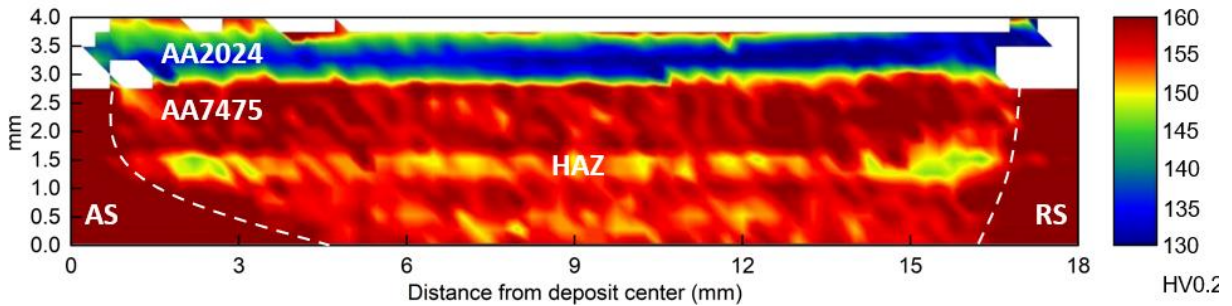
The BM is shown as base line (dashed line) for comparison with the material measured after FS layer deposition. A uniform distribution of hardness values within the AA7475 substrate can be noted, independent of the specific process parameter set. Only a small scatter in hardness values at the substrate after the process at high axial force (12 kN) and low deposition speed (8 mm/s), Fig. 51c, is detected. Concerning the AA2024 deposit, the hardness profiles through the coating thickness

shows the same trends for all parameter sets, i.e., a lower hardness near the substrate-deposit interface (~ 120 HV0.2) and a gradual increase of hardness across the thickness until the highest value of ~ 147 HV0.2 is reached near the deposit surface.

As the FS process induces thermo-mechanical phenomena in AA2024 consumable material, i.e., thermal cycle and different plastic deformation rates through deposit thickness, it is expected that both strengthening mechanisms, precipitation hardening and grain refinement, can likely influence the strength of the deposited material. According to a study, the dissolution of GPB zones and the S' phase and the formation of the S phase of the AA2024 alloy were observed to take place at the peak temperatures of 225 and 260 °C, respectively. (77) Yet, the dissolution of the S phase occurs in the range of 330 up to 470 °C. (78) Furthermore, along the deposit thickness, the deposited material is cooled by convection into the environment as well as heat conduction into the substrate and, since the FS process has a short deposition time, this results in short thermal cycles. This way, the difference of hardness seen in Figure 50 along deposit thickness can be related to the dissolution of GPB zones and S' phase, as well as coarsened S phase, as a result of the temperature reached during FS.(77)⁷⁶ The highest temperature (~ 342 °C) concentrated near the top of the AA2024 deposit surface might likely contribute to the dissolution of the S phase. However, due to the short thermal cycle, the prior re-precipitation of S' and S phases which took place all along the lower temperature range, will likely still be dominant, thus producing higher microhardness values. (77,78) Furthermore, a study also reported differences in hardness from the top of the deposit to the bonding interface, when depositing AA2024 over AA1050, with similar process parameters as in this study. (79) They showed that within R_s of 1000 rpm, precipitation hardening is considered as the predominant strengthening mechanism, whereas, at R_s of 600 rpm, i.e., lower heat generation, grain refinement is the predominant strengthening mechanism. In the current study, R_s of 900, 1100 and 1300 rpm were applied. Therefore, the difference in hardness along the AA2024 deposit thickness is most likely associated with temperature gradient that induces the dissolution of (GPB zone and S' phase) precipitates and coarsened S phase near the deposit-substrate, followed by re-precipitation of (S' and S phases) and some dissolution of S phase, in regions near the deposit surface. Moreover, the hardness of ~ 147 HV0.2 reached near the deposit surface is equivalent to AA2024 BM. This equivalent hardness is likely the result of precipitation hardening. (79)

Furthermore, the FS process induced a loss in hardness of ~18% compared to the as-received substrate. This softening likely occurs due to thermal cycle induced by FS, generating a HAZ in the substrate material. The HAZ extension is observed in the microhardness map shown in Figure 52.

Figure 52 – Microhardness map from cross-section of specimen with $F_z = 12$ kN and $v_x = 12$ mm/s, showing an asymmetrical HAZ.



Source: the author.

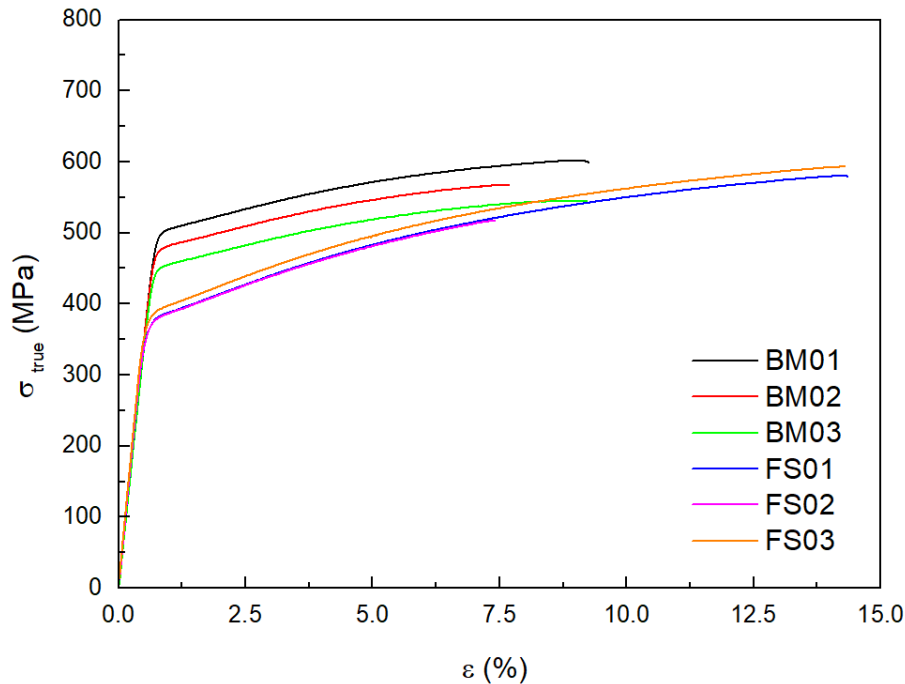
Thermal exposure generates variation in the extent of coarsening of the existing strengthening precipitates, decreasing mechanical strength. (80) The HAZ is also referred to as the lowest hardness zone due to a significant dissolution and coarsening of precipitates in aluminum alloys. (81) Larger HAZ towards RS is observed and is likely related to the process asymmetry, as seen from the offset shown in Figure 45. The middle of the stud contact plane is shifted to RS, increasing heat exposure in this region, compared to AS, and consequently affecting the strength in this region.

5.5.2 Tensile test

The tensile tests were conducted with the suitable chosen parameter (S19 with $F_z = 12$ kN, $R_s = 900$ rpm, $v_x = 8$ mm/s) and compared with AA7475-T761 BM.

Figure 53 shows the true stress/ true strain curves for tensile testing. Table 7 shows mean values of tensile properties from ultimate tensile strength (UTS), yield strength (YS) and elongation of the FS specimens reinforced with AA2024 deposits and AA7475-T761 uncoated BM.

Figure 53 – Tensile test results for AA7475-T761 BM (BM01, BM02 and BM03) and FS specimens (FS01, FS02 and FS03).



Source: the author.

Table 7 – Mean values of tensile properties for YS, UTS and elongation from BM and FS specimens.

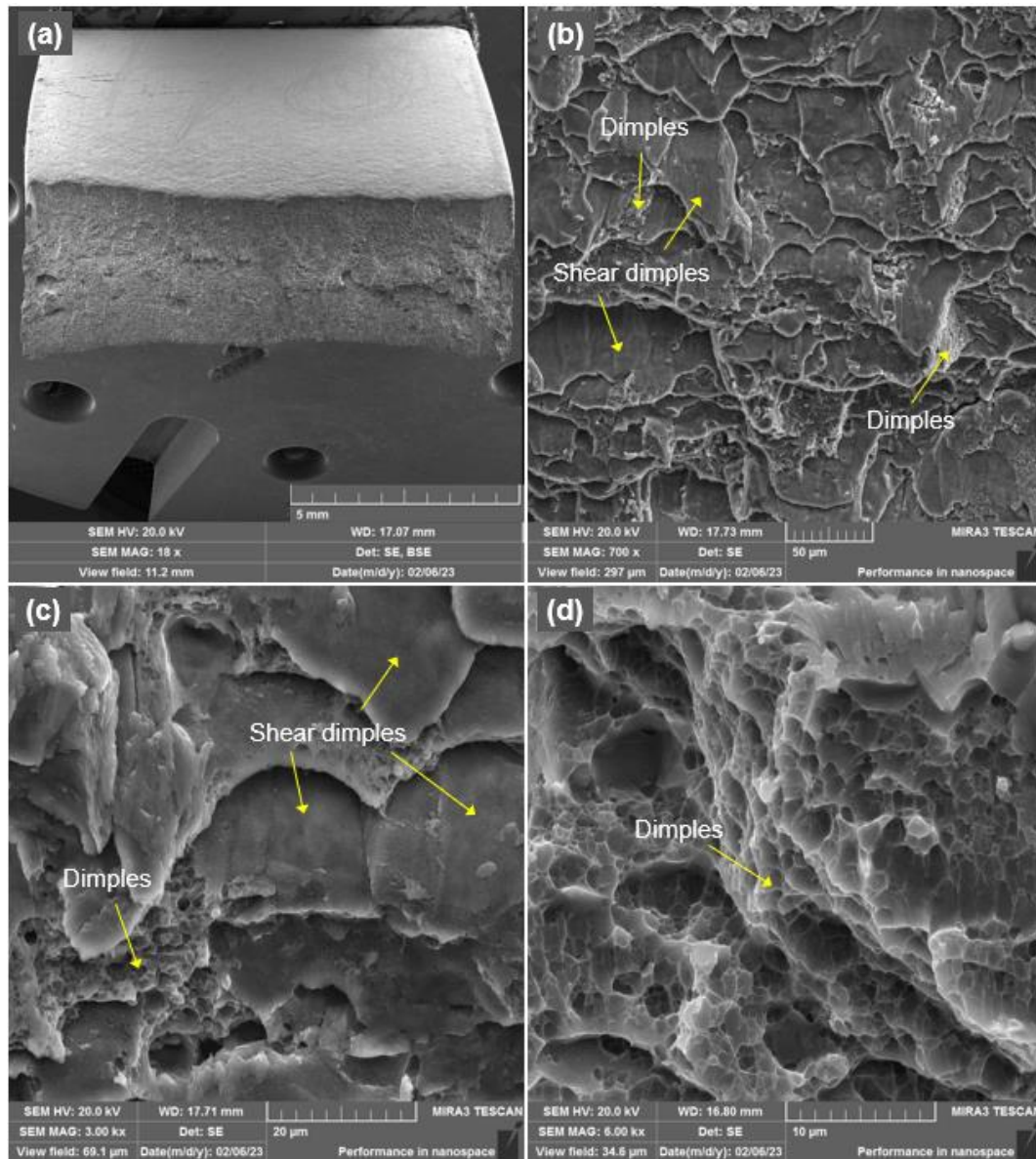
	BM	FS
YS (MPa)	478 ± 25	380 ± 7
UTS (MPa)	572 ± 29	564 ± 41
Elongation (%)	9.4 ± 1.2	12.9 ± 4.4

Source: the author.

The tensile behavior of the FS specimens differs from BM. Slight decrease of 1.4% in UTS and significant reduction of 25,8 % in YS from FS specimens is observed (Table 7), which can be related to process temperature exposure in the substrate material, as evidenced by microhardness results in the substrate material as shown in Figure 50. The reduction in YS and UTS can be likely associated to dissolution and coarsening of strengthening precipitates within the HAZ from the substrate material. Although, an increase of 37% in elongation suggests that the increase in ductility, in this regard, a positive contribution of the reinforcement provided from the AA2024 deposited layer. Similar result was achieved in the deposition of AA6082-T6 on AA2024-T3. (74)

Figure 54 and 55 depicts the fractured surface by SEM images from BM and the deposited material after tensile test, respectively.

Figure 54 – Fracture surface of AA7475-T761 BM specimen after tensile test (a). Fractured surface features (b), presence of shear dimples, tear ridges and smaller dimples (c) and magnification of the smaller dimples(d).

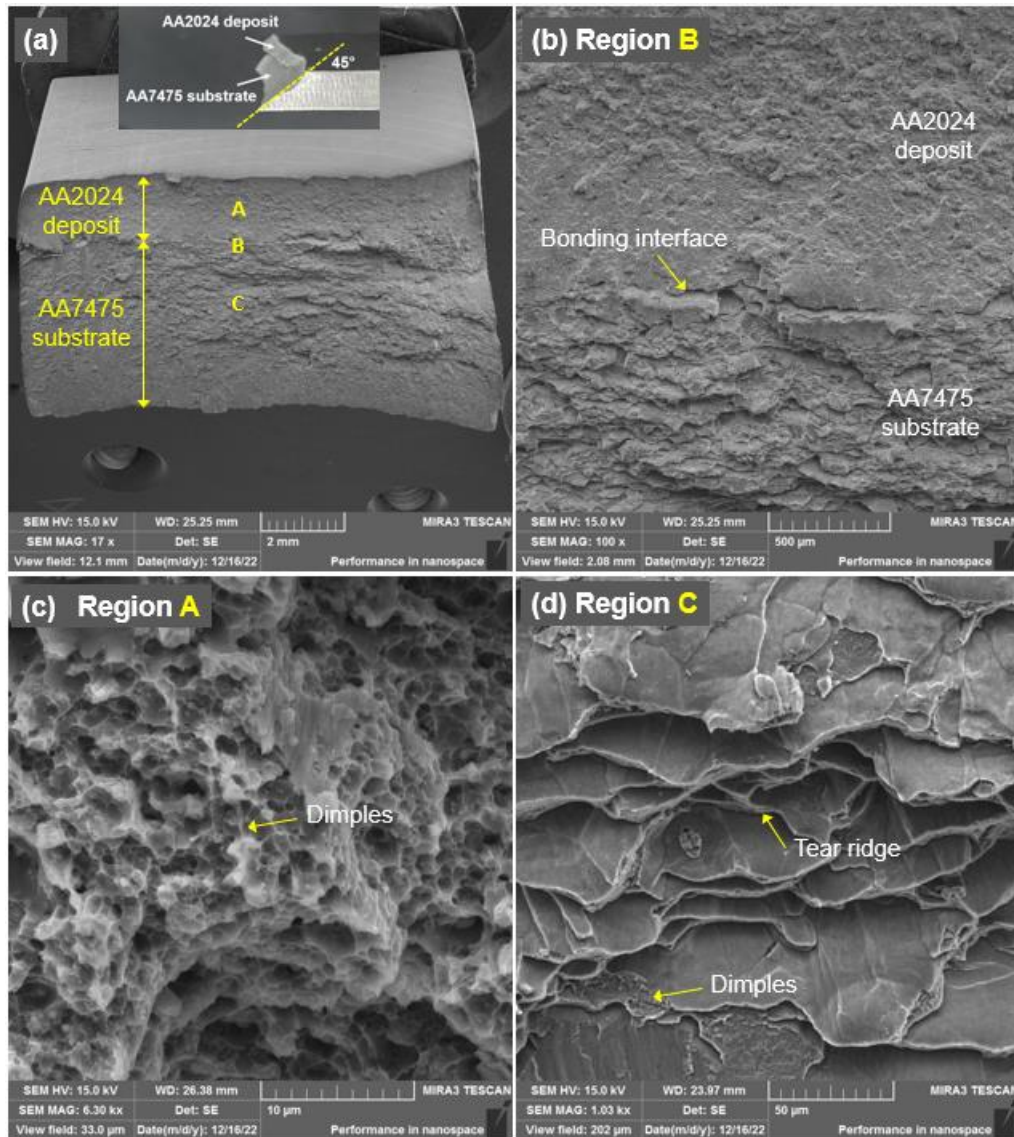


Source: the author.

Figure 54a shows a general observation on the fractured surface from AA7475-T761 BM, all specimens fractured along at 45° direction in relation to the applied load. According to the fracture morphology shown in Figure 54b-d, transgranular shear fracture is observed, with predominance of broad-flat surfaces. This feature is commonly associated to a ductile shearing mode. Similar fracture surface is found in a study of AA5052 alloy sheet after stretch flange forming, mainly generated by shear damage failure.(82) Few multi-sized cuplike depressions are also present in specific areas. This morphology, known as dimples, is typical of microvoid

coalescence that occurs by particle cracking, interfacial failure between an inclusion or precipitate particle and the surrounding matrix. (12,82-84)

Figure 55 – Fractured surface of FS specimen after tensile test (a). Bonding interface (b), AA2024 deposit material (c) and AA7475 substrate material (d).



Source: the author.

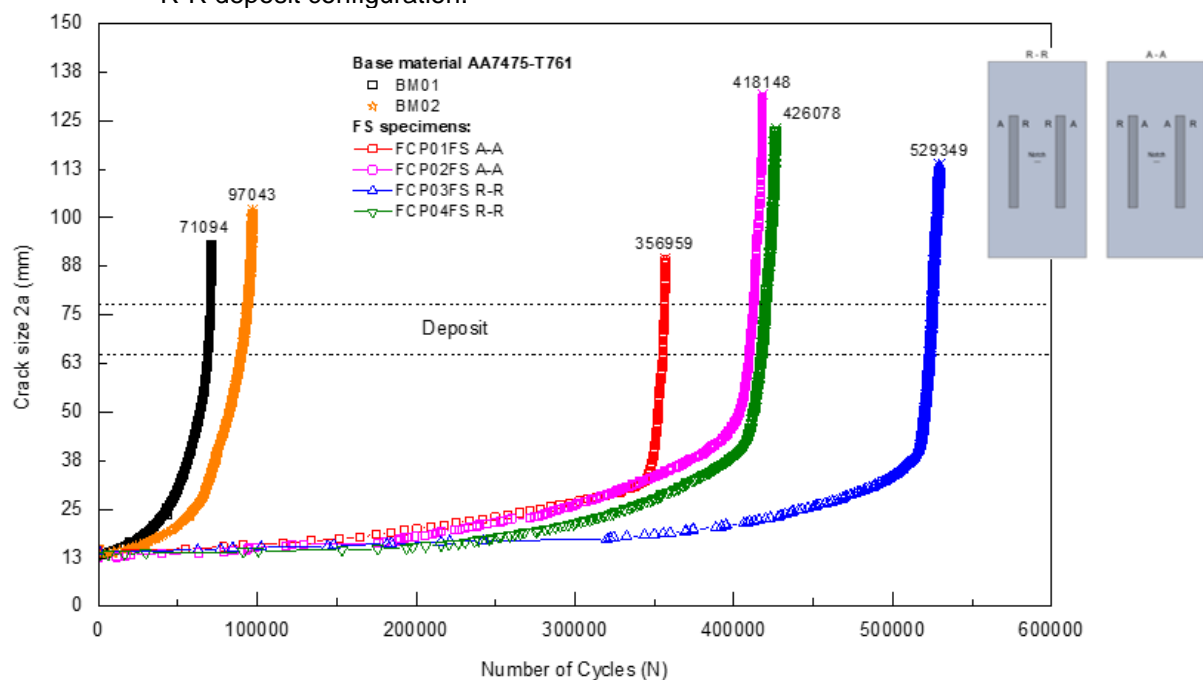
Figure 55a-b shows the fracture surface characteristics from deposit and substrate regions of a specific FS specimen. According to the fracture morphology shown in Figure 55c, the deposit material presents numerous small dimples. The fracture morphology shown in Figure 55d from substrate exhibits the similar broad-flat surfaces and less occurrence of isolated small dimples. This observation is similar to the fracture surface present in FSWelded AA7075-T6 alloy. (85)

5.6 FATIGUE CRACK PROPAGATION

As mentioned before, FS technique can result in a compressive stress field in the surrounding region from the active zone. This residual stress state achieved from FS has a potential application as fatigue crack growth retarder. This section presents the results and discussion from the FS layer deposition effect on the FCP and growth rate of AA7475-T761 sheets reinforced with AA2024-T351 deposits with three different configurations (i.e., R-R, A-A and R-A deposit configurations). Furthermore, fracture surfaces from low ΔK and moderate ΔK regions are analyzed, regarding the influence of the three configurations in comparison with uncoated AA7475-T761 sheets.

The evolution of the crack size as a function of the number of cycles for specimens with A-A and R-R configuration and uncoated AA7475-T761 BM is shown in Figure 56.

Figure 56 – Crack size versus number of cycles for AA7475-T761 BM and FS specimens with A-A and R-R deposit configuration.



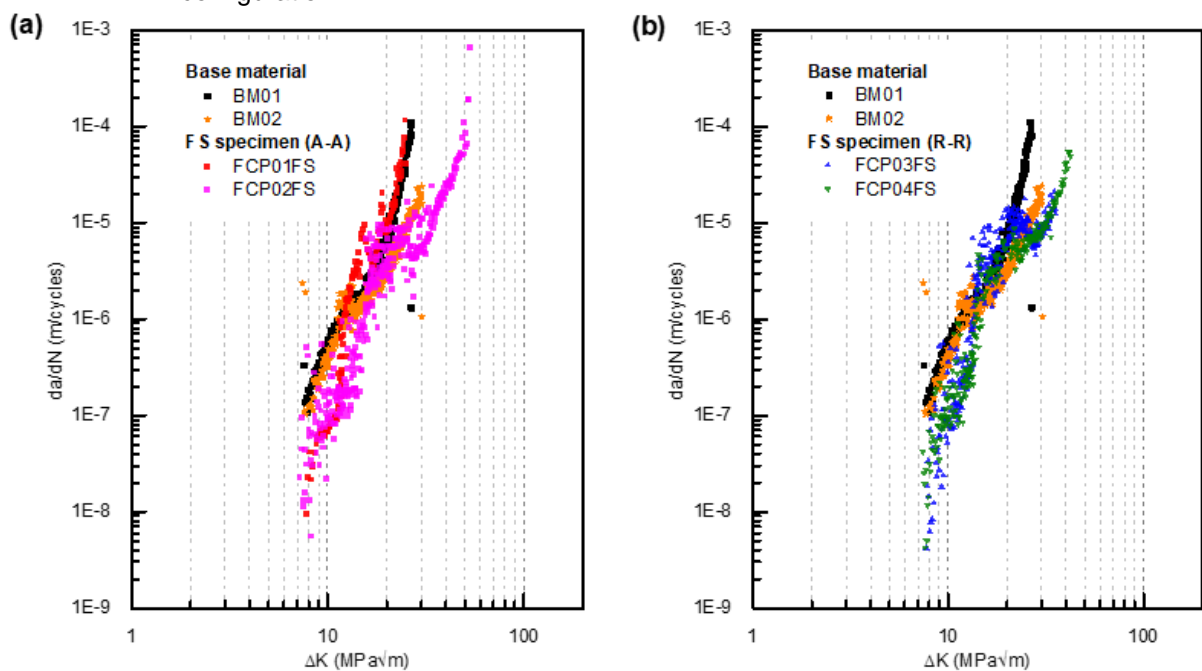
Source: the author.

The fatigue life for FS specimens with A-A and R-R deposit configuration was remarkably increased compared to the uncoated AA7475-T761 BM, with an expressive increase of around 460% and 568% in fatigue life, respectively. Also, the crack barely grows up to 150000 cycles for both FS specimen configuration, exhibiting interesting fatigue crack growth behavior, as the number of cycles required to pass through the compressive stress field assumed around the active zone is much greater than the

uncoated sheet. Many other techniques to improve fatigue performance were studied in aluminum alloys. The fatigue life achieved in AA7085 specimens reinforced with a pair of GLARE straps was improved in 90% compared to unreinforced specimens. (86) Laser shock peened panels from AA2024 alloy showed an increase in fatigue life of 38% with an 20mm offset from the center of the notch and the LSP region. (40) Yet, FS can also be carried out to improve fatigue life.

Figure 57 illustrates the results from FCGR (da/dN) as function of stress intensity factor (ΔK) for BM, A-A and R-R configurations. It can be observed that for both FS specimen configuration, FCGR is lower than BM specimens in low ΔK and near-threshold regions. To clearly demonstrate the crack retardation effect on the FCGR for both FS specimen configurations, the Paris constants, and the da/dN values at ΔK regions between 7.5 and 23 $MPa\sqrt{m}$ were determined in order to compare with BM specimens, as indicated in Table 8.

Figure 57 – Results for da/dN over ΔK for BM and FS specimens with (a) A-A configuration and (b) R-R configuration.



Source: the author.

Table 8 – Mean values of Paris constants and FCP rate from AA7475-T761 BM and FS specimens with A-A and R-R configuration.

Specimen	C ($\times 10^{-14}$)	n	da/dN=C(ΔK) ⁿ (m/cycle)($\times 10^{-5}$)								
			Low ΔK				Moderate ΔK		High ΔK		
			7.5*	9*	11*	13*	15*	17*	19*	21*	23*
BM	1.53	3.851	0.134	0.028	0.063	0.138	0.157	0.216	0.371	0.575	1.370
FS (A-A)	0.0351	5.495	0.002	0.010	0.009	0.088	0.202	0.427	0.781	0.670	2.154
FS (R-R)	0.0290	4.505	0.002	0.006	0.010	0.025	0.260	0.398	0.387	0.650	0.773

* ΔK =MPa \sqrt{m} .

Source: the author.

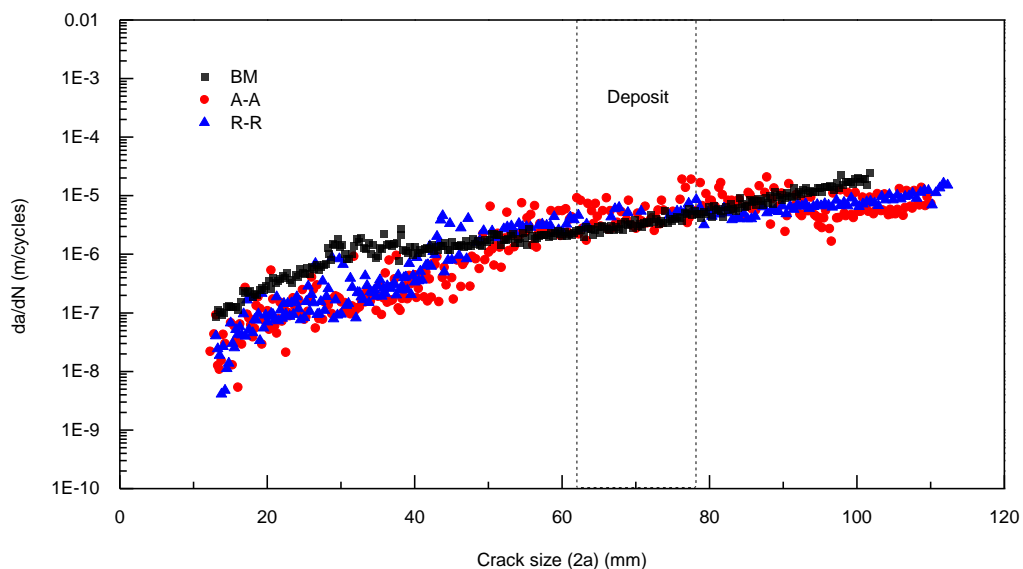
As can be seen in Table 8, the FCGR in low ΔK is reduced by 70% and 88% for A-A and R-R configurations, respectively. This reduction aligns with the observation made in Figure 57. The reduction in FCGR suggests the presence of compressive residual stresses, which contribute to slowing down crack growth, especially for crack lengths up to 40.00 mm, as shown in Figure 56. In the case of moderate ΔK , the FCGR for the BM specimen tends to be lower than for both FS deposit configurations. This indicates a reverse behavior, which is likely due to the presence of an active zone beneath the deposit region. This active zone experiences tensile residual stresses, which accelerate fatigue crack growth. Finally, at high ΔK , the specimen with the A-A configuration exhibits a higher FCGR compared to the other configurations. This can be attributed to a lesser contribution of the compressive residual stress field achieved when depositing the AS on the same side as the crack growth path.

Current investigation regarding residual stress state for FS layer deposition of 2XXX alloy on 7XXX alloy has not yet been published. In a study of FSW of AA7075 alloy, residual stress profiles present an active zone around the welded joint, more concentrated on the RS, due to differences in heating cycles and clamping arrangement. The center of the nugget zone is concentrated by tensile stresses and balanced by a compensative zone of compressive residual stresses in the surrounding material. (87) Another work on the joining of AA7075 plates by FSW shows slightly higher compressive stresses in RS, as compensation for the higher tensile stresses achieved in this region for this material. (88) The results obtained in a study regarding FS layer deposition of Ti-6Al-4V also shows an active zone of tensile residual stresses in the deposit region, and as consequence a compensative zone characterized by compressive residual stresses around the deposit region. (47) Thus, it is expected an increase in fatigue life due to the presence of residual stress induced by FS, mainly by

compressive stresses, that contributes to the reduction of crack growth rate. It was observed in shot peened FSWelded AA7075-T7351 alloy, where results of crack growth rate were converging at higher ΔK . (89) A study regarding FSW of AA7050-T7451 alloy indicates that the significant reduction in FCP rates of FSWelded specimens was mainly due to the contribution of residual stresses. (90) It is shown in several works that fatigue crack can be retarded by compressive residual stresses around the crack front path. (91,92) Research on AA6061-T6 with LSP surface treatment, known as a process that induces compressive residual stresses, indicates a decrease in FCP rates due to compressive residual stresses induced by the process. (93) The results show values of approximately 2×10^{-5} and 8×10^{-5} mm/cycles in crack growth rate for low ΔK . In another study on the effect of laser shock peening on FCP of AA2024-T3 alloy, fatigue crack growth for laser-peened specimen and BM is retarded by 23%, considering $\Delta K=8 \text{ MPa}\sqrt{\text{m}}$. (94)

Figure 58 shows the results for FCGR (da/dN) as function of crack size for BM, A-A and R-R specimen configuration.

Figure 58 – FCP rate (da/dN) versus crack length ($2a$) for AA7475-T761 BM, A-A and R-R FS specimen configuration.



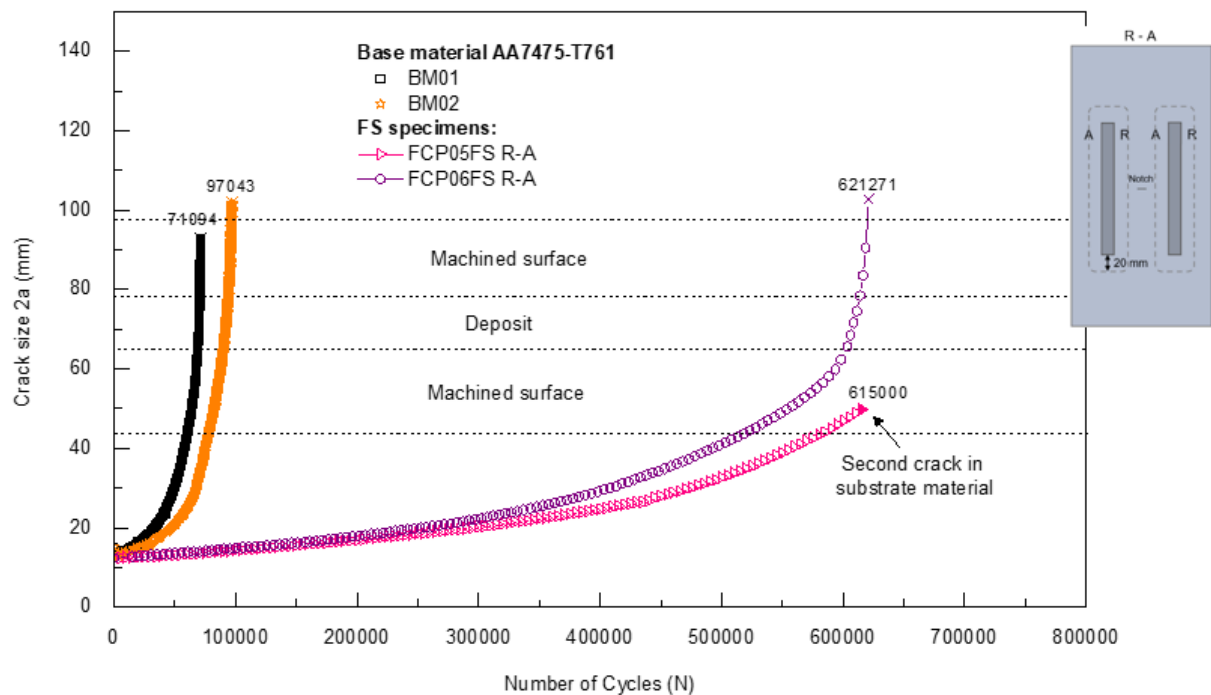
Source: the author.

From Figure 58, it can be noticed for both FS deposit configurations that the crack growth delay occurs up to 40.0 mm. Also, specimen with A-A configuration presents slightly higher da/dN for crack sizes above 40 mm, compared to others, which agrees with the da/dN values for moderate ΔK (Table 8). According to a study of residual stress state in the deposition of AA6082 on AA2024, slightly higher

compressive stresses are reached in RS. (47) Therefore, lower crack growth rate is expected in the RS, i.e., in the R-R deposit configuration.

Figure 59 shows the results from crack size as function of number of cycles for specimens from BM (AA7475-T761) and two FS specimens with R-A deposit configuration and machined sheet surface. An increase of around 739% in fatigue life is achieved for specimen FCP06FS. Machining is a process that can induce an active zone with a compressive nature and affect the crack growth rate. (94,95) A secondary crack nucleates and propagates on the substrate material in specimen FCP05FS. The machined surface can lead to stress concentration, thus favoring a secondary crack nucleation in the surface.

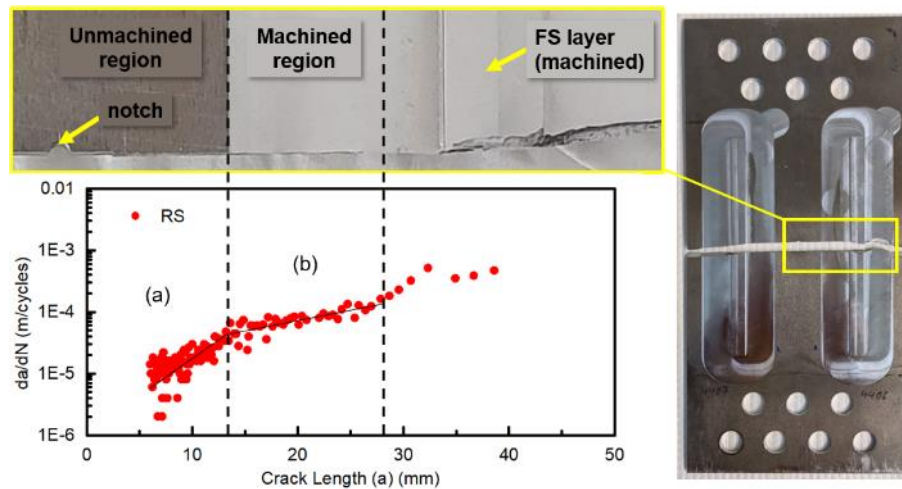
Figure 59 – Crack size (2a) versus number of cycles for BM (AA7475-T761) and FS specimens with R-A deposit configuration and machined surface.



Source: the author.

Figure 60 illustrates with more details an example of the crack growth rate within the machined region in RS for the same specimen. The machined region affects positively the crack growth restrain, as seen by the curve slope from the middle portion of the da/dN versus crack length curve.

Figure 60 – Crack growth rate da/dN over crack length on RS notch side for specimen FCP06FS. Different slope in (a) unmachined region and (b) machined region.

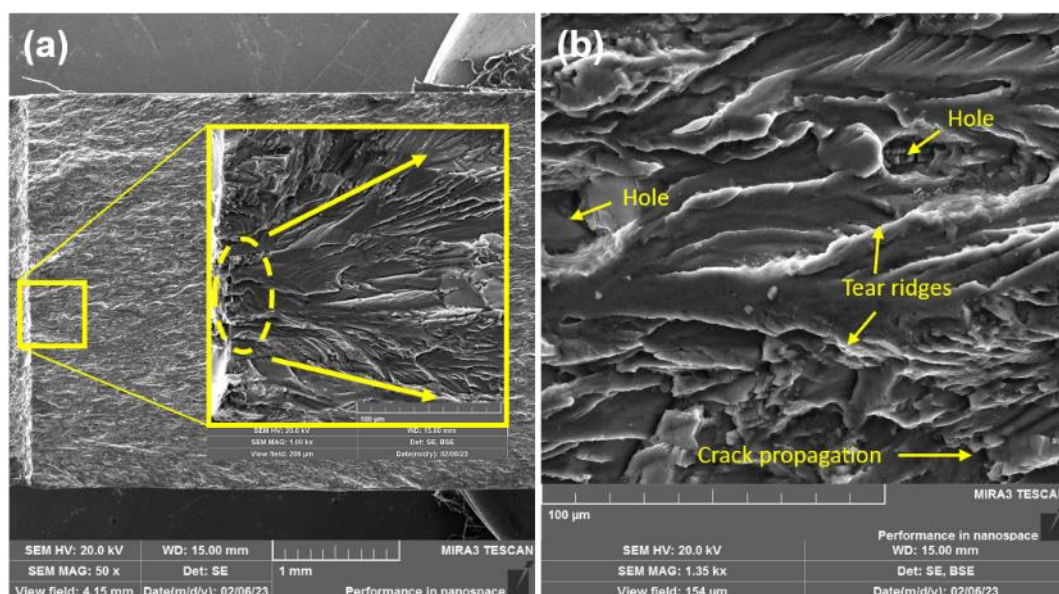


Source: the author.

5.6.1 Fracture surface analysis

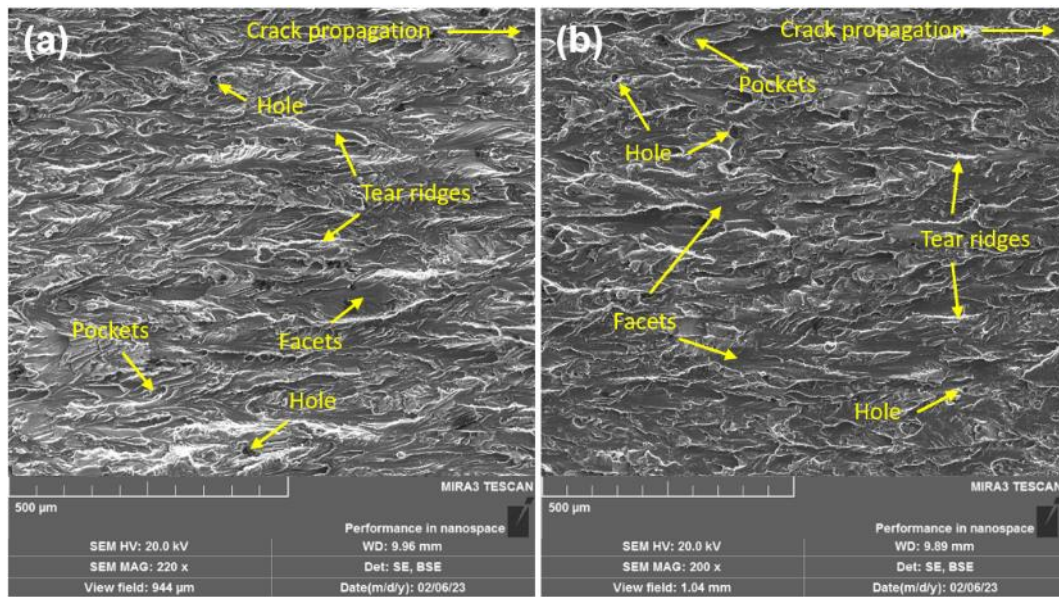
Further investigation on FCP behavior of specimens from BM and reinforced with FS was carried out with fracture surface analysis by using SEM imaging in different ΔK ranges, from regions around the active zone beneath the deposit region. Figures 61 and 62 illustrates the fracture surface after FCP test at the pre-cracking zone, at the initial stage of FCP (low ΔK I region), low ΔK II region and a moderate ΔK regions for BM.

Figure 61 – Fracture surface morphology from AA7475-T761 BM. Pre-cracking zone (a) and low ΔK I (b).



Source: the author.

Figure 62 – Fracture surface morphology from AA7475-T761 BM. Low ΔK II (a) and moderate ΔK (b).



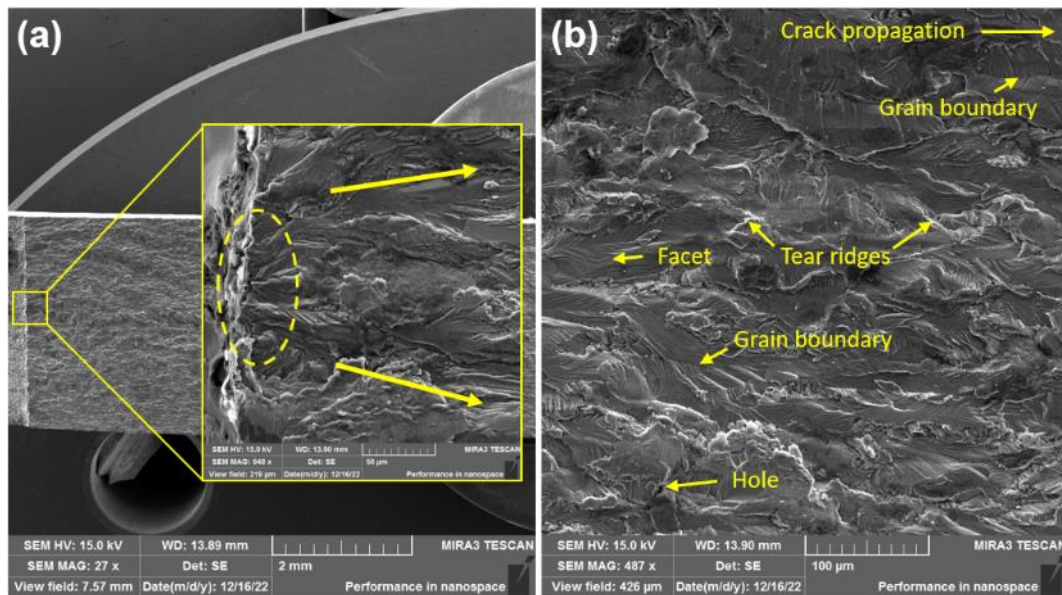
Source: the author.

In Figure 61a, the pre-crack nucleates and spreads toward crack propagation direction in a “fan-shaped” pattern with the expansion of facets along different orientations, as seen by the yellow circle and arrows. In Figure 61b, the fracture surface in low ΔK I is flat and propagates in the form of transgranular fracture. There are many flat pockets connected by tear ridges, indicating that the crack propagates in different orientations, probably crossing twist grain boundaries. (96) Furthermore, some deep multi-sized cavities can be observed this feature is likely related to Orowan mechanisms on particles during FCP.

In Figure 62a, the fracture morphology is featured with many tear ridges and enlarged pockets following the crack growth direction. Many flat surfaces between tear ridges are also present. The increase in ΔK influences the frequency of fracture features: less tear ridges, more flat surfaces and less pockets, as can be seen in Figure 62b, which can be related to differences in the crack front resistance.

Figure 63 shows the fracture morphology from FS specimen after FCP at the pre-cracking zone and at the initial stage of FCP (low ΔK I region).

Figure 63 – Fracture surface morphology from FS specimen. Pre-cracking zone (a) and low $\Delta K I$ region (b).

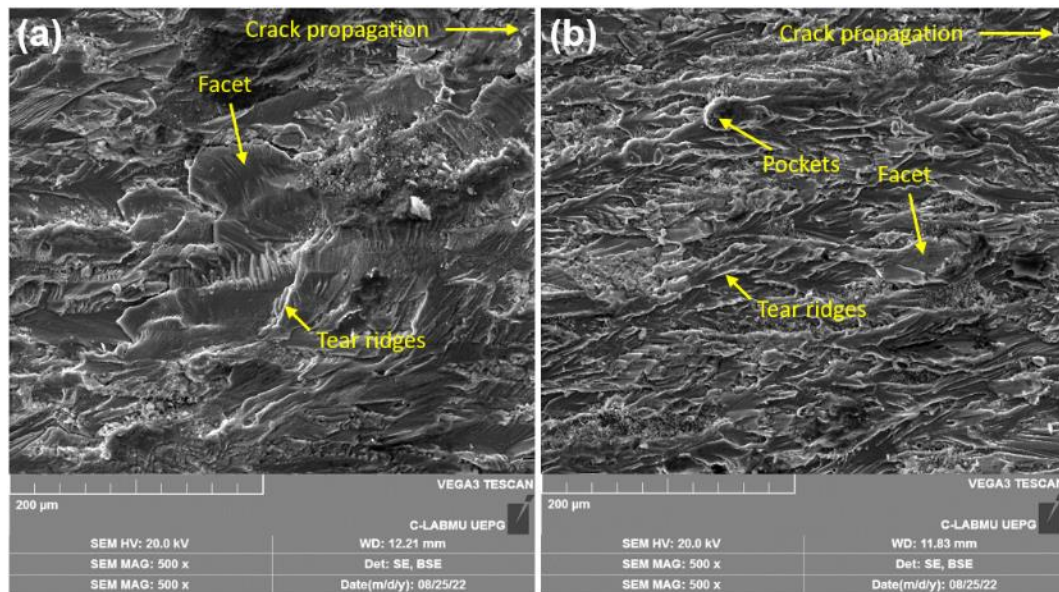


Source: the author.

In Figure 63a, the crack nucleates and spreads toward the propagation direction in more than one region. The image with higher magnification shows a crack nucleation site spreading along fatigue crack facets with different height and distinct direction. Figure 63b shows less occurrence of tear ridges and presence of larger flat surfaces. These many flat surfaces have resulted from the lower crack propagation rate as a consequence of compressive residual stress from FS process. Thus, crack deviation from the crack path crossing twist grain boundaries can be more highlighted.

Figure 64 shows the fracture morphology from FS specimen after FCP in low $\Delta K II$ and moderate ΔK .

Figure 64 – Fracture surface morphology from FS specimen. Moderate ΔK (a) and (b).



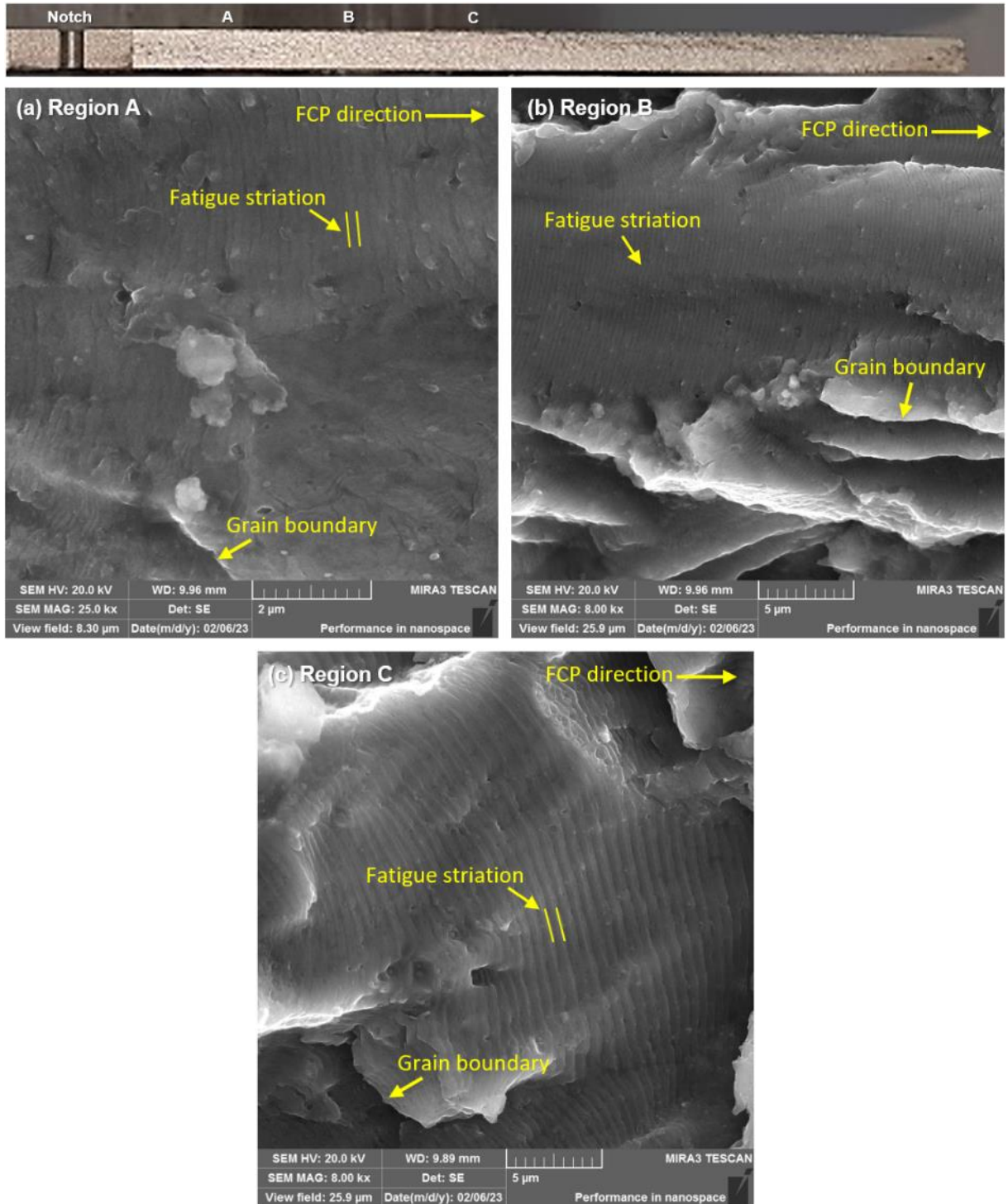
Source: the author.

In Figure 64a, the fracture morphology is featured with a combination of pockets and broad-flat surfaces containing multiple crack paths. However, less occurrence of tear ridges and pockets is observed. The increase in ΔK influences the frequency of tear ridges, height and orientation of facets, as can be seen in Figure 64b. This change in fracture morphology can be likely related to the absence of compressive residual stress. Accordingly, there is an increase in enlarged pockets and formation of smoother tear ridges similar to BM specimens. This feature was also observed in a study of FCP in AA2A97-T3 sheets at values of ΔK upon $20 \text{ MPa}\sqrt{\text{m}}$. (97) According to a study of FCP behavior in AA2524-T3, the crack propagates in different crystal planes, generating tear ridges. (98)

The mechanism of stable crack growth is commonly featured by fatigue striations, as observed in Figures 65 and 66 for AA7475-T761 BM and FS specimen, respectively. The parallel lines indicated in the figure are referred to as fatigue striations, oriented nearly normal to the direction of overall crack propagation. Each striation is related to the incremental advance of the crack front for a loading cycle and the spacing between striations is also correlated to ΔK range. (99)

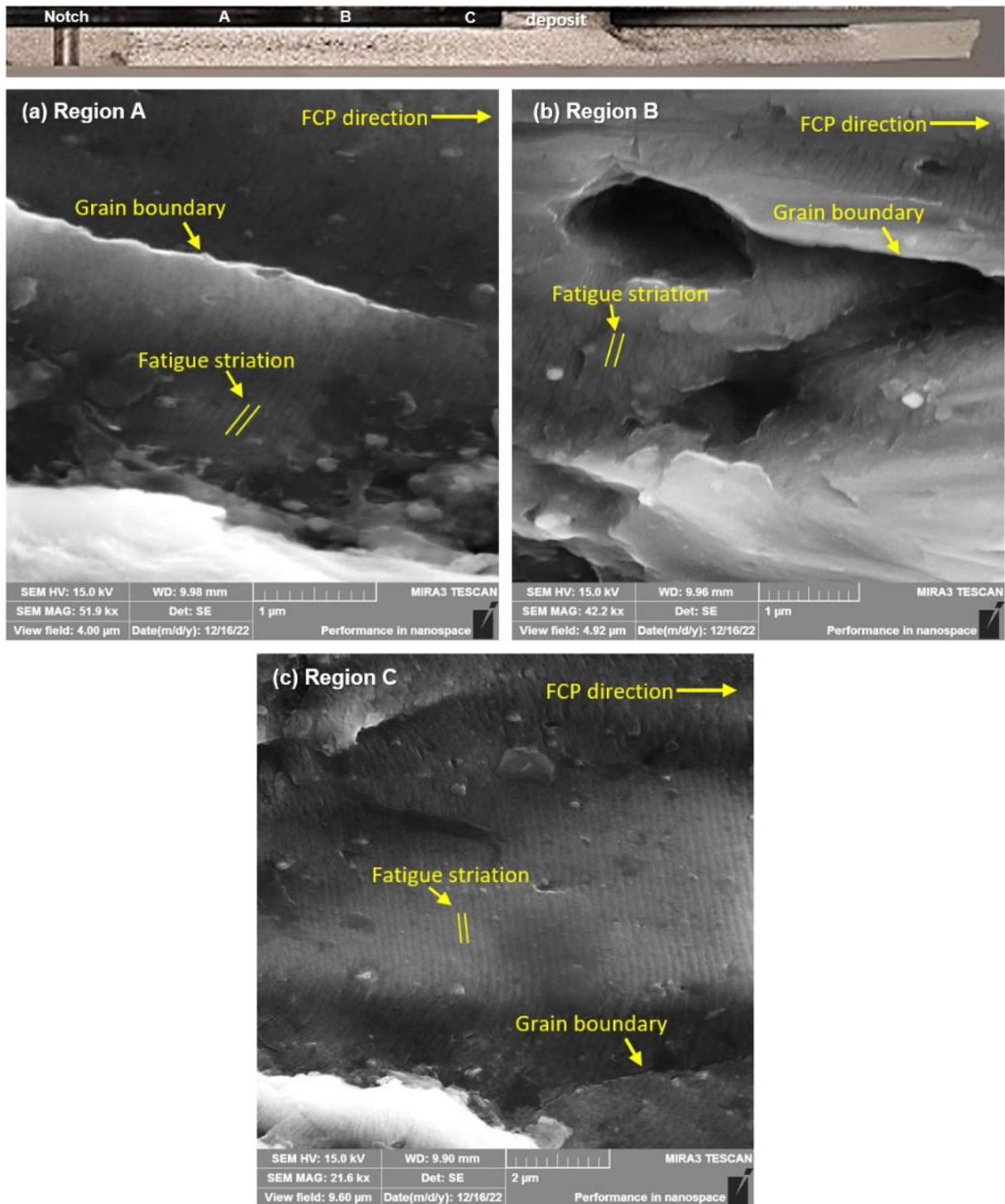
In this study, average striation spacing for uncoated specimen and FS deposit configurations was measured. In this way, it was possible to analyze the compressive residual stress effect from the FS on the striation spacing and to compare it with the BM specimen.

Figure 65 – Fatigue striation marks for BM specimen at different ΔK ranges: (a) region A, (b) region B and (c) region C.



Source: the author.

Figure 66 – Fatigue striation marks for FS specimen at different ΔK ranges: (a) region A, (b) region B and (c) region C.



Source: the author.

Table 9 shows the average striation spacing from BM and FS specimen on different regions.

Table 9 – Average striation spacing for BM and FS specimen in different regions.

Specimen	Average striation spacing (μm)		
	Region A (low ΔK I)	Region B (low ΔK II)	Region C (moderate ΔK)
AA7475-T761 BM	0.153 ± 0.019	0.259 ± 0.018	0.591 ± 0.045
FS specimen	0.077 ± 0.004	0.093 ± 0.014	0.157 ± 0.010

Source: the author.

The results from Table 9 highlight that the average striation spacing for FS specimens are lower in relation to BM, with a decrease of around 50%, 64% and 73% for Region A, B and C respectively. This reveals that the compressive residual field is effective in the surrounding of the active zone, confirming that the crack growth retardation is achieved by FS processing. Comparing FS to other techniques, a proportional increase in fatigue striation spacing to ΔK range was also observed in a shot peened 7B50-T7751 aluminum alloy. Moreover, the striation spacing was around $3\mu\text{m}$ for low ΔK . (99) The lowest fatigue striation spacing achieved by laser peening in 6061-T6 aluminum alloy was $0.12\ \mu\text{m}$ on the crack arrest region ($a = 25\ \text{mm}$), representing a decrease of 16% in relation to the untreated material. (100) Also, in another work with friction stir welded AA2195 plates subjected to laser peening showed a decrease in striation spacing in about 22% for 1 mm of crack length, and 32% for 10 mm of crack length. (101) Then, FS layer deposition also influences the fatigue striation, showing a decrease in spacing in the region around the active zone, similarly to other processes that induces compressive stresses.

6 CONCLUSIONS

This work investigated the feasibility of FS layer deposition of AA2024 on AA7475 aluminum alloys as fatigue crack growth retarder. The main findings of this study, focusing on the stated objectives, is addressed as follow:

- Successful deposition of AA2024-T351 alloy over high strength AA7475-T761 alloy was achieved by FS.
- Regarding process stability and visual appearance, satisfactory conditions are reached with lower v_x and lower R_s .
- The interface areas and the deposits consist of fine-grained microstructure with sound bonding between the dissimilar materials for all parameters.
- EDS results show that the bonding is achieved by interdiffusion, creating a 7.5 μm thick diffusion zone across the dissimilar interface.
- Microhardness is affected by FS, generating a HAZ in the substrate and lower microhardness values near bonding interface, for both substrate and deposit material.
- Deposition of AA2024 studs onto AA7475 substrate by FS produces an offset with the center of the deposit towards AS. Consequently, the HAZ in the substrate is slightly more prominent on the RS than on the AS.
- Bending test results show excellent bond strength and the absence of delamination in the lateral surface of the AS region for all conditions tested. In contrast, small delamination was predominant in the RS region.
- The tensile test results showed a slight decrease of 1.4% in UTS and significative reduction of 25,8 % in YS for the FS specimens. Although, an increase of 37% in elongation was achieved with the reinforcement provided by FS process.
- The fractography after tensile test in BM reveals a morphology derived from transgranular shear fracture, along a 45° direction, which is common for ductile metals. For FS specimens, the deposit region presents numerous small dimples, and isolated dimples within broad-flat surfaces in the substrate.
- All FS configuration investigated in this work presented a remarkable increase in fatigue life. Specimens with A-A and R-R configuration increased 460% and 568% in fatigue life, respectively. Also, the post-machining step in R-A

configuration increased in 739% the fatigue life, however secondary cracks propagating in the machined surface were observed.

- The contribution of the compressive residual stress in FS specimens is expected to be effective for up to 40.00 mm of crack length, which still comprehends low ΔK . Also, a reduction of 70% and 88% in FCGR is achieved for A-A and R-R, respectively. A reverse behavior is observed for moderate ΔK , due to the active zone beneath the deposit region.
- The fracture surface observed after FCP indicates a transgranular fracture, with presence of facets, tear ridges and pockets. The increase in ΔK influences the frequency of these fracture features, with increase of flat surfaces and decrease of tear ridges and pockets as the crack front resistance is diminished.
- The average striation spacing measured for FS specimens decreases in 50%, 64% and 73% for Region A, B and C, respectively, revealing the presence of a strong compressive stress field around the active zone beneath the deposit region.

7 SUGGESTIONS FOR FUTURE WORK

- Measure and precisely record the process temperature, in order to fully understand the influence on microstructure changes and fatigue crack propagation behavior.
- Investigate the influence of process parameter in the offset between deposit's center and stud's center.
- Use DIC methods for crack opening displacement measures and plastic deformation zone identification, using appropriate recording system.
- Evaluate the residual stress profile, with information on the depth distribution, for deposited and uncoated specimens, and also for machined specimens.

REFERENCES

- 1 DAS, S. K.; YIN, W. The worldwide aluminum economy: the current state of the industry. **JOM**, vol. 59, p. 57-63, 2007.
- 2 KAH, P.; RAJAN, R. MARTIKAINEN, J.; SUORANTA, R. Investigation of weld defects in friction-stir welding and fusion welding of aluminum alloys. **International Journal of Mechanical and Materials Engineering**, vol. 10, n. 26, 2015.
- 3 DOVZHENKO, G. Residual stresses and fatigue crack growth in friction surfacing coated Ti-6Al-4V sheets. **Journal of Materials Processing Technology**, vol. 262, p. 104-110, 2018.
- 4 STARKE, E. A.; STALEY, J. T. Application of modern aluminum alloys to aircraft. **Progress In Aerospace Sciences**, v. 32, n. 2-3, p. 131-172, 1996.
- 5 MOURITZ, A. P. (ed.). 1 – introduction to aerospace materials. In: MOURITZ, A. P. (ed.). **Introduction to aerospace materials**. Cambridge: Woodhead Publishing Limited, 2012. p. 39-56. Disponível em: <https://doi.org/10.1533/9780857095152.39>. Access in: 11 jan. 2022.
- 6 NIU, M. Chun-Yung. **Airframe structural design**: practical design information and data on aircraft structures. California: Conmilit Press Ltd, 1988. 612 p.
- 7 MOURITZ, A. P. (ed.). 8 – aluminum alloys for aircraft structures. In: MOURITZ, A. P. (ed.). **Introduction to aerospace materials**. Cambridge: Woodhead Publishing Limited, 2012. p. 173-201. Available in: <https://doi.org/10.1533/9780857095152.173>. Access in: 11 jan. 2022.
- 8 MOURITZ, A. P. (ed.). 3 - materials and material requirements for aerospace structures and engines. In: MOURITZ, A. P. (ed.). **Introduction to aerospace materials**. Cambridge: Woodhead Publishing Limited, 2012. p. 39-56. Available in: <https://doi.org/10.1533/9780857095152.39>. Access in: 11 jan. 2022.
- 9 MISHRA, R. S.; KOMARASAMY, M. **Friction stir welding of high-strength 7xxx aluminum alloys**. Oxford: Elsevier Inc, 2016. 104 p.
- 10 CHAWLA, K. K. **Composite materials**: science and engineering. 3. ed. New York: Springer, 2012. 542 p.
- 11 TOTTEN, G. E.; MACKENZIE, D. S. **Handbook of Aluminum**: physical metallurgy and processes. New York: Marcel Dekker, 2003. 1296 p.
- 12 MEYERS, M.; CHAWLA, K. **Mechanical behavior of materials**. 2. ed. Cambridge: Cambridge University Press, 2009. 856 p.
- 13 HATCH, J. E. **Aluminum**: properties and applications. ASM International, 1984. 424 p.

- 14 HAIDEMENOPOULOS, G. N. **Physical metallurgy: principles and design**. Florida: Taylor and Francis Group, 2018. 475 p.
- 15 MISHRA, R. S.; SIDHAR, H. **Friction stir welding of 2XXX aluminum alloys including Al-Li alloys: a volume in the friction stir welding and processing book series**. Texas: Elsevier, 2017, 102 p.
- DAVIS, J. R. **Aluminum and aluminum alloys**. 1nd. Ohio: ASM International, 1993.
- 16 BOAG, A.; HUGHES, A. E.; WILSON, N. C.; TORPY, A.; MACRAE, C. M.; GLENN, A. M.; MUSTER, T. H. How complex is the microstructure of AA2024-T3? **Corrosion Science**, vol. 51, p. 1565-1568, 2009.
- 17 CHEN, J.; ZHEN, L.; YANG, S.; SHAO, W.; DAI, S. Investigation of precipitation behavior and related hardening in AA7055 aluminum alloy. **Materials Science and Engineering: A**, vol. 500, p. 34-42, 2009.
- 18 SCHIJVE, Jaap. Fatigue damage in aircraft structures, not wanted, but tolerated? **International Journal of Fatigue**, v. 31, n. 6, p. 998-1011, jun. 2009.
- 19 MOURITZ, A. P. (ed.). 20 – fatigue of aerospace materials. In: MOURITZ, A. P. (ed.). **Introduction to aerospace materials**. Cambridge: Woodhead Publishing Limited, 2012. p. 469-497. Available in: <https://doi.org/10.1533/9780857095152.469>. Access in: 11 jan. 2022.
- 20 WANHILL, R; BARTER, S; MOLENT, L. **Fatigue crack growth failure and lifing analyses for metallic aircraft structures and components**. Netherlands: Springer, 2019. 99 p.
- 21 FINDLAY, S. J.; HARRISON, N. D. Why aircraft fail. v. 5, n. 11, p. 18-25, nov. 2002.
- 22 CAMPBELL, G. S.; LAHEY, R. A survey of serious aircraft accidents involving fatigue fracture. **International Journal of Fatigue**, v. 6, n. 1, p. 25-30, jan. 1984.
- 23 National Transportation Safety Board–NTSB (2013) B733depressurisation while en-route, Accident Number:DCA11MA039
- 24 ANDERSON, T. L. **Fracture mechanics: fundamentals and applications**. Florida: Taylor and Francis Group, 2017, 661 p.
- 25 IRWIN, G. R. **Fracture**, in: Handbuch der physik, Bd. IV, Springer-Verlag, Berlin/Heidelberg, vol. 551. 1958.
- 26 PARIS, P. C.; ERDOGAN, F. A critical analysis of crack propagation laws. **Journal of Basic Engineering**, vol. 85, 1963.

- 27 KRUPP, U. **Fatigue crack propagation in metals and alloys: microstructural aspects and modelling concepts**. Weinheim: Wiley-VCH, 2007, 287 p.
- 28 SCHIJVE, J. **Fatigue of structures and materials**. 2. ed. Netherlands: Springer Science+Business Media, 2009. 621 p.
- 29 ALDERLIESTEN, R. C. Designing for damage tolerance in aerospace: a hybrid material technology. **Materials and Design**, vol. 66, p. 421-428, 2014.
- 30 MCCLUG, R. A literature survey on the stability and significance of residual stresses during fatigue. **Fatigue and Fracture of Engineering Materials and Structures**, vol. 30, n. 3, p. 173–205, 2007.
- 31 KUMAR, N.; MISHRA, R. S.; BAUMANN, J. A. **Residual stresses in friction stir welding**. Elsevier, 2014, 50 p.
- 32 WITHERS, P. J. Residual stress and its role in failure. **Reports on Progress in Physics**, vol. 70, n. 12, p. 2211-2264, 2007.
- 33 PAVAN, M. **Laser shock peening for fatigue life enhancement of aerospace components**. 2017. 255 f. Tese (Doutorado) - Faculty Of Engineering, Environment And Computing, Coventry University, 2017.
- 34 WITHERS, P.; BHADESHIA, H. Residual stress part 1: measurement techniques, **Materials Science and Technology**, vol. 17, n. 355365, 2001.
- 35 (2009). **Residual Stress**. In: Schijve, J. (eds) *Fatigue of Structures and Materials*. Springer, Dordrecht.
- 36 VAN DEN BERG, N.; XIN, H.; VELJKOVIC, M. Effects of residual stresses on fatigue crack propagation of an orthotropic steel bridge deck. **Materials and Design**, vol. 198, n. 109294, 2021.
- 37 WEBSTER, G.; EZEILO, A. Residual stress distributions and their influence on fatigue life-times, **International Journal of Fatigue**, vol. 23, p. 375-383, 2001.
- 38 KASHAEV, N.; KELLER, S.; STARON, P.; MAAWAD, E.; HUBER, N. On the prediction of fatigue crack growth based on weight functions in residual stress field induced by laser shock peening and laser heating. **Fatigue and Fracture of Engineering Materials and Structures**, v. 44, n. 12, p. 3463-3481, sep. 2021.
- 39 CARVALHO, A. L. M.; VOORWALD, H. K. C. Influence of shot peening and hard chromium electroplating on the fatigue strength of 7050-T7451 aluminum alloy. **International Journal of Fatigue**, vol. 29, n. 7, p. 1282-1291, jun. 2007.

- 40 ASWEGEN, D. C.; POLESE, C. Experimental and analytical investigation of the effects of laser shock peening processing strategy on fatigue crack growth in thin 2024 aluminum alloy panels. **International Journal of Fatigue**, vol. 142, n. 105969, jan. 2021.
- 41 SCHNUBEL, D.; HORSTMANN, M.; HUBER, N. Retardation of fatigue crack growth in aircraft aluminum alloys via laser heating. **International Journal of Structural Integrity**, vol. 4, p. 429–445, 2013.
- 42 STALEY, J.; LEGE, D. Advances in aluminum alloy products for structural applications in transportation. **Journal de Physique IV Proceedings**, EDP Sciences, 03 (C7), pp.C7-179-C7-190. 1993.
- 43 UNIVERSITY OF WATERLOO. **Residual Stress**. Available in: <https://uwaterloo.ca/fatigue-stress-analysis-lab/research/residual-stress>. Access in: 29th april 2022.
- 44 SCHIJVE, J. Crack stoppers and arall laminates. **Engineering Fracture Mechanics**, vol. 37, n. 2, p. 405-421, 1990.
- 45 PACCHIONE, M.; HOMBERGSMEIER, E. Hybrid Metal Laminates for Low Weight Fuselage Structures. **Engineering Against Fracture**, p. 41-57, 2009.
- 46 BOSCOLO, M.; ZHANG, X. Bonded crack retarders for aircraft integral metallic structures: a sensitivity analysis of design parameters. **Structures, Structural Dynamics and Materials Conference**. American Institute of Aeronautics and Astronautics, 2012.
- 47 DOVZHENKO, G. **Characterization of residual stresses in friction surfacing of Ti and Al alloys**. 2020. Thesis (Doctoral degree) – Faculty of Mathematics, Informatics and Natural Sciences Department of Physics, Universität Hamburg, Hamburg, 2020. Available in: <https://ediss.sub.uni-hamburg.de/handle/ediss/8902>. Access in: 15th April 2020.
- 48 SAKIHAMA, H.; TOKISUE, H.; KATOH, K. Mechanical properties of friction surfaced 5052 aluminum alloy. **Materials Transactions**, vol. 44, p. 2688-2694. 2003.
- 49 SHINODA, T.; LI, J. Q.; KATOH, Y.; YASHIRO, T. Effect of process parameters during friction coating on properties of non-dilution coating layers. **Surface Engineering**, vol. 14, p. 211-216. 1998.
- 50 RAFI, H. K.; RAM, G. D. J.; PHANIKUMAR, G.; RAO, K. P. Friction surfaced tool steel (H13) coatings on low carbon steel: a study on the effects of process parameters on coating characteristics and integrity. **Surface and Coatings Technology**, vol. 205, p. 232-242. 2010.
- 51 TOKISUE, H.; KATOH, K.; ASAHINA, T.; USIYAMA, T. Mechanical properties of 5052/2017 dissimilar aluminum alloys deposited by friction surfacing. **Materials Transactions**, vol. 47, p. 874-882. 2006.

- 52 RAFI, H. K.; RAM, G. D. J.; PHANIKUMAR, G.; RAO, K. P. Friction surfacing of austenitic stainless steel on low carbon steel: studies on the effects of traverse speed. London. In: **World Congress on Engineering**. 2010.
- 53 VITANOV, V. I.; VOUTCHKOV, I. I.; BEDFORD, G. M. Decision support system to optimise the Frictec (friction surfacing) process. **Journal of Materials Processing Technology**, vol. 107, p. 236-242. 2000.
- 54 BEDFORD, G. M.; VITANOV, V. I.; VOUTCHKOV, I. I. On the thermos-mechanical events during friction surfacing of high speed steels. **Surface and Coatings Technology**, vol. 141, p. 34-39. 2001.
- 55 CHANDRASEKARAN, M.; BATCHELOR, A. W.; JANA, S. Study of the interfacial phenomena during friction surfacing of mild steel with tool steel and Inconel. **Journal of Materials Science**, vol. 33, p. 2709-2717. 1998.
- 56 CHANDRASEKARAN, M.; BATCHELOR, A. W.; JANA, S. Friction surfacing of metal coatings on steel and aluminum substrate. **Journal of Materials Processing Technology**, vol. 72, p. 446-452. 1997.
- 57 FUKAKUSA, K. On the characteristics of the rotational contact plane – a fundamental study of friction surfacing. **Welding International**, vol. 10, p. 524-529. 1996.
- 58 GOVARDHAN, D.; KUMAR, A. C. S.; MURTI, K. G. K.; MADHUSUDHAN REDDY, G. Characterization of austenitic stainless steel friction surfaced deposit over low carbon steel. **Materials and Design**, vol. 36, p. 206-214. 2012.
- 59 MACEDO, M. L. K.; PINHEIRO, G. A.; DOS SANTOS, J. F.; STROHAECKER, T. R. Deposit by friction surfacing and its applications. **Welding International**, vol. 24, p. 422-431. 2010.
- 60 SAHOO, D. K.; MOHANTY, B. S.; PRADEEP, A. M. V.; JOHN, D. F. An experimental study on friction surfaced coating of aluminum 6063 over AISI 316 stainless steel substrate. **Materials Today: Proceedings**, vol. 40, p. S10-S18. 2020.
- 61 RAHMATI, Z.; AVAL, H. J.; NOUROUZI, S.; JAMAATI, R. Effects of pre-heat treatment of the consumable rod on the microstructural and mechanical properties of the friction surfaced Al-Cu-Mg alloy over pure aluminum. **Surface and Coatings Technology**, vol. 410, 2021.
- 62 GANDRA, J.; MIRANDA, R. M.; VILAÇA, P. Performance analysis of friction surfacing. **Journal of Materials Processing Technology**, vol. 242, p. 1676-1686, 2012.
- 63 FITSEVA, V. **Friction surfacing of titanium grade 1 and Ti-6Al-4V**. 2016. 116 f. Tese (Doutorado) - Technischen Universität Hamburg-Harburg (TUHH), 2016.

- 64 KALIEN, Z.; RATH, L.; ROOS, A.; KLUSEMANN, B. Experimentally established correlation of FS process temperature and deposit geometry. **Surface and Coatings Technology**, vol. 397, n. 126040, 2020.
- 65 EHRICH, J., ROOS, A., KLUSEMANN, B., HANKE, S. Influence of Mg content in Al alloys on processing characteristics and dynamically recrystallized microstructure of friction surfacing deposits. **Materials Science and Engineering: A**, vol. 819, n. 141407, 2021.
- 66 GANDRA, J.; KROHN, H.; MIRANDA, R. M.; VILAÇA, P.; QUINTINO, L.; DOS SANTOS, J. F. Friction surfacing – a review. **Journal of Materials Processing Technology**, vol. 214, o. 1062-1093, 2014
- 67 HANKE, S.; DOS SANTOS, J. F. Comparative study of severe plastic deformation at elevated temperatures of two aluminum alloys during friction surfacing. **Journal of Materials Processing Technology**, vol. 247, p. 257-267, 2017.
- 68 PIRHAYATI, P.; JAMSHIDI AVAL, H. Microstructural characterization and mechanical properties of friction surfaced AA2024-Ag composites. **Transactions of Nonferrous Metals Society of China**, vol. 30, p. 1756-1770.
- 69 EHRICH, J.; STARON, P.; KARKAR, A.; ROOS, A.; HANKE, S. Precipitation evolution in the heat-affected-zone and coating material of AA2024 processed by friction surfacing. **Advanced Engineering Materials**, vol. 24, iss. 11, 2022.
- 70 SUHUDDIN, U., MIRONOV, S., KROHN, H., BEYER, M., DOS SANTOS, J. F. Microstructural evolution during friction surfacing of dissimilar aluminum alloys, **Metall. Mater. Trans. A Phys. Metall. Mater. Sci**, vol. 43A, n. 13, p. 5224-5231, 2012.
- 71 GALVIS, J. C., OLIVEIRA, P. H. F., HUPALO, M. F., MARTINS, J. P., CARVALHO, A. L. M. Influence of friction surfacing process parameters to deposit AA6351-T6 over AA5052-H32 using conventional milling machine. **Journal of Materials Processing Technology**, vol. 245, p. 91-105, 2017.
- 72 RAFI, H. K., RAM, G. D. J., PHANIKUMAR, G., RAO, K. P. Microstructural evolution during friction surfacing of tool steel H13. **Materials Design**, vol. 32, n. 1, p. 82-87, 2011.
- 73 YU, M., ZHAO, H., ZHANG, Z., ZHOU, L., SONG, X., MA, N. Texture evolution and corrosion behavior of the AA6061 coating deposited by friction surfacing, **J. Mater. Process. Technol.**, vol. 291, n. 117005, 2021.
- 74 GANDRA, J., PEREIRA, D., MIRANDA, R. M., SILVA, R. J. C., VILAÇA, P. Deposition of AA6082-T6 over AA2024-T3 by friction surfacing - Mechanical and wear characterization. **Surf. Coatings Technol.**, vol. 223, p. 32-40, 2013

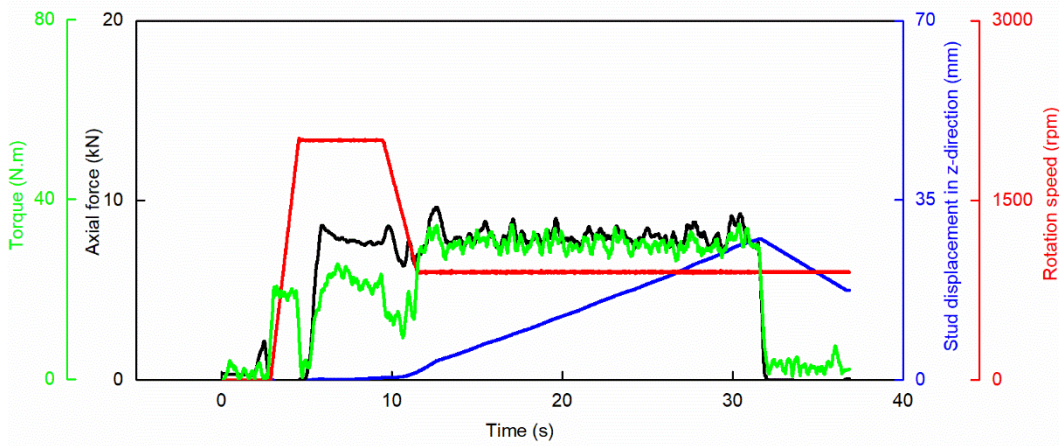
- 75 PIRHAYATI, P., AVAL, H. J. An investigation on thermo-mechanical and microstructural issues in friction surfacing of Al-Cu aluminum alloys. **Mater. Res. Express**, vol. 6, n. 056550, 2019.
- 76 ESIN, V.A., BRIEZ, L., SENNOUR, M., KÖSTER, A., GRATIOT, E., CRÉPIN, J. Precipitation-hardness map for Al Cu-Mg alloy (AA2024-T3). **J. Alloys Compd.**, vol. 854, n. 157164, 2021
- 77 STARINK, M.J., GAO, N., YAN, J.L. 2004. The origins of room temperature hardening of Al–Cu–Mg alloys. **Mater. Sci. Eng. A**, vol. 387–389, p. 222–226, 2004
- 78 RAHMATI, Z., AVAL, H. J., NOUROUZI, S., JAMAATI, R. Effect of mechtrode rotational speed on friction surfacing of AA2024 on AA1050 substrate. **CIRP J. Manuf. Scie. Technol.**, vol. 33, p. 209–221, 2021b
- 79 DE, P. S.; MISHRA, R. S. Friction stir welding of precipitation strengthened aluminum alloys: scope and challenges. **Sci. Technol. Weld. Joining** vol. 16, p. 343-347, 2011.
- 80 ZHANG, Z.; XIAO, B. L.; MA, Z. Y. Hardness recovery mechanism in the heat-affected zone during long-term natural aging and its influence on the mechanical properties and fracture behavior of friction stir welded 2024Al-T351 joints. **Acta Materialia**, vol. 73, p. 227-239, 2014.
- 81 KUMAR, S.; AHMED, M.; PANTHI, S. K. Investigation on the crack and thinning behavior of aluminum alloy 5052 sheet in stretch flanging process. **Journal of Failure Analysis and Prevention**, vol. 20, p. 1212-1228, 2020.
- 82 ASM HANDBOOK, Vol. 12, **Fractography**, ASM International, Materials Park, Ohio, USA, 1987, 517p.
- 83 HERTZBERG, R. W. **Deformation and Fracture Mechanics of Engineering Materials**. Chichester: John Wiley, 5th ed., New York , 2013, 755p.
- 84 CABRINI, M.; BOCCHI, S.; D'URSO, G.; GIARDINI, C.; LORENZI, S.; TESTA, C.; PASTORE, T. Effect of load on the corrosion behavior of friction stir welded AA7075-T6 aluminum alloy. **Materials**, vol. 13, n. 2600, 2020.
- 85 HAGHSHENAS, M.; GHARGHOURI, M. A., BHAKHRI, V.; KLASSEN, R. J.; GERLICH, A. P. Assessing residual stresses in friction stir welding: neutron diffraction and nanoindentation methods. **International Journal of Advanced Manufacturing Technology**, vol. 93, p. 3733-3747, 2017.
- 86 SYED, A. K.; ZHANG, X.; FITZPATRICK, M. E. A comparison of fatigue crack growth performance of two aerospace grade aluminum alloys reinforced with bonded crack retarders. **Fatigue & Fracture of Engineering Materials & Structures**, vol. 41, p. 1237-1242, 2017.

- 87 JI, P.; YANG, Z.; ZHANG, J.; ZHENG, L.; JI, V.; KLOSEK, V. Residual stress distribution and microstructure in the friction stir weld of 7075 aluminum alloy. **Journal of Materials Science**, vol. 22, 2015.
- 88 HATAMLEH, O.; LYONS, J.; FORMAN, R. Laser and shot peening effects on fatigue crack growth in friction stir welded 7075-T7351 aluminum alloy joints. **International Journal of Fatigue**, vol. 29, p. 421-434, 2007.
- 89 JOHN, R. Residual stress effects on near-threshold fatigue crack growth in friction stir welds in aerospace alloys. **International Journal of Fatigue**, vol. 25, p.939-948, 2003.
- 90 FLECK, N. A.; SHIN, C. S.; SMITH, R. A. Fatigue crack growth under compressive loading. **Engineering Fracture Mechanics**, vol. 21, p. 173-185, 1985.
- 91 KALAINATHAN, S.; PRABHAKARAN, S. Recent development and future perspectives of low energy laser shock peening. **Optics and Laser Technology**, vol. 81, p. 137-144, 2016.
- 92 RUBIO-GONZÁLEZ, C.; OCAÑA, J. L.; GOMEZ-ROSAS, G.; MOLPECERES, C.; PAREDES, M.; BANDERAS, A.; PORRO, J.; MORALES, M. Effect of laser Shock processing on fatigue crack growth and fracture toughness of 6061-T6 aluminum alloy. **Materials Science and Engineering: A**, vol. 386, p. 291-295, 2004.
- 93 BERRY, L.; WHEATLEY, G.; WENCHEN, M.; NEJAD, R. M.; BERTO, F. The influence of milling induced residual stress on fatigue life of aluminum alloys. **Forces in Mechanics**, vol. 7, n. 100096, 2022.
- 94 PIRHAYATI, P.; JAMSHIDI AVAL, H. Microstructural characterization and mechanical properties of friction surfaced AA2024-Ag composites. **Transactions of Nonferrous Metals Society of China**, vol. 30, p. 1756-1770.
- 95 LIU, G.; HUANG, C.; ZHAO, B.; WENG, W.; SUN, S. Effect of machined surface integrity on fatigue performance of metal workpiece: a review. **Chinese Journal of Mechanical Engineering**, vol. 34, n. 118, 2021.
- 96 CARVALHO, A. L. M; MARTINS, J. P. Effect of interrupted ageing and retrogression-reaging treatments of fatigue crack growth with a single applied overload in 7050 aluminum alloy. **Materials Research**, vol. 21, n. 3, 2018.
- 97 HAO, M.; WANG, L.; CHEN, J.; WANG, R.; LI, G. A. Intrinsic fatigue crack growth in Al-Cu-Li-Mg-Zr alloys: the effect of the iron constituent particles. **Metals**, vol. 11, n. 110, 2021.
- 98 LIU, C.; MA, L.; ZHANG, Z.; FU, Z.; LIU, L. Research on the corrosion fatigue property of 2524-T3 aluminum alloy. **Metals**, vol. 11, n. 1754, 2021.

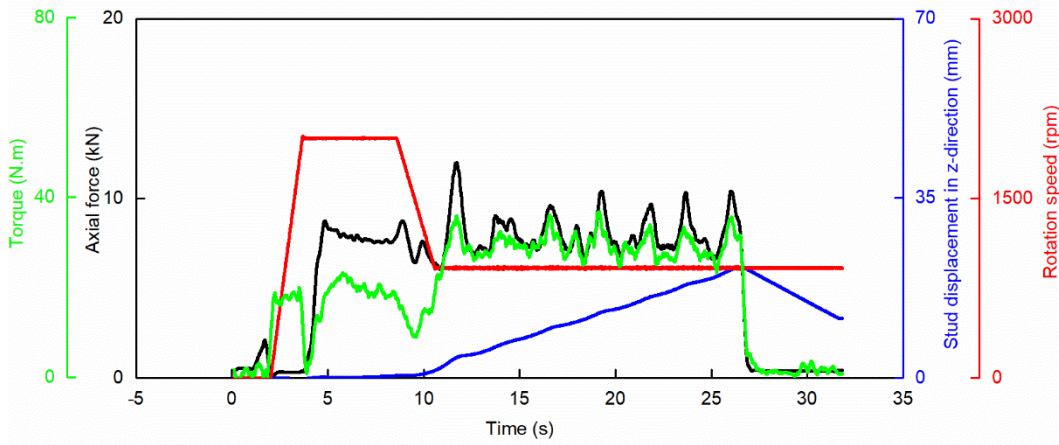
- 99 QIN, Z.; LI, B.; ZHANG, H.; WILFRIED, T. Y. A.; GAO, T.; XUE, H. Effects of shot peening with different coverage on surface integrity and fatigue crack growth properties of 7B50-T7751 aluminum alloy. **Engineering Failure Analysis**, vol. 133, n. 106010, 2022.
- 100 HUANG, S.; ZHOU, J. Z.; SHENG, J.; LUO, K. Y.; LU, J. Z.; XU, Z. C.; MENG, X. K.; DAI, L.; ZUO, L. D.; RUAN, H. Y.; CHEN, H. S. Effects of laser peening with different coverage areas on fatigue crack growth properties of 6061-T6 aluminum alloy. **International Journal of Fatigue**, vol. 47, p. 292-299, 2013.
- 101 HATAMLEH, O. A comprehensive investigation on the effects of laser and shot peening on fatigue crack growth in friction stir welded AA2195 joints. **International Journal of Fatigue**, vol. 31, p. 974-988, 2009.

APPENDIX A – PROCESS DATA GRAPHS OF FS SPECIMENS.

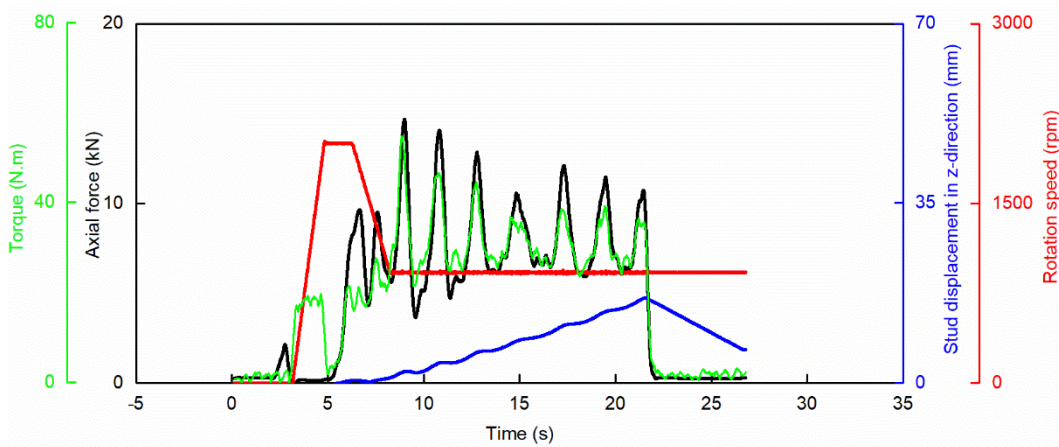
Specimen 01



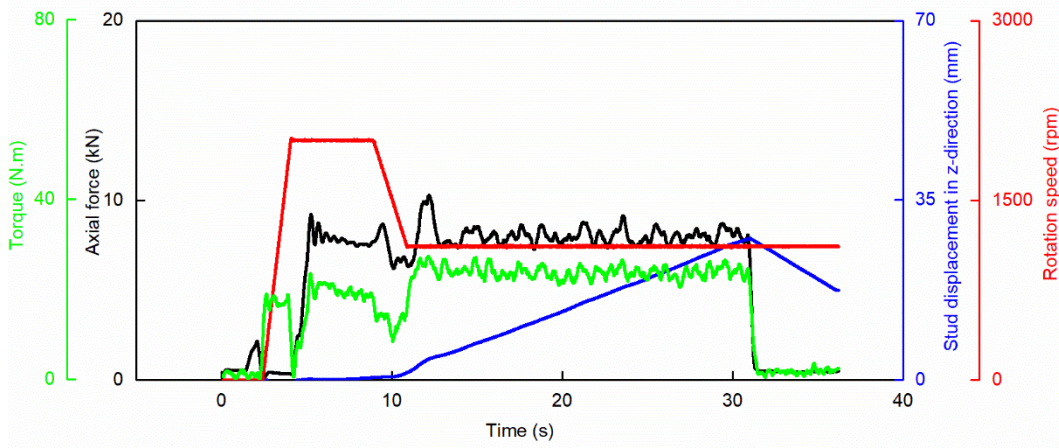
Specimen 02



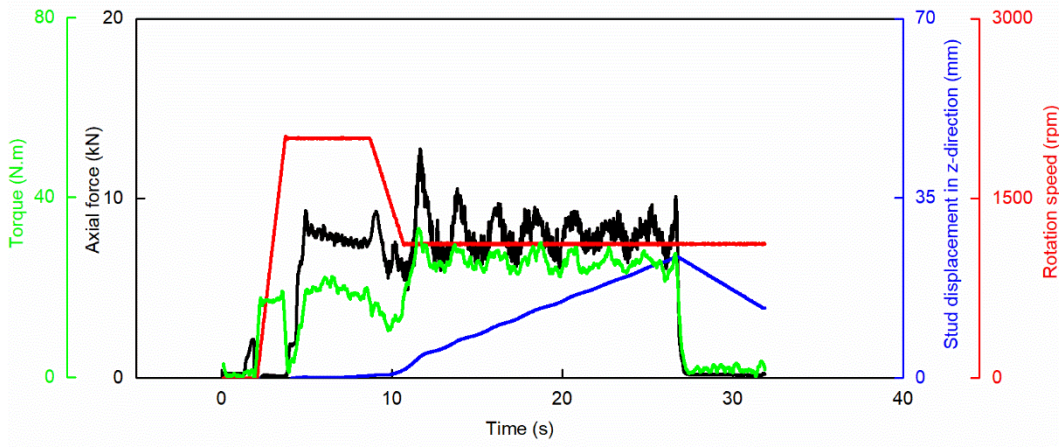
Specimen 03



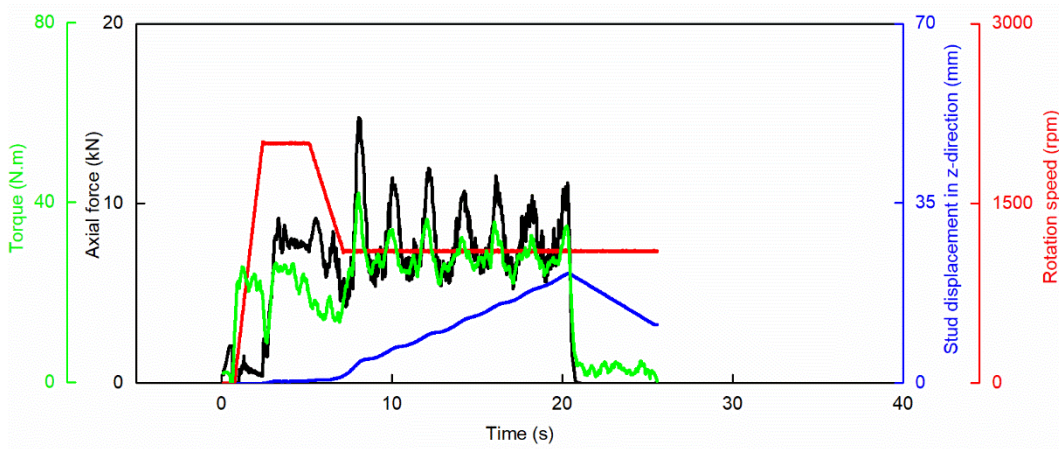
Specimen 04



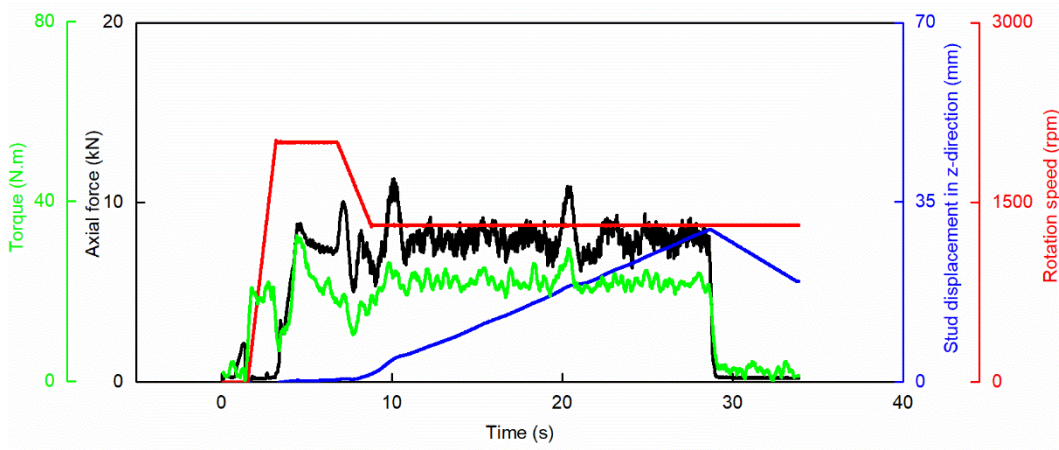
Specimen 05



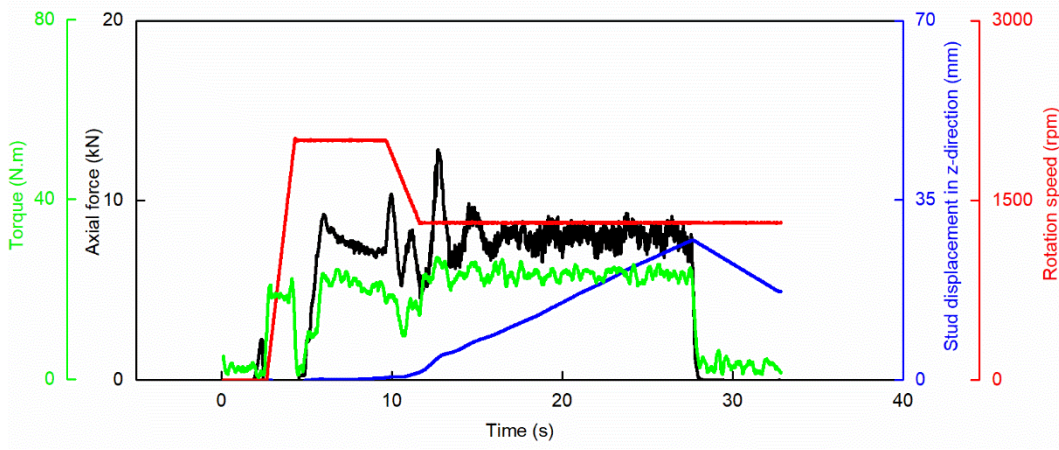
Specimen 06



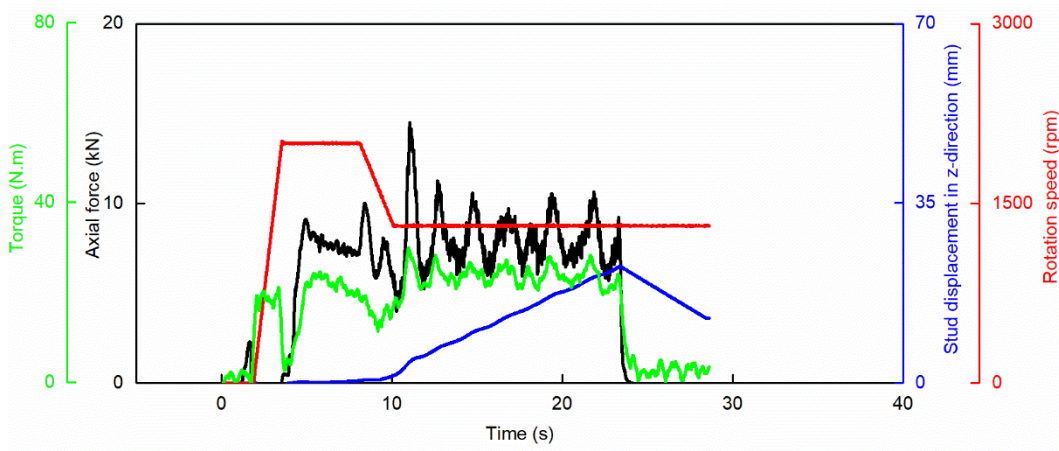
Specimen 07



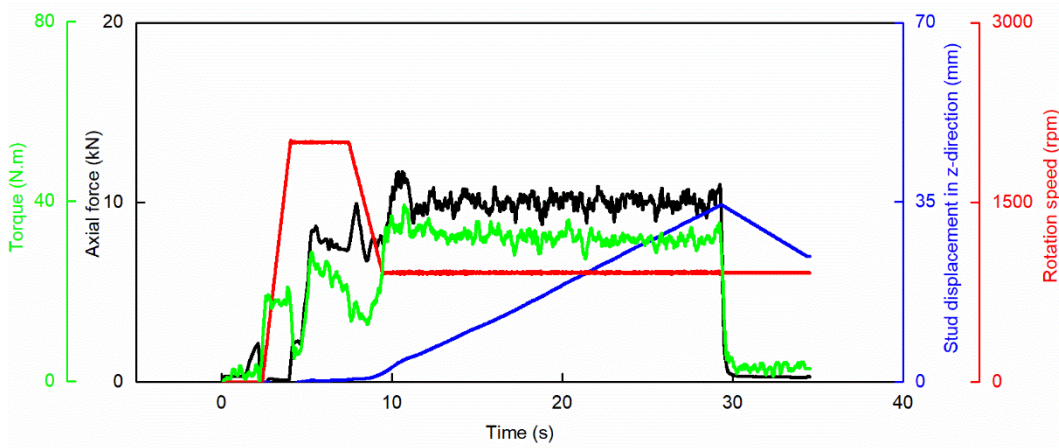
Specimen 08



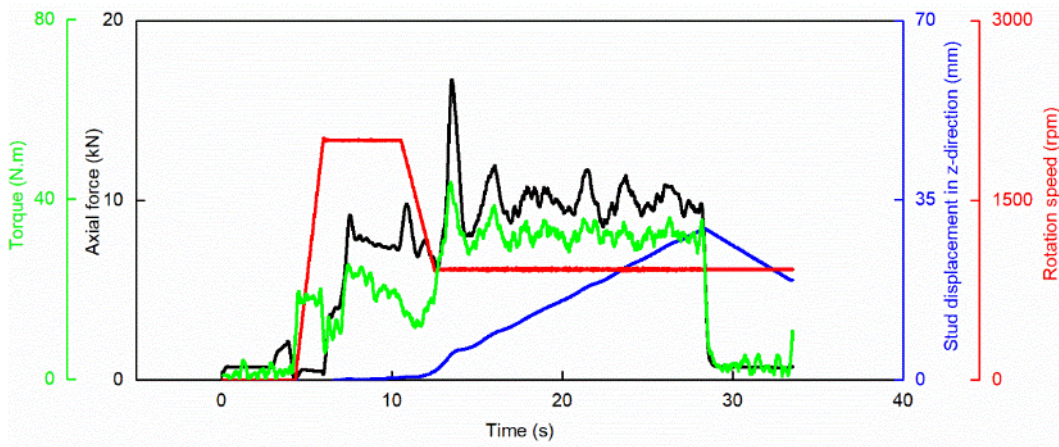
Specimen 09



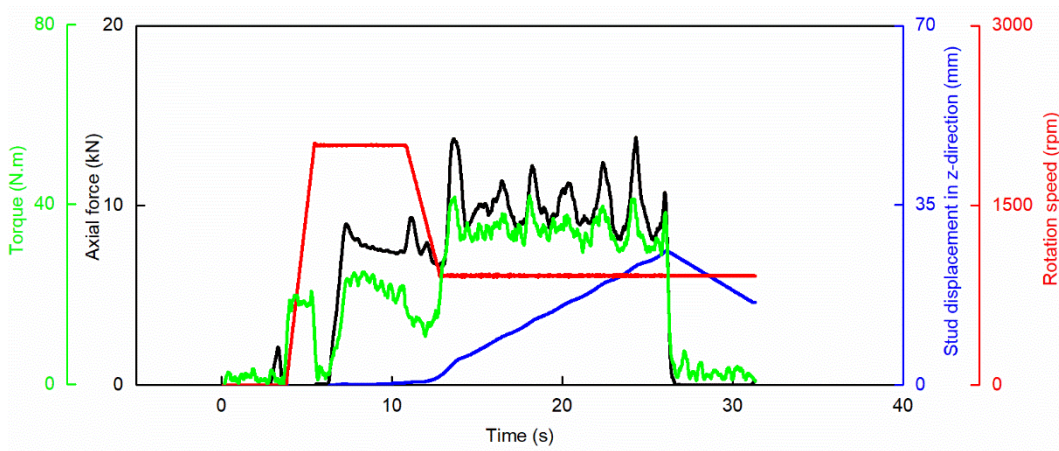
Specimen 10



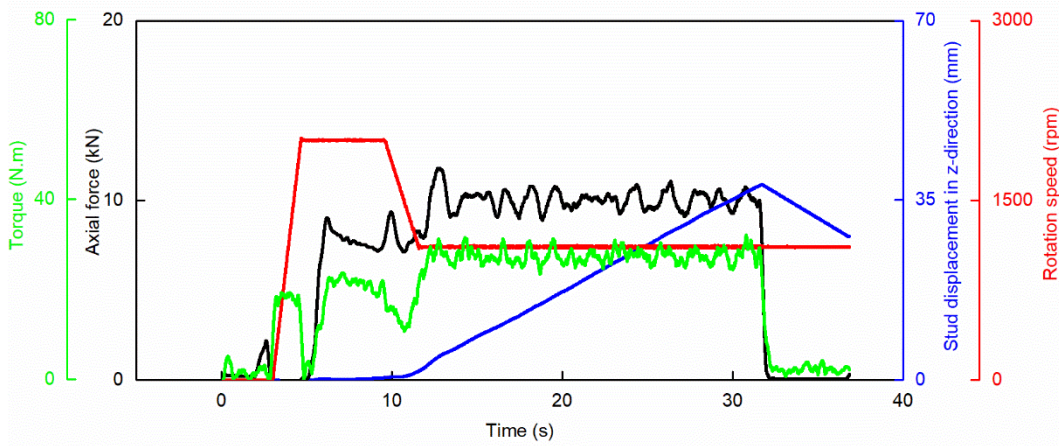
Specimen 11



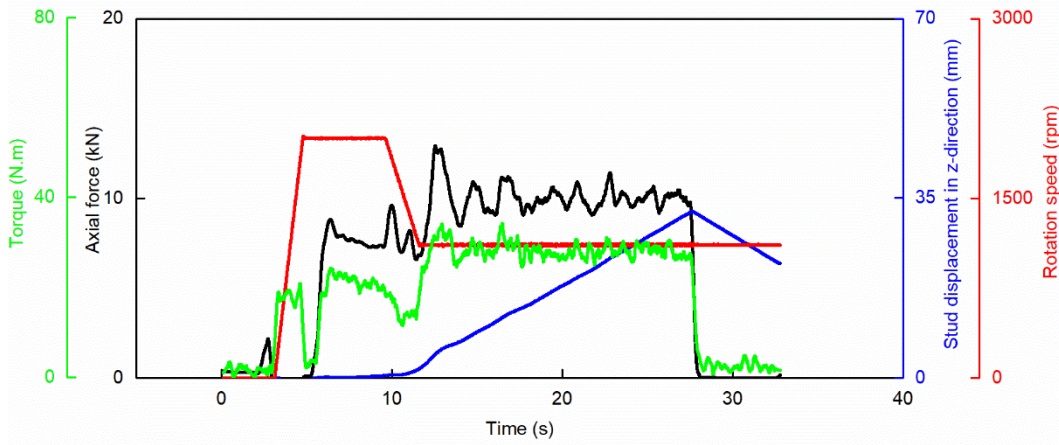
Specimen 12



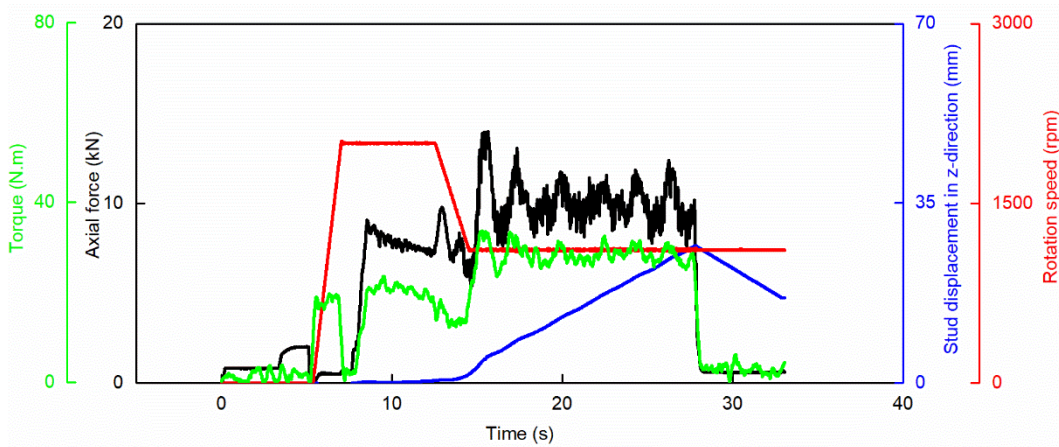
Specimen 13



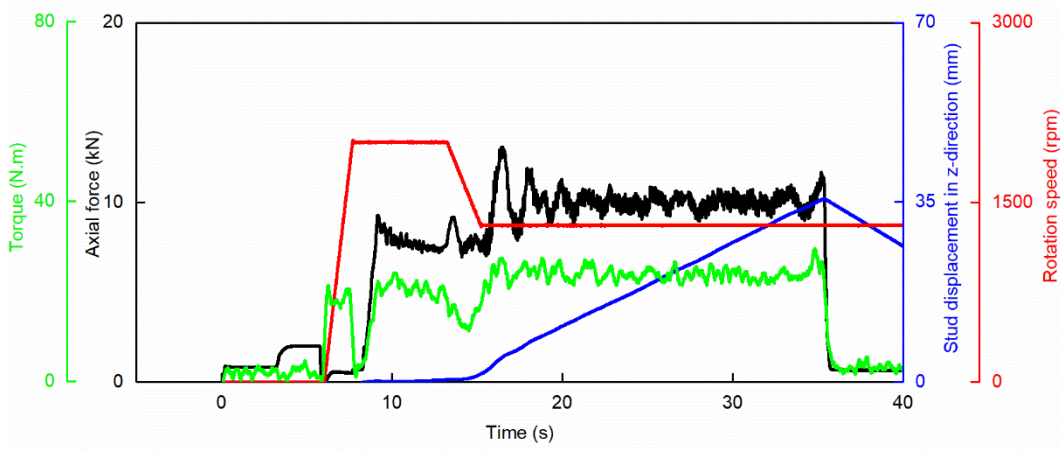
Specimen 14



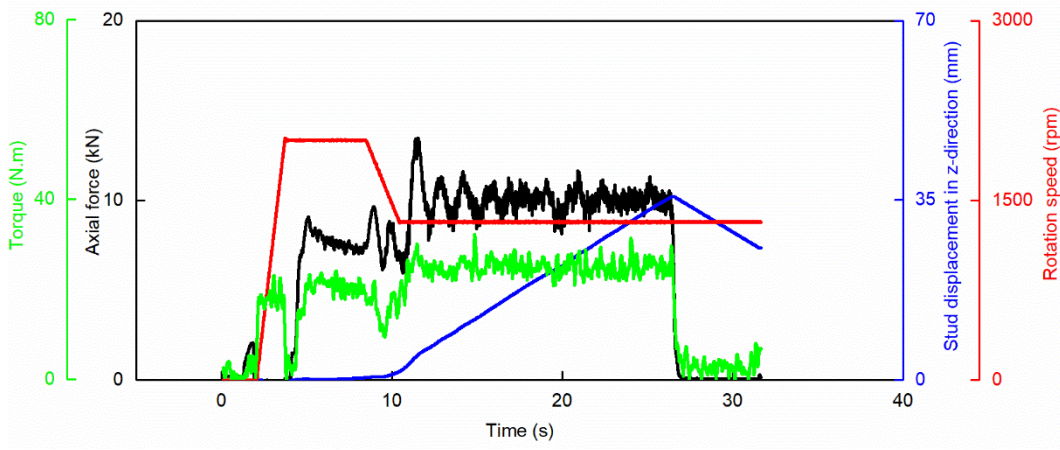
Specimen 15



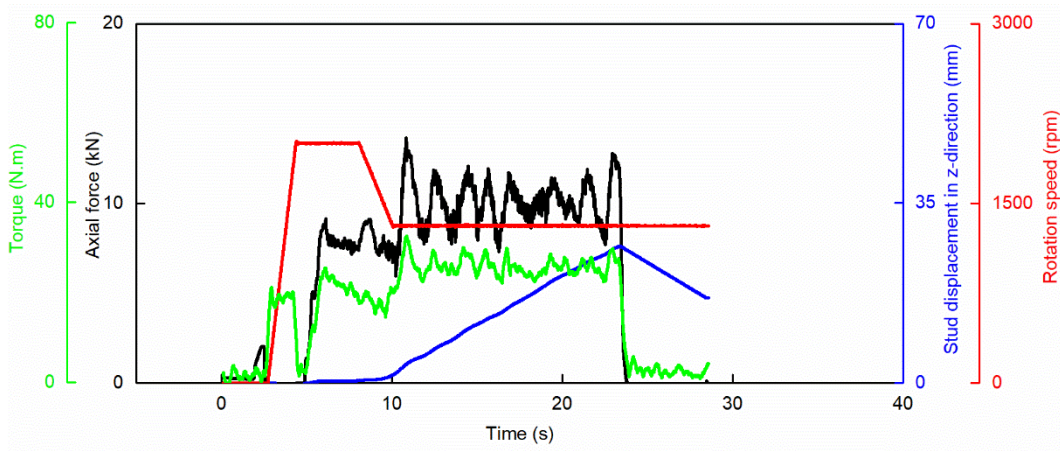
Specimen 16



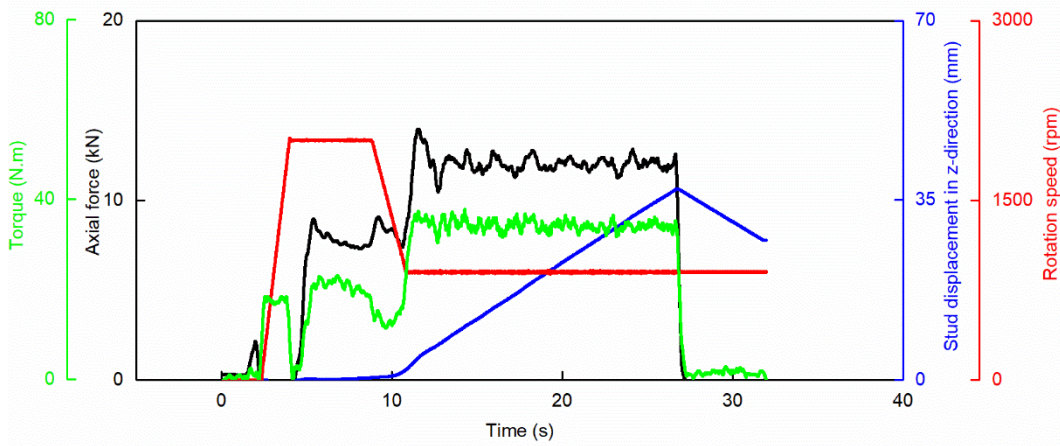
Specimen 17



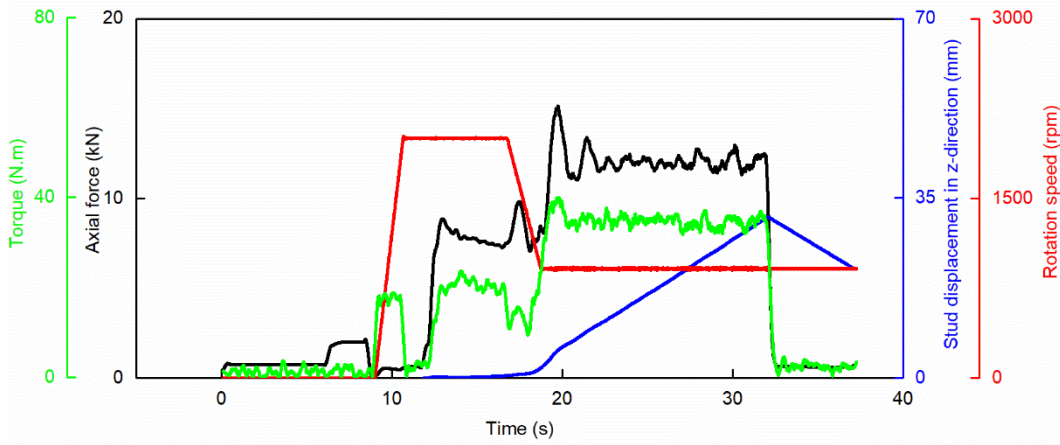
Specimen 18



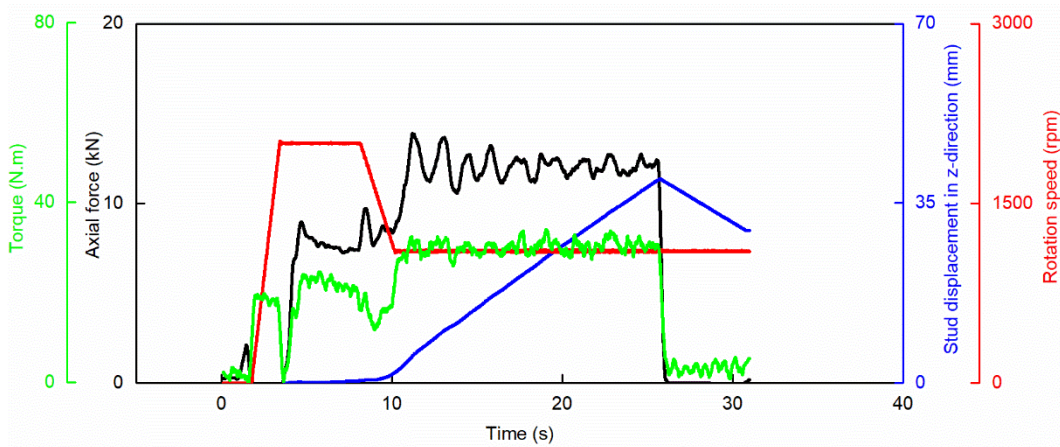
Specimen 20



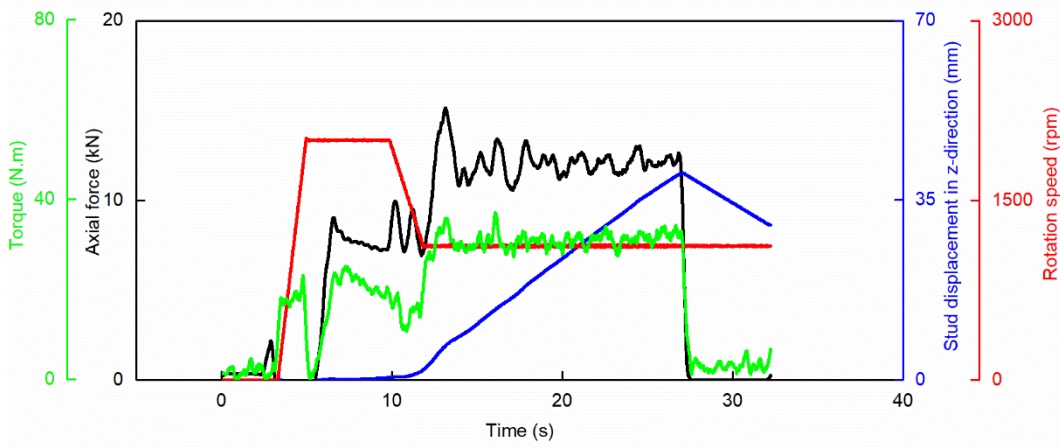
Specimen 21



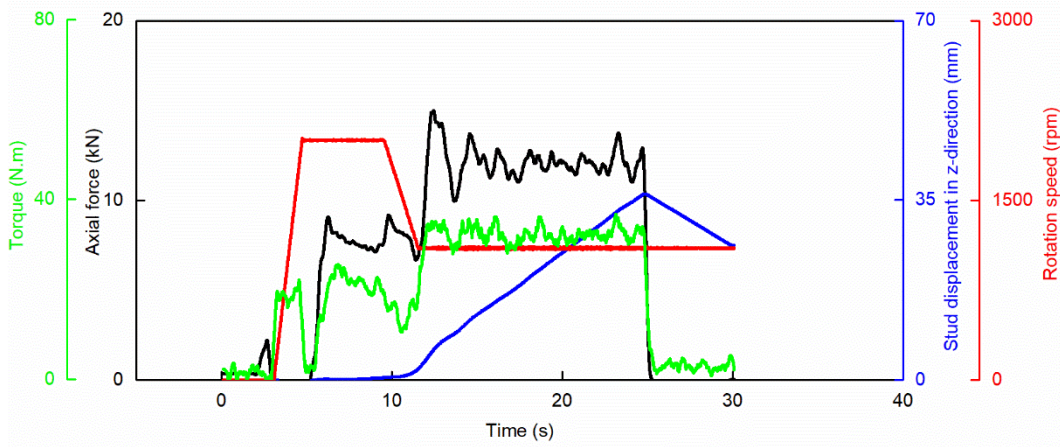
Specimen 22



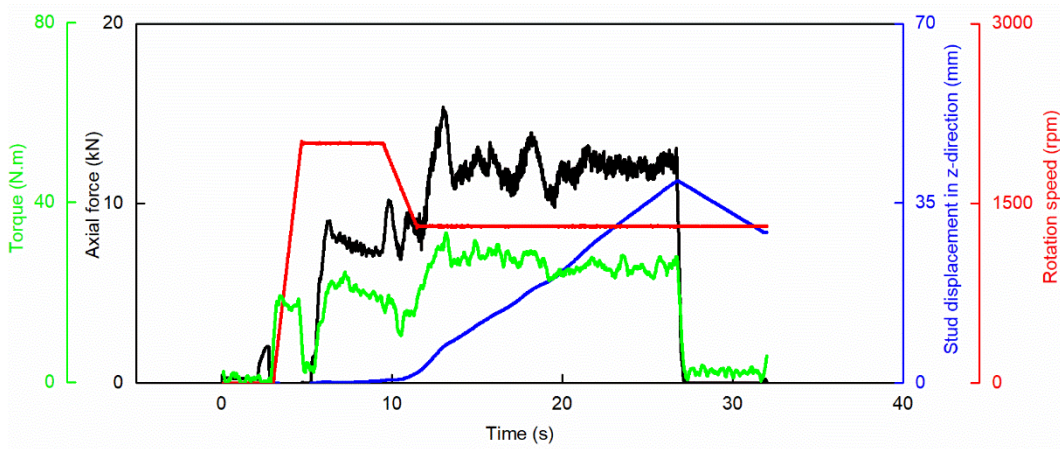
Specimen 23



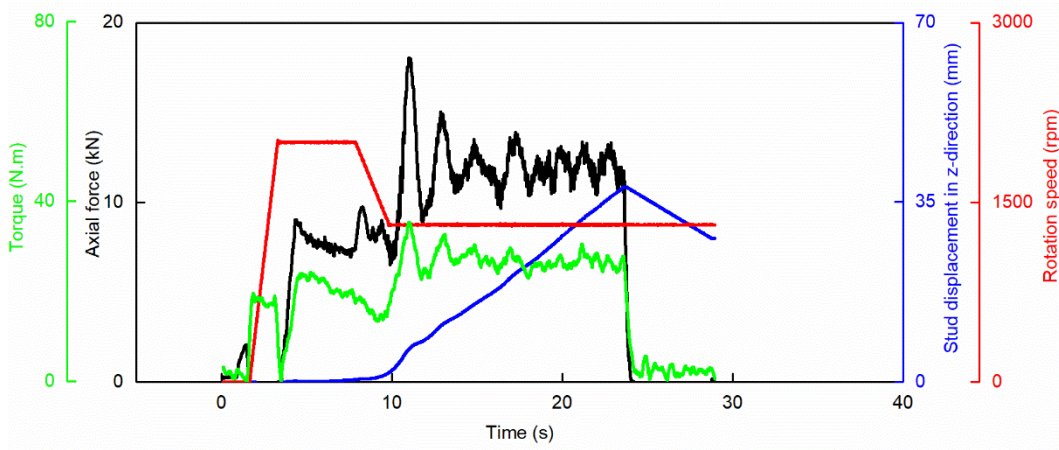
Specimen 24



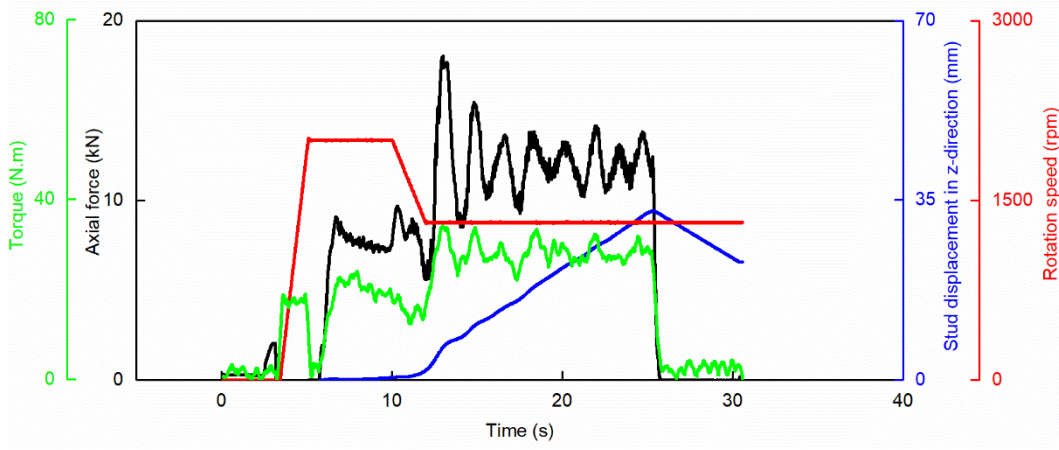
Specimen 25



Specimen 26



Specimen 27



APPENDIX B – MACROGRAPHS FROM CROSS-SECTIONED SPECIMENS.

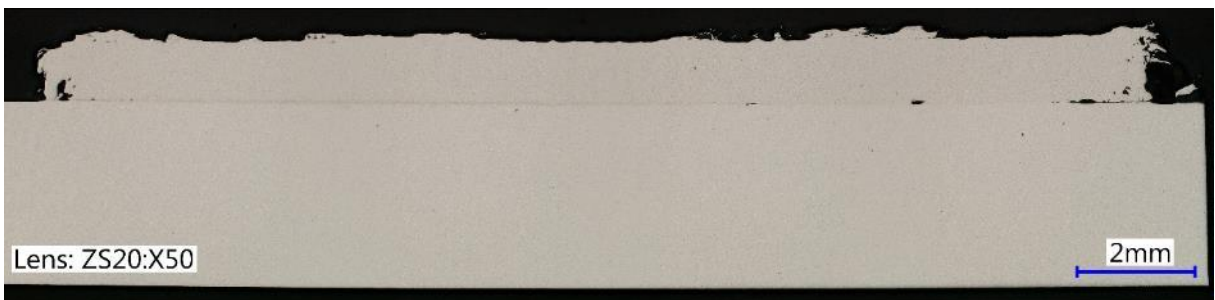
Specimen 01



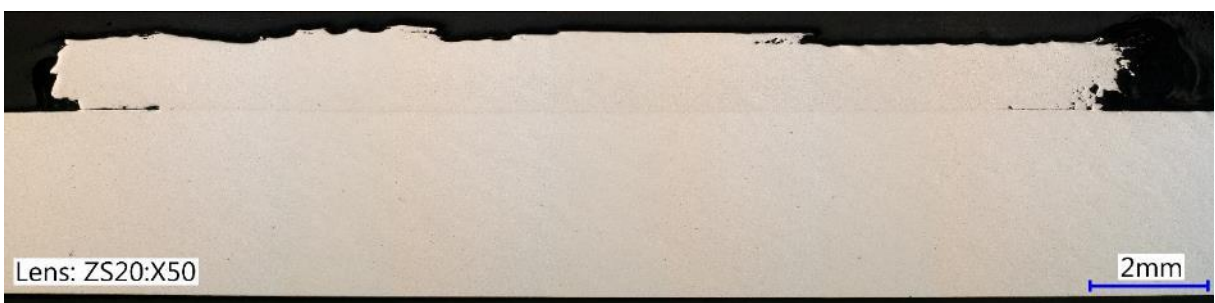
Specimen 02



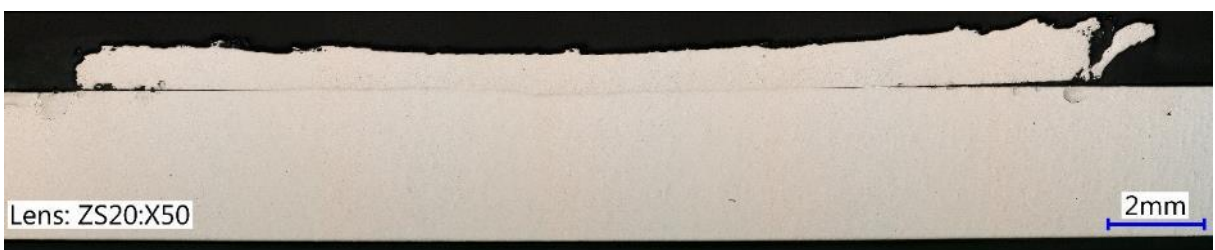
Specimen 03



Specimen 04



Specimen 05



Specimen 06



Specimen 07



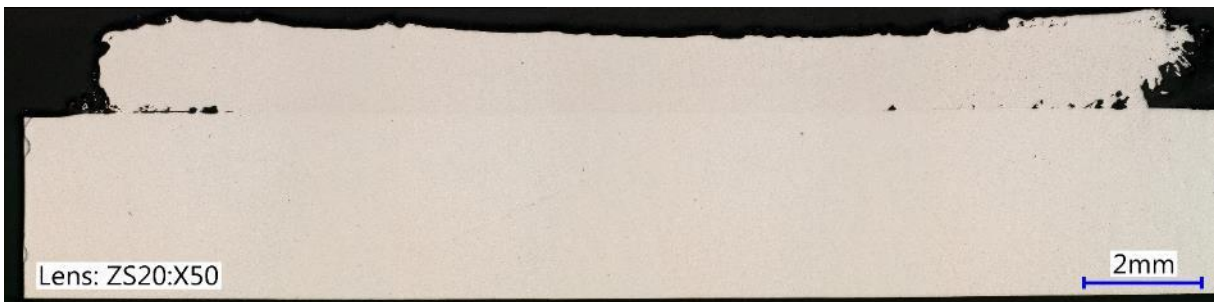
Specimen 08



Specimen 09



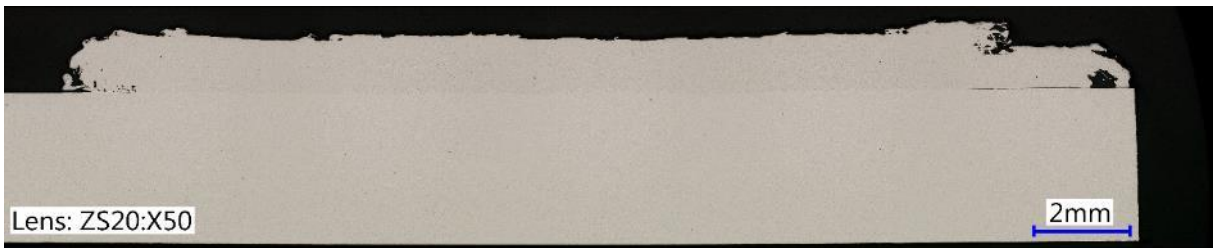
Specimen 10



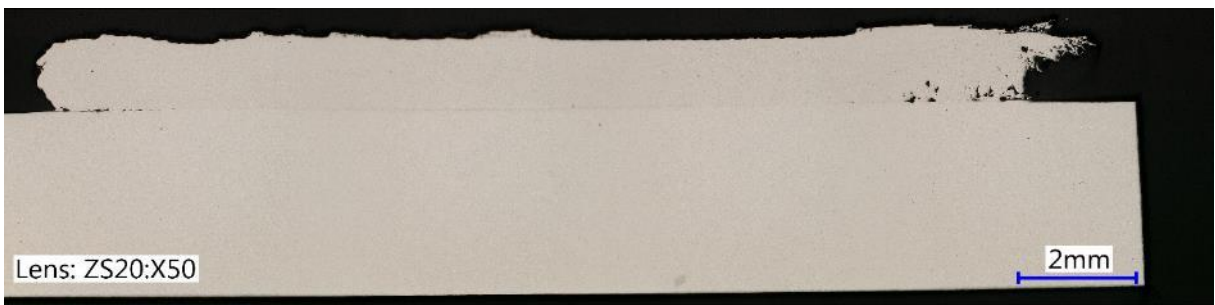
Specimen 11



Specimen 12



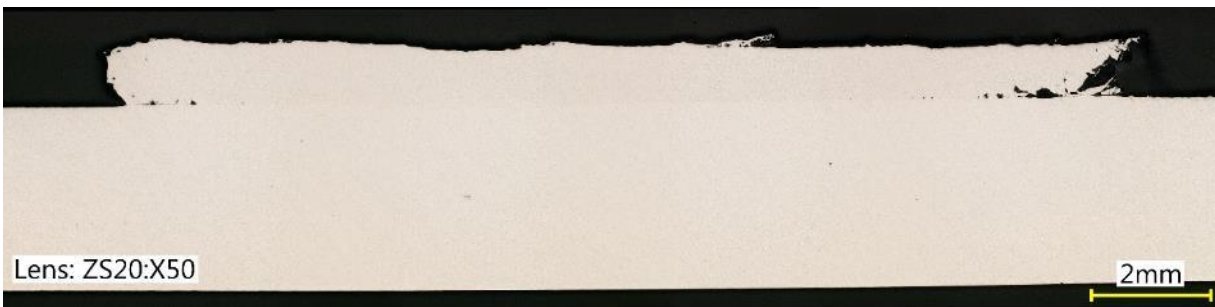
Specimen 13



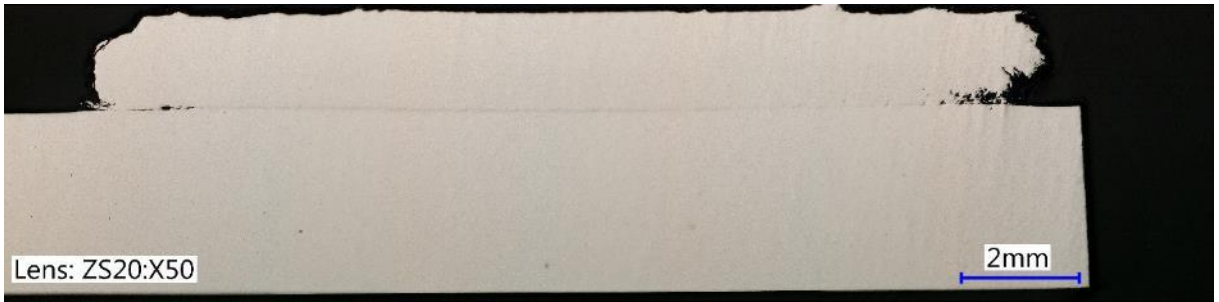
Specimen 14



Specimen 15



Specimen 16



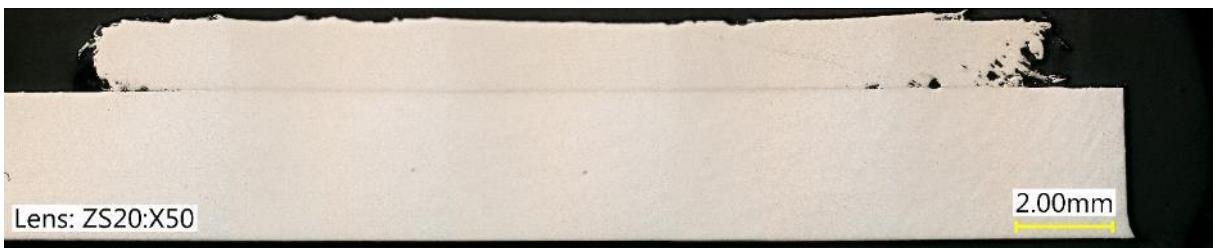
Specimen 17



Specimen 18



Specimen 19



Specimen 20



Specimen 21



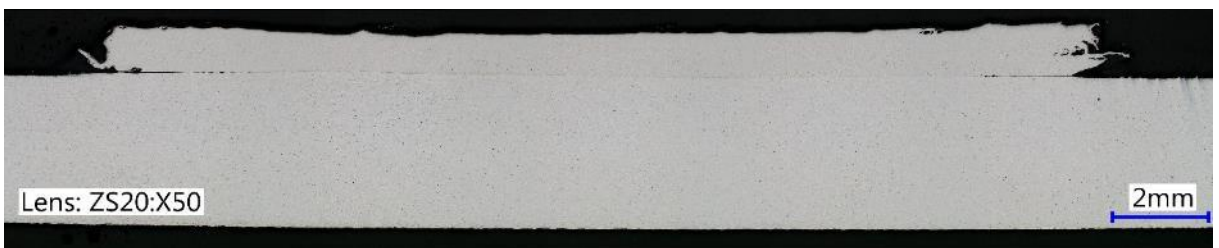
Specimen 22



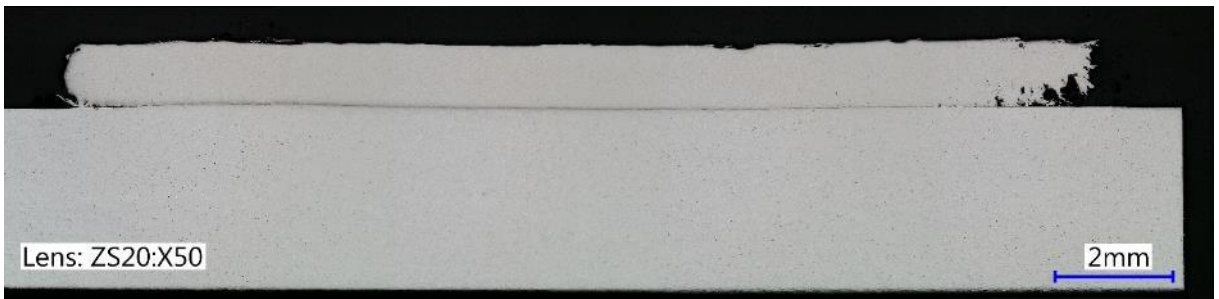
Specimen 23



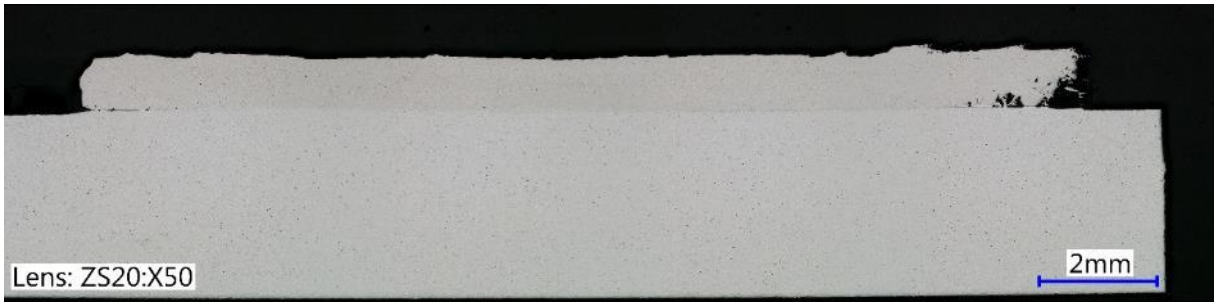
Specimen 24



Specimen 25



Specimen 26



Specimen 27



*AS always in the left edge.